LONDON'S GLOBAL UNIVERSITY

Development of tools and methodologies for proton dosimetry audit

Hannah Cook

A dissertation submitted in partial fulfilment of the requirements for the degree of

Doctor of Philosophy

at the

University College London

Supervisors: Dr. A. Lourenço

Prof. G. Royle

Dr. H. Palmans

Department of Medical Physics and Biomedical Engineering

University College London

2023

I, Hannah Louise Cook confirm that the work presented in this thesis is my own. Where information has been derived from other sources, I confirm that this has been indicated in the thesis

Dedication

For my loved ones

Abstract

High-energy proton beam therapy (PBT) is an advanced form of radiotherapy which is now being provided by the NHS in the UK. As for any radiotherapy, accurate dosimetry of proton beams is a prerequisite for a successful treatment. A crucial method of quality assurance assessment of the patient treatment is end-to-end dosimetry audits which evaluate the quality of practice of the full treatment.

This work contributes to PBT audits, through the development of tools and techniques that increase the accuracy of the determination of absorbed dose. Existing tissue-equivalent materials (TEM) have been shown to be unsuitable for PBT audits. This project developed a cost-function model for the formulations of imaging photon and therapeutic proton optimised TEM. In addition, new materials were successfully manufactured and characterised by experiments and Monte Carlo simulations. These novel materials were shown to be superior to current commercial TEMs. The best novel formulations were shown to mimic stopping power, mass attenuation, and mass density within 2%, along with further reducing the uncertainty in other key radiation properties.

This work has also led to the development of two bespoke phantoms that test PBT delivery challenges. The Range Length Phantom studies show film can provide repeatable range measurements within an average relative uncertainty of 0.5% for a series of heterogenous phantom setups within an audit setting. A pilot audit was

performed with the PRoton heaD and NeCk Evaluation phantom. The study showed 2% agreement between detectors within the tumour region to treatment planning system predictions. Film analysis showing a >95% pass rate for 4%/3 mm gamma analysis. Overall, the phantom was shown to be a useful tool to evaluate PBT deliveries and provides a realistic challenge for clinical centres as part of an end-to-end audit service.

Impact Statement

One in two people in the UK will be diagnosed with cancer in their lifetime and 50% of those people will receive radiotherapy as part of their treatment. For the best patient outcome, radiotherapy needs to provide a targeted treatment to the tumour. Proton beam therapy can deliver a high dose to kill the tumour and prevent damage to surrounding tissues compared to that of conventional radiotherapy techniques. Therefore, in recent years high-energy proton beam therapy has been provided by the NHS to treat complex adult and pediatric cancer patients.

Quality assurance (QA) measures are essential within radiotherapy to ensure safe and accurate delivery of the complex radiotherapy treatments. Currently, certain QA tools used in proton therapy are made from materials designed for other radiotherapy techniques. Therefore, use of these tools can result in radiotherapy QA testing being inaccurate or unsuitable for proton therapy treatments. Moreover, due to the challenges in measuring dose to patients directly, phantoms that simulate the patient geometry and composition are a crucial tool for quality assurance and assessing the risk of novel therapeutic and imaging modalities. The accuracy of the dose measurements depends on the realism of the phantoms used to describe the patient, in terms of elemental composition and internal anatomical shape of the human body.

In this work, a first of its kind Range Length Phantom (RaLPh) was developed to independently assess the range prediction in heterogeneous scenarios within a multi-centre dosimetry audit setting. A cost-function model for the formulation of new tissue-

equivalent plastic materials that simulate the composition of a patient was developed. Based on these findings, a range of novel bone and muscle-equivalent plastics were formulated, produced, and experimentally verified. This led to the development of an optimised anthropomorphic PRoton heaD and NeCk Evaluation phantom (PRuDeNCE) which houses active and passive detectors that can be used to independently verify, by measurement, the clinical proton therapy treatment pathway. A clinical national audit was developed to evaluate the quality of the practice of PBT, thus supporting the safe and effective adoption and improvement of this complex treatment modality in the UK as well as providing quality assurance support for the first national proton trial. This work has been published in academic journals, presented internationally to the medical physics community, and resulted in the completion of a national pilot proton audit.

The tools and methodologies developed during this work has provided clinical proton medical physics staff with confidence in delivering complex radiotherapy treatment. The QA tools developed provide patient pathway (imaging, planning and treatment) testing which could potentially identify issues which may cause patient harm, and so ensures safe implementation of radiotherapy techniques and the best practice for clinical trials within the field of proton therapy.

Acknowledgements

I would sincerely like to thank my supervisors, Ana Lourenço, Hugo Palmans, and Gary Royle, without whom this work would not have been possible. I am truly grateful for their guidance, support, and patience through this process. To Gary Royle for your encouragement throughout the academic process and supporting my endeavours to attend training and conferences internationally. To Hugo Palmans for being a patient teacher and incredible knowledge in the field of radiation dosimetry and proton therapy. Your thoughts and guidance of my experimental design and analysis throughout the years has enabled me to make the utmost of my project. Last but no means least, Ana Lourenço has been a guiding light through my PhD. I am extremely indebted to her for support, guidance, and enthusiasm over the past years. Thank you for always believing in me, even when I was disbelieving. You are an amazing role model and an inspirational '#protongirl'.

I owe a special thank you to my colleagues and close collaborators at The National Physical Laboratory (Mohammed Hussein, Russell Thomas, Catharine Clark, Warda Heetun, Kelley Ferreira and many more) and University College London (Andy Nisbet, Charles-Antoine Collins Fekete, Esther Bär, Caterina Veiga, and Michaël Simard). Thank you for the countless hours spent on discussing details of my projects and for being involved with my work. I must give thanks to all the other PhD students (Sam Flynn, Michael McManus, Daniela Botnariuc, Reem Ahmad, Yunen Cervantes and Chris Green) who I met along the way and the great friendships I have made. Thank you for all the good times in the office and the pub! I would also like to express

huge gratitude to all the wonderful collaborators from different research groups and backgrounds. Your can-do attitudes and support made this work possible. Thank you to the staff at the Rutherford Cancer Centres Proton Centres (John Pettingell, Jamil Lambert, Mark Osborne, Edward Ilsley, Yit-Fong Chan, and Jeevan Pandey), UCLH NHS Foundation Trust Proton centre (Callum Gilles and Vasilis Rompokos) and The Christie NHS Foundation Trust Proton Centre (Matt Lowe).

A big thank you to Nathan Niemann (BARTS NHS Trust) for kindly supporting the developing of the plastic materials for the project. I would like to also thank the excellent engineering services at the UCL Electronic and Electrical Engineering workshop (Thomas Hamer and John Langdon), NPL Design team (Peter Lovelock and Michael Parfitt) and Engineering Workshop (Keith Burgon and Paul Stevens) for the manufacture of the phantoms developed during this project.

Finally, I want to express the most heartfelt thanks to my family and partner for their unconditional love and support through this process. You have supported me through all the highs and lows of the PhD, and I will be forever grateful.

UCL Research Paper Declaration Form

referencing the doctoral candidate's own published work(s)

For a research manuscript that has already been published:

Publication 1

a) Title of manuscript: Development of a heterogeneous phantom to measure range in clinical proton therapy beams
b) DOI: 10.1016/j.ejmp.2021.11.006
c) Journal: Physica Medica
d) Publisher: Elsevier
e) Date of publication: January 2022
f) List of the manuscript authors in the order they appear on the publication: H. Cook, J. Lambert, R. Thomas, H. Palmans, M. Hussein, C.H. Clark, G. Royle, J. Pettingell, A. Lourenço.
g) Was the work peer reviewed? Yes
h) Have you retained the copyright? No
i) Was an earlier form of the manuscript uploaded to a preprint server? No

I acknowledge permission of the publisher named under 1d to include in this thesis portions of the publication named as included in 1c. ✓

Publication 2

a) Title of manuscript: Development of optimised tissue-equivalent for proton therapy
b) DOI: 10.1088/1361-6560/acb637
c) Journal: Physics in Medicine & Biology
d) Publisher: IOP Publishing
e) Date of publication: January 2023
f) List of the manuscript authors in the order they appear on the publication: H. Cook, M. Simard, N. Niemann, C. Gilles, M. Osborne, M. Hussein, V. Rompokos, H. Bouchard, G. Royle, J. Pettingell, H. Palmans, A. Lourenço.
g) Was the work peer reviewed? Yes
h) Have you retained the copyright? No
i) Was an earlier form of the manuscript uploaded to a preprint server? No

I acknowledge permission of the publisher named under 1d to include in this thesis portions of the publication named as included in 1c. ✓

RESEARCH PAPER DECLARATION

Publication 3

For a research manuscript prepared for publication but that has not yet been published:

a) Title: Development of the PRoton heaD and NeCk Evaluation (PRuDeNCE) phantom for proton therapy audit
b) Has the manuscript been uploaded to a preprint server? No
c) Where is the work intended to be published? TBC
d) List the manuscript's authors in the intended authorship order
e) Stage of publication: First draft

For multi-authored work, please give a statement of contribution covering all authors:

Publication 1: Authors provided contributions to the conception or design of the work, experimental data acquisition, analysis, and interpretation of data for the work. Authors provided comments to the drafting of the manuscript for publication.

Publication 2: Authors provided contributions to the conception or design of the work, experimental data acquisition, analysis, and interpretation of data for the work. Authors provided comments to the drafting of the manuscript for publication.

Publication 3: Authors provided contributions to the conception or design of the work, experimental data acquisition, analysis, and interpretation of data for the work. Authors provided comments to the drafting of the manuscript for publication.

In which chapter(s) of your thesis can this material be found?

Chapter 2, 3, and 4.

5. e-Signatures confirming that the information above is accurate (this form should be co-signed by the supervisor/ senior author unless this is not appropriate, e.g., if the paper was a single-author work)

Candidate: Signed

Supervisor/ Senior Author: Signed

Date 08/03/2023

Table of Contents

TABLE OF CONTENTS

TABLE OF CONTENTS

Table of Figures

TABLE OF FIGURES

Table of Tables

TABLE OF TABLES

Abbreviations

CSDA	Continuously slowing down approximation
CT	Computed tomography
CTV	Clinical target volume
DECT	Dual-energy computed tomography
GTV	Gross target volume
HU	Hounsfield units
ICRU	International Commission of Radiation Units and Measurements
IROC	Imaging and Radiation Oncology Core
LET	Linear energy transfer
MC	Monte Carlo
MRI	Magnetic resonance Imaging
MU	Monitor unit
NHS	National Health Service
NPL	National Physical Laboratory
NTCP	Normal tissue complication probability

ABBREVIATIONS

OAR	Organs at risk
OD	Optical density
OSLD	Optically stimulated luminescence dosimeter
PDD	Percentage depth dose
PDI	Percentage depth ionisation
PET	Positron emission tomography
PTCOG	Particle therapy co-operative group
PTV	Planning target volume
PPRIG	Proton physics research implementation group
RBE	Relative biological effectiveness
RE	Relative effectiveness
RSP	Relative stopping power
SECT	Single-energy computed tomography
SOBP	Spread out Bragg peak
TCO	Tissue control probability
TLD	Thermoluminescent dosimeter
TPS	Treatment planning system
WET	Water-equivalent thickness

Science Communication

The work presented in this thesis has resulted in the following outputs.

Peer-reviewed journal papers:

Cook H., Lambert J., Thomas R., Palmans H., Hussein M., Clark C.H., Royle G., Pettingell J., & Lourenço A. Development of a heterogeneous phantom to measure range in clinical proton therapy beams. Physica Medica **93**, 59-68, (2022)

Cook H., Simard M., Niemann N., Gillies C., Osborne M., Hussein M., Rompokos V., Bouchard H., Royle G., Pettingell J., Palmans H., Royle G., Pettingell J., & Lourenço A. et al. Development of optimised tissue-equivalent materials for proton therapy. Physics in Medicine & Biology **68,** 075009, (2023)

Cook H., Niemann N., Gillies C., Rompokos V., Lowe M., Hussein M., Clark C.H., Thomas R., Nisbet A., Royle G., Palmans H., & Lourenço A., (2023). Development of the PRoton heaD and NeCk Evaluation (PRuDeNCE) phantom for proton therapy audit. TBC (in preparation)

NPL Audit reports:

Cook H., Hussein M., & Lourenço A. Report on Proton Head and Neck End-to-End Dosimetry Pilot Audit at University College London Hospital Proton Beam Therapy Centre. NPL audit report, (2023) (drafted)

Cook H., Hussein M., & Lourenço A. Report on Proton Head and Neck End-to-End Dosimetry Pilot Audit at The Christie Proton Beam Therapy Centre. NPL audit report, (2023) (drafted)

Oral presentations:

Cook H., Lambert J., Thomas R., Palmans H., Hussein M., Clark C.H., Royle G., Pettingell J., & Lourenço A. Development of RALPH (proton RAnge Length PHantom) for proton range uncertainty audit. 58th Annual conference of the particle therapy co-operative group 2019; *Manchester, U.K.*

Cook, H., Royle, G., Palmans, H., & Lourenço, A. Simulations for the improvement of bone-equivalent materials for proton beam dosimetry. International Conference on Monte Carlo Techniques for Medical Applications 2019. *Montreal, C.A.*

Hussein, M., Barry, M., **Cook, H.,** Lourenço, A., Patallo, I. S., Shipley, D., & Clark, C. H. RayStation at the National Physical Laboratory – current and future opportunities for research and development, Raystation European User Meeting 2020; *Online*

Cook, H., Simard M., Niemann N., Gillies C., Palmans H., Hussein M., Bouchard H., Royle G., & Lourenço A. Optimising tissue-equivalent materials for proton therapy. European Society for Therapeutic Radiology and Oncology Conference 2022; *Copenhagen, D.K.*

Botnariuc D., Ghica C., **Cook H**., Bento M., Nisbet A., Royle G., Hussein M., Lourenço A., & Veiga C. A Monte Carlo framework to evaluate the radiological properties of 3D-printable materials for proton therapy phantom development. International Conference on Monte Carlo Techniques for Medical Applications 2022; *Antwerp,*

B.E.

Poster presentations:

Cook H., Lambert J., Thomas R., Palmans H., Hussein M., Clark C.H., Royle G., Pettingell J., & Lourenço A. Measurement of range uncertainties using radiographic film and a bespoke phantom. Proton Physics Research Implementation Group Workshop 2019; *Teddington, U.K.*

Cook H., Royle, G., Palmans, H., & Lourenço, A. Development of a bone-equivalent material for the dosimetry of proton therapy beams. 58th Annual Conference of the Particle Therapy Co-Operative Group 2019; *Manchester, U.K.*

Cook H., Niemann N., Gillies C., Rompokos V., Lowe M., Hussein M, Clark C.H., Thomas R., Nisbet A., Royle G., Palmans H., & Lourenço, A. A new audit tool for proton therapy: PRoton heaD and NeCk Evaluation (PRuDeNCE) phantom, 61st Annual Conference of the Particle Therapy Co-Operative Group 2023; *Madrid E.S.*

Prize:

The Postgraduate Institute of Measurement Science Conference 2021, #GrAbPGI Competition: 2nd place for graphical abstract – Online

1. Introduction

1.1. Context of project

1.1.1. Radiotherapy with protons

In recent years, the UK government has invested £250M in two National Health Service (NHS) state-of-the-art proton therapy clinics [1] to provide high energy scanning proton beam treatments for cancer patients. Proton therapy has been adopted within the UK to treat a series of static cancer sites such as brain, spinal cord, eye, and head and neck cancers as well as treating paediatric patients [2]. The creation of these facilities is in response to the potential that proton beam therapy has over other well-established modalities.

Currently, about 50% of cancer patients receive radiotherapy as part of their treatment [3]. Research has shown that late effects such as second cancers, cardiovascular disease, and fertility complication are high in long-term survivors of cancer having undergone radiotherapy [4–6]. Therefore, it is imperative that healthy tissue is spared so that the probability of these late effects are significantly reduced for patients [7–9]. Due to proton interactions with matter, the beam can deliver a high dose to kill the tumour and prevent damage to surrounding tissue due to its finite range compared to that of conventional radiotherapy that uses photons [10].

Figure 1.1 shows the comparison of the photon and proton depth dose distribution as it travels through a patient to the tumour [11].

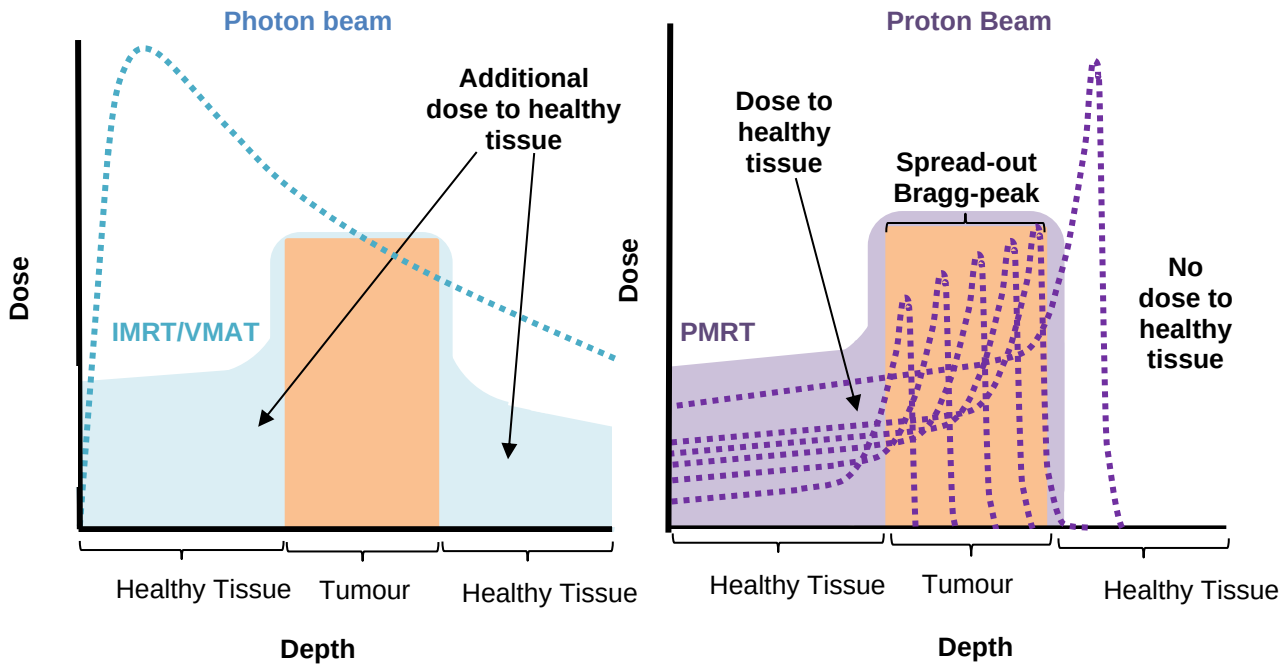

Figure 1.1 *Photon vs Proton dose profile [11]. Shaded regions illustrate the total dose distribution with depth.*

Photons deposit their energy indirectly, they transfer energy to charged particles (such as electrons and positrons) which then deposit their energy via charged particle interactions [12]. This transfer of energy can occur via three main types of interaction: photoelectric effect, Compton scattering and pair production. This results in a depth dose which is a combination of the inverse square law, secondary charged particle build up, and the attenuation of photons via absorption and scattering interactions [13]. This creates the characteristic shape of a continuing reduction of dose with depth after the build-up region and the dose maximum. Thus, the main disadvantage of photon treatments are the higher dose proximal to the target region as well as the dose deposited behind the tumour.

Unlike photons, protons have regular direct interactions with the medium due to Coulomb interactions and scattering [12]. These interactions are described in further detail in Chapter 3. The charged particles engage in a quasi-continuous energy loss

mechanism of which the mean value for a large number of particles is called the ‘continuous slowing down approximation’ (CSDA). The slower the particle the more energy is deposited in the medium per unit of path length, thus this produces the Bragg peak in a proton depth-dose distribution and finite range of the particle (Figure 1.1). Given that the Bragg peak is quite narrow, proton treatments are optimised by generating a spread-out Bragg peak (a series of superimposed Bragg peaks over a range of energies) to provide a uniform energy deposition in the tumour volume and little to no energy deposition after the tumour. However, a drawback of using modulated proton beams is the higher skin dose for the patient in comparison to photon beams as well as possible larger field edge depending on proton system and setup parameters [14]. The lateral field edge of a proton beam is dependent on several factors such as air gap, proton range, compensator thickness, proton fluence pattern, and depth within the patient [15]. Consequently. the lateral field edge can be worse for proton treatment especially when a range shifter is used for shallower targets with scanning proton beams systems [16].

1.1.2. Radiotherapy Dosimetry

As for any radiotherapy, accurate dosimetry of proton beams is a prerequisite for a successful treatment. Radiation dosimetry refers to the area of metrology that aims to measure and determine the absorbed dose of direct or indirectly ionising radiation within and around the human body. Absorbed dose is the physical quantity which is defined as the measure of the energy imparted per unit mass [17]. It is typically expressed in the derived SI unit of gray (Gy). For proton therapy, dose can be calculated as follows:

$$\mathrm{D} = \Phi \frac{S}{\rho} \tag{1.1}$$

where dose (D) is equal to fluence times the stopping power. Fluence (Φ) is defined as the quotient of dN by da, where dN is the number of particles incident on a sphere of cross-sectional area da. ρ is the mass density of the medium. Mass stopping power ($\frac{S}{\rho}$) is the rate at which a single proton loses kinetic energy per unit of path length (expressed as mass thickness) of the stopping medium.

Due to the human body being composed of approximately 80% water in soft tissue and 30% water in bones, dose in radiotherapy is specified in water. Radiation dosimetry measurements are typically performed in water phantoms at a specific reference point and conditions for a given radiation beam quality [12], where the beam quality describes the energy spectrum of the radiation beam. Calorimetry provides the most direct method to determine absorbed dose-to-water, either via the use of water calorimeters or graphite calorimeters with a graphite-to-water conversion [18,19]. The energy deposited in the medium is measured by the direct temperature rise within the medium. Absorbed dose is determined by equation 1.2.

$$\mathrm{D}_{\mathrm{med}} = c_{\mathrm{med}} \cdot \Delta \mathrm{T}_{\mathrm{med}} \tag{1.2}$$

where c_{med} is the specific heat capacity of the medium, $\Delta \mathrm{T}_{\mathrm{med}}$ is the temperature change of the medium. Correction factors should also be considered for heat transport, field nonuniformity and changed scatter and attenuation due to the presence of non-medium-equivalent materials. Due to the cumbersome nature of calorimeters, they are not used within the radiotherapy clinics, but kept within National Measurement laboratories to provide calibration factors for secondary standard ionisation chambers

within a reference radiation beam (^{60}Co beam). Reference dosimetry practice therefore allows for traceability to primary standards measurements for air kerma and absorbed dose to water to the ionisation chamber used in the clinic, which ensures harmonisation of absorbed dose given to patients within the clinic [20].

Ionisation chambers are the key reference dosimetry detector used within clinics to provide absorbed dose measurements. For a proton beam, the dose to water (D_{w,Q_0}) for a reference beam of quality (Q_0) can be determined as follows [12]:

$$D_{w,Q_0} = M_{Q_0} N_{D,w,Q_0} \tag{1.3}$$

where M_{Q_0} is the reading of the dosimeter under reference conditions used in the standard laboratory and N_{D,w,Q_0} is the calibration factor in terms of absorbed dose to water in a ^{60}Co beam. In clinical scenarios, further correction factors are required for the differences in the reference conditions to that of the standard laboratory, such as detector and radiation field influencing quantities. Ionisation chambers can be used to measure at precise depths, distance, and field sizes specified in dosimetry protocol or codes of practice, such as the Atomic Energy Agency (IAEA) TRS-398 [21]. These measurements provide confidence in the dosimetry of radiotherapy measurements from proton machine commissioning to the validation of radiation treatments offered to patients.

1.1.2.1. Monte Carlo simulations

Monte Carlo has become a vital tool for radiation dosimetry research as the numerical method provides a technique to solve complex transport equations [22]. A range of Monte Carlo models have been adapted for radiotherapy applications, such as Electron TRANsport (ETRAN) [23], FLUktuierende KAksade (FLUKA) [24],

Electron Gamma Shower (EGS) [25], GEometry And Tracking (Geant4) [26], and PENetration and Energy Loss of Positrons and Electrons (PENELOPE) [27]. Monte Carlo provides an environment to simulate radiation physics within complex 3D geometries such as detailed clinical accelerators, ionisation detector, and patient geometry to determine dosimetric quantities such as absorbed dose and stopping-power ratios [28]. Monte Carlo is particularly useful for the estimation of quantities that are difficult to determine experimentally such as perturbation factors due to ionisation chambers. However, Monte Carlo calculations should not be considered error free and the limitations of the model should be understood before using the numerical tool.

Monte Carlo simulations were performed throughout this work and further details on the simulations can be found in Chapters 2, 3 and 4. For this work, FLUKA packages were used to create realistic simulations of a proton beam transport for a specific energy travelling through a medium or setup to validate experimental measurements and to provide further information on key dosimetric quantities of interest.

1.1.3. Radiotherapy in the clinic

For radiotherapy, the treatment should provide the best possible care to the patient [29]. The patient should receive an accurate treatment which is reasonably achievable after technical and biological factors are considered [30]. A figure of 5% uncertainty for dose to the tumour (in some cases, within 2% uncertainty) with 95% confidence is stated by the International Commission on Radiation Units and Measurements [31]. This is due steepness of the dose response curves (seen in Figure 1.2) making the therapeutic window for a successful treatment very narrow [32]

(seen in Figure 1.2). The goal of radiotherapy is to achieve maximised tumour control while minimising tissue complications [33].

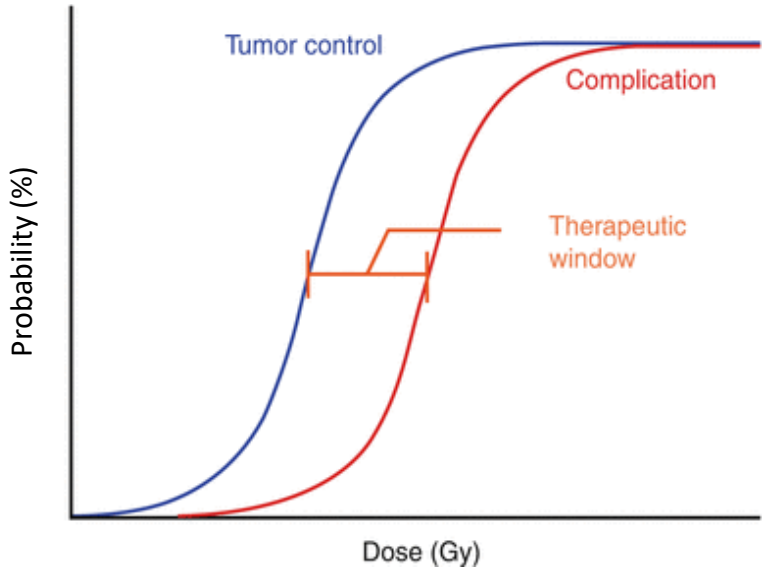

Figure 1.2 *Clinical evidence of the dose effect on TCP (blue line) and NTCP (red line) [28]*

For proton therapy, this goal of 5% uncertainty (95% confidence interval) is not currently achievable due to a range of contributing uncertainty factors in the dosimetry chain including reference dosimetry, patient positioning, patient imaging, treatment planning and beam uncertainties [34]. Currently, reference dosimetry performed with ionisation chambers alone has a 2.0-2.3% uncertainty (68% confidence interval) for dose measurements in water [21]. Consequently, there is a variety of clinical studies and research at every stage of the dosimetric chain to try and reduce these uncertainties so that the potential of proton therapy can be harnessed for radiotherapy [35].

1.1.3.1. Radiotherapy audits and phantoms

One method within the field of radiotherapy dosimetry to ensure accuracy, precision, and consistency of clinical centres is dosimetry audits [36]. Audits range

from postal to onsite visits which can perform reference measurements to patient pathway testing. Audits have been shown to uphold and improve standards as well as highlight any potential issues with a treatment modality [36]. Quality assurance and compliance of clinical centres is critical for improving general patient outcome and enabling successful clinical trials [37]. A vital tool for radiotherapy dosimetry audits is the use of radiotherapy phantoms.

A phantom is 'a body of material resembling a body or bodily part in mass, composition, and dimensions and used to measure dose distributions' [38]. The use of phantoms has existed in the field of Medical Physics almost as long as ionising radiation has been used to treat patients [39]. The use of real humans for repeated testing of radiation procedures is not practical or ethical hence the need for the development of phantoms. Although phantom development had been around for over 120 years, a recent review of phantom research has shown the area is still thriving with the number of publications rising annually (Figure 1.3). [40].

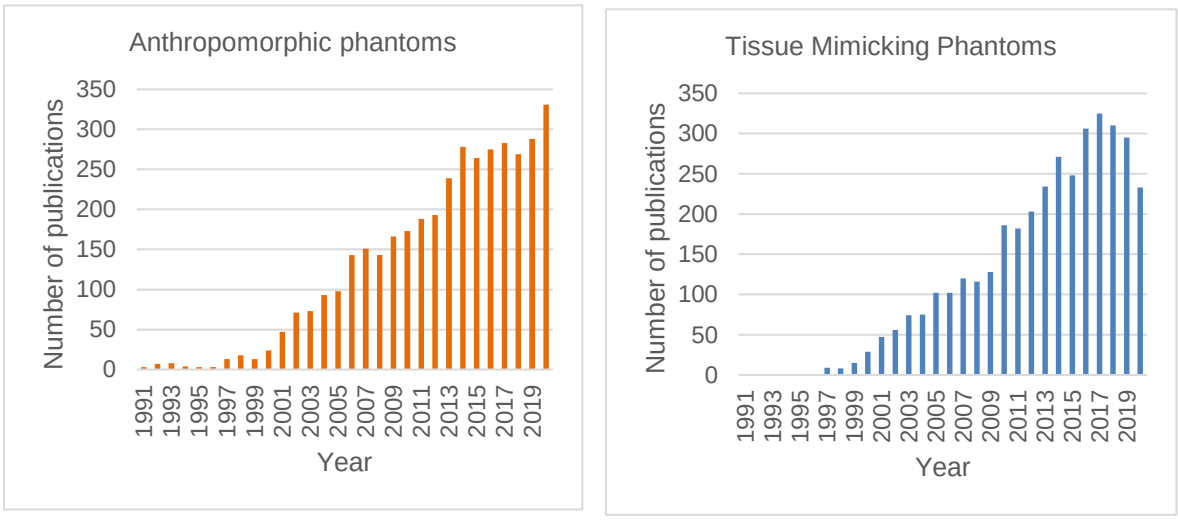

Figure 1.3 *Research articles published per year between 1991 and 2020 in the Web of Science database with search terms a) Anthropomorphic phantoms and b) Tissue Mimicking Phantoms.*

Today, phantoms have been implemented into a range of medical physics areas (Figure 1.4); from testing of therapeutic therapies (X-rays, brachytherapy, and ion therapy treatments) and clinical imaging procedures (CT, SPECT, PET, MRI, Ultrasound) to phantoms for clinical education and training of therapeutic surgery and computational applications [39,40]. The development of phantoms is dependent on its purpose, which can affect the physical size, shape, material composition, and detectors used internally or externally in the phantom [41–46].

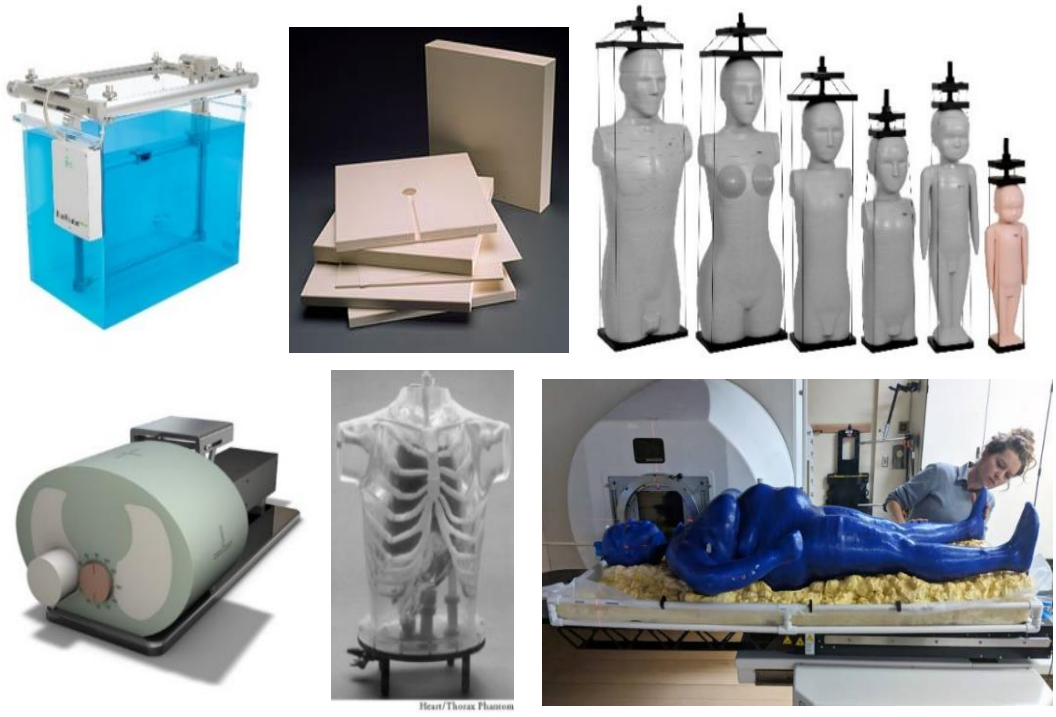

Figure 1.4 *Examples of difference types of phantoms (Top row from left to right: water phantom, water-equivalent material slabs, CIRS ATOM anthropomorphic phantoms. Bottom row from left to right: Moving target lung phantom, nuclear medicine phantom, 3D printed body) [41-46]*

The challenges of any dosimetric phantom design and manufacture can be broken down into three key components: materials selection, geometry, and detectors. For this work, the focus was on the research into radiotherapy phantoms.

1.1.3.1.1. Materials Selection

For many dosimetry scenarios, water phantoms are used due to water being easily obtainable as well as water molecules being dominant in the human composition. However, water doesn't mimic the variety of human tissue compositions, for example, lung, dense bone, and adipose tissue, and so there has been a need to develop a range of tissue-equivalent materials. The composition of tissue-equivalent materials is based on published data on human tissue compositions [47,48] and characteristics of the type of radiation.

In some situations, human skeletons have been used in radiotherapy phantoms [49]. However, composition uncertainty of the specific bone and bone marrow degradation over time can cause dosimetric uncertainty. Consequently, human bone isn't typically implemented in modern phantoms. Other organic animal tissues have been used as or within phantoms, but natural decay of tissue leads to limited use [50,51]. Therefore, research has gone into formulating inorganic tissue-equivalent materials with which radiation interacts as closely as possible to irradiated human tissue over the required range of energies.

One of the first tissue substitute materials used for radiotherapy was wax, however, its limitations as a tissue substitute material were highlighted by the radiotherapy community. Consequently, from the 1940s there was a push to develop new tissue-equivalent materials for radiotherapy [52]. Firstly, research began by trying to develop materials that matched the atomic composition of human tissues. However, this trial and error method of developing tissue-equivalent materials became very complex for tissue with a large number of elemental components. [52]. Hence, tissue-equivalent materials are often formulated so that their radiation interaction properties

are equivalent rather than their atomic composition. The different mathematical methods devised for tissue-equivalent material formulation will be explained in more detail in Chapter 3. Consequently, a range of tissue-equivalent materials have been developed in a variety of physical forms, solid [49,52–54], liquid [55], and gel forms [56] .

However, developing these materials can be an expensive and technical process so other methods are now being considered, such as urethane mixtures [57] and 3D printable materials [58]. The 3D printing process can provide cheap customised fabrications for radiotherapy phantoms [59–62]. However, there are still challenges regarding making a range of 3D printable materials that are tissue-equivalent within acceptable radiotherapy dosimetry uncertainties [63,64].

1.1.3.1.2. Geometry

Geometry of the phantom is a crucial design parameter during the development of the radiotherapy phantoms. The size and shape are dependent on the use of the phantom but will often mimic anatomic geometries. The geometry of the phantom must satisfy both absorption and scattering properties of the radiation type, otherwise this may affect the detector results within the phantom [52]. Epoxy resin-based tissue-equivalent materials can be moulded into anthropomorphic shapes, however, this can be a costly process. [49,54,65].

3D printing has potential for the development of an anthropomorphic phantom due to the ability to easily print 3D shapes without the need of moulds or advanced manufacture processes. However, 3D printing can be prone to printing filament variability [62], phantom printing size restrictions, and defects such as small unintended air voids [66] or warping. A study by the Imaging and Radiation Oncology

Core (IROC) team (IROC Houston QA Centre Houston, TX, U.S.A) showed significant variability in relative stopping power (RSP) for 3D printed materials depending on the sample print direction relative to beam orientation [63,67]. Therefore, the 3D printing manufacture process has limitations that need to be considered in the phantom design.

1.1.3.1.3. Detectors

The development of a dosimetry phantom with suitable materials and geometry is worthless unless the correct detectors are selected and applied within or around the phantom. Typically, absolute dose in target volume as well as a 3D dose profile is required within the phantom so that comprehensive dose verification can be achieved within the target as well as accessing the dose distribution in other regions such as organs at risk (OAR). There are a range of possible detectors that can be implemented within the phantom, each with their key advantages and disadvantages [39]. The detector should not affect the dose measurements, accordingly small and tissue-equivalent detectors are most appropriate for dosimetric phantom applications.

Three types of detectors that are typically used in phantom dose verification due to their near tissue-equivalence are thermoluminescent dosimeter (TLD), alanine and film. TLD and more recently optically simulated thermoluminescent dosimeter (OSLD) detectors are implemented in many of the phantoms developed by IROC for radiotherapy audit and provide dosimetric precision of 3% uncertainty (68% confidence level) for dose measurements [68–70]. Alanine pellets were used by Carlino *et al.* (2018) [37] for a dosimetric end-to-end audit and provide dosimetry precision of 3% uncertainty (68% confidence level) for dose measurements [71]. Film dosimeters enable high spatial 2D resolution and are used in many phantoms to provide dose distribution measurements for gamma analysis of agreement with

treatment planning system (TPS) dose calculations [37,68,72,73]. However, alanine [37], TLD [74], OSLD [75],and film [76,77] are susceptible to signal quenching effects, causing an under response of the dosimeter within the high linear energy transfer (LET) region of the proton beam and so corrections should be applied for absolute dose dosimetry measurements. Consequently, although not tissue-equivalent, ionisation chambers are also used within phantoms as they are considered the ‘gold standard’ for absolute dose measurement within dosimetry.

1.2.3.2. Radiotherapy phantoms for proton therapy

Currently, many proton centres use phantoms that have been developed for other radiotherapy modalities. Proton phantoms are typically made of photon tissue-equivalent materials which have not been optimised to be proton equivalent. For example, materials have been tailored to match properties such as electron density. Matching of a specific electron density can be achieved by a range of materials with different atomic number elements. However, for proton therapy key interaction properties such as stopping power are sensitive to the elemental composition and atomic number of the elements within the medium. Therefore, materials can lead to two main issues; i) large uncertainty for proton dosimetry measurements, such as dose and/or range measurements; ii) they require treatment planning material override of the phantom materials in the TPS which results in a phantom that does not examine the full patient workflow.

Work by Grant *et al.* (2014) [78] has highlighted many previously used tissue-equivalent materials, such as PMMA, bone meal and pressed cork, are not suitable for proton therapy. Out of the 18 tested materials, only 50% of the materials fell within the IROC acceptance criteria of less than 5% uncertainty between TPS and assigned

RSP values. This work highlights that selection of suitable phantom materials is required for proton phantom manufacture to ensure accurate proton dosimetry. Work by Lewis *et al.* (2018) [73] presented similar findings for their work into the development of a paediatric spine phantom for proton therapy. Testing of commercial bone-equivalent materials used for X-rays, such as Gammex Inner bone (Gammex, Sun Nuclear, Norfolk, VA U.S.A), Gammex Cortical bone, Polyether ether ketone (PEEK), Polyethylene terephthalate (PETP), are shown to be unsuitable and could lead to relative errors of up to 35% in range calculations by the TPS.

There exists a small number of phantoms developed specifically for proton radiotherapy measurements, for which further information is given in Table 1.1. For many of these phantoms, the term proton-equivalent materials either means the stopping power of the material is within an acceptable uncertainty (i.e. 1.5% for Computerized Imaging Reference System Inc. (CIRS, Sun Nuclear, Norfolk, VA U.S.A) head and neck phantom [65]) or materials fall within 5% uncertainty on a clinical Hounsfield Unit (HU) - RSP conversion curve. [68,72]. However, for a phantom to be truly acceptable for proton therapy the tissue-equivalent materials should have ‘absorption **and** scattering properties of which, for a given irradiation, simulate as nearly as possible those of a given biological material such as soft tissue, muscle, bone, or fat’ within an acceptable uncertainty [38]. For proton end-to-end audit phantoms both photon and protons absorption and scattering quantities must be considered due to the phantom (or patient) being imaged with photons via computed tomography (CT) and then treated with protons. For photons, the attenuation coefficient is crucial, whilst for protons, the stopping power is considered the most important dosimetric property. Moreover, to mimic the total dose distribution the

nuclear interactions and scattering should also be considered for protons. Consequently, the key limitation with radiotherapy phantoms, in particular proton therapy phantoms, is the restrictive number of suitable materials for proton therapy and the limited dosimetric characterisation of these materials [40].

Chapter 3 will discuss the work into the development of photon and proton optimised tissue-equivalent materials. ICRU report 44 states that for radiotherapy dosimetry measurements in water and tissue-equivalent materials should not introduce uncertainties in absorbed dose measurement in the excess of 1% [38]. Although this criterion has been shown to be achievable for reference dosimetry measurements using water-equivalent materials in photon beams [79], for end-to-end dosimetry audits using a combination of water and tissue-equivalent phantoms, phantom materials with larger uncertainty (within 5%) have been shown to be clinical acceptable [68,73].

For this work, I aimed to develop proton optimised tissue-equivalent materials which performed better than current commercial materials and so the following proton tissue-equivalence criteria was set for the plastic materials: i) within 2% uncertainty for mass density, mass attenuation, and RSP, ii) within 5% for scattering and nuclear interactions. These targets were set depending on the physical and radiation properties ability to influence the material characterisation during the CT imaging process and proton dosimetry measurements, in addition to the challenge of matching multiple properties and using plastic materials to manufacture tissue-equivalent materials.

Also, within proton therapy audits there is a need for phantom designs that better test the complex nature of proton therapy treatments, such as the effects of

heterogeneities, patient daily variations, and movement on proton treatments. Chapter 2 and 4 will discuss two end-to-end audit phantoms developed during this project to test some of the key proton therapy clinical irradiation challenges. The main criteria for the development of acceptable proton phantom was set as the following: i) the phantom can be used as an end-to-end audit tool without the need for material overrides in the TPS [68] ii) the phantom shape and design should fulfil both absorption and scattering properties and therefore ensure repeatable and accurate detector measurement within the phantom [52].

Table 1.1 *Phantoms for proton therapy (anthropomorphic)*

Manufacture and Model	Body region	Materials used in phantom	Detectors used in phantom	Reference
CIRS Proton therapy dosimetry head phantom (Model: 731-HN)	Head	CIRS Tissue-equivalent materials (Soft tissue, Brain, and bone materials). Weight gain feature (fat layer). 3D printable tumour region or a neutral brain-equivalent material	Film in the sagittal direction (3 positions)	[65,80]
		CIRS Tissue-equivalent materials (Soft tissue, Brain, and bone materials).	Film in the sagittal direction (3 positions). Customised to include alanine pellets and ionisation chambers in brain region (tumour target)	[37,65,81]
		CIRS Tissue-equivalent materials (Soft tissue, Brain, and bone materials). Titanium insert in spinal region.	Film in the coronal direction (5 positions).	[65,82]
IROC Head Phantom	Head	RANDO® water-equivalent plastic and embedded human skull. (New phantoms use highly detailed polymer mouldings)	Film in the coronal and sagittal planes. Two TLD capsules in tumour target	[68,72]
MedAustron Homogenous phantom	Head	Polystyrene	Film in coronal direction (perpendicular to beam direction). Ionisation chamber and alanine in target volume	[37,83]
IROC Liver Phantom	Liver	Water filled phantom and Solid blue water (Standard Imaging, Madison, WI)	Film in the coronal and sagittal planes. Two TLD capsules in each target	[68]
Japan Clinical Oncology Group (JCOG) Liver Phantom	Liver	Acryl plate water filled phantom and Rib material (BE-H (Kyoto Kagaku Co. Ltd., Kyoto, Japan))	Ionisation chamber can be moved throughout the phantom	[84]

Table 1.1 continued.

IROC Lung Phantom	Lung	Solid Water® (Gammex, Middleton, WI), high density rib structure and compressed Cork with Balsa wood insert	Film in coronal, sagittal and axial planes and two TLD capsules in the target	[68]
Advanced Radiation DOSimetry system (ARDOS) Lung Phantom	Lung	High density balsa wood, Photon/Electron Solid water, SB3 Cortical bone	TLD, film and ionisation chamber in different lung motion scenarios	[85,86]
IROC Prostate	Prostate	Water filled phantom and polystyrene dosimetry insert	Film in the coronal and sagittal planes. Two TLD capsules in the prostate target	[68]
IROC Paediatric Spine	Spine	Solid water (Gammex, Inc., Middleton, Wisconsin), Blue water (Standard Imaging, Middleton, Wisconsin) and Techtron HPV Bearing Grade	Film in the coronal and sagittal planes. Two TLD capsules in the vertebral structures.	[73]
CIRS Thorax phantom	Thorax/ Spine	CIRS Tissue-equivalent material and CFR-PEEK or titanium for spinal implants	Film in coronal plan	[87]

1.2. Aim of work

To contribute to the improvement of the quality and consistency of proton therapy treatments through the advancement of dosimetry audit for proton therapy by the development of proton optimised tissue-equivalent materials and heterogeneous and anthropomorphic phantoms.

The aim of this work can be broken down into three objectives:

i) Investigation of proton optimised tissue-equivalent materials

Studies have shown the need for proton optimised tissue-equivalent materials [78]. The objectives of this project are:

- Adaptation of a semi-analytical tool developed by Palmans *et al.* (2002) [88], Al-Sulaiti *et al.* (2012) [89] and Lourenço *et al.* (2017) [90], which was previously used to develop water-equivalent materials optimised for nuclear interactions, for investigation of tissue-equivalent materials against human tissues for proton beams.

- Development of a mathematical model (cost-function approach) for the formulation of tissue-equivalent materials optimised for proton beam therapy, considering a range of radiation interactions for both photon and proton interactions.

- To study available tissue substitutes and develop new tissue-equivalent materials that are relevant for proton beams. Perform a study of tissue-

equivalent materials against real tissue to assess the tissue-equivalence of the materials.

- Manufacture of new epoxy resin-based tissue-equivalent materials for proton therapy, as well as experimental testing of newly developed materials to characterise them in photon and proton beams to ensure they pass the required proton phantom material criteria (defined in section 1.2.3.2.).

Research into new audit phantoms developed specifically for proton therapy, considering proton challenges and/or including proton optimised tissue-equivalent materials. The objectives of this project are:

ii) Development of a heterogeneous phantom for proton range measurements

- Design and manufacture of phantom; the phantom materials based on water-equivalent materials developed by Lourenço *et al.* (2017) [90] as well as commercial tissue-equivalent materials (bone and lung) [91].
- Development of a testing protocol and design tests to assess the phantom detector for accurate range measurement, as well as testing of phantom to ensure it meets the required acceptable proton phantom criteria defined in section 1.2.3.2.

iii) Development of an optimised head and neck phantom with patient-weight variation feature for proton therapy

- Design and manufacture of a head and neck phantom (made from proton optimised tissue-equivalent materials) to include a weight-loss feature to

assess the effects of anatomical changes on the patient's treatment dose distributions.

- Development of a testing protocol and design tests to assess the phantom detectors for accurate dose and dose distribution measurement, as well as testing of the phantom to ensure it meets the required acceptable proton phantom criteria defined in section 1.2.3.2.

1.3. Novel contribution of this work

This work has looked to contribute towards improving the accuracy of proton therapy audits, through a series of novel contributions during my PhD:

i) Investigation of proton optimised tissue-equivalent materials

While previous work has focused mainly on the development of photon and electron tissue-equivalent materials [52,56] or the development of proton water-equivalent materials for nuclear interactions [90], this work has developed an original cost-function model for the formulation of optimised tissue-equivalent materials by considering both photon and proton interactions. This model enabled a range of novel bone and muscle-equivalent plastics to be produced and characterised experimentally with CT imaging and proton high energy scanning beam measurements, as well as Monte Carlo simulations for use as clinical phantom materials. The best novel formulations were shown to mimic mass density, stopping power, and mass attenuation properties within 2% uncertainty along with further reducing the uncertainty in other key radiation properties (scattering and nuclear interactions).

ii) Development of a heterogeneous phantom for proton range measurements

Previous work has highlighted that EBT3 film can provide range measurements within proton therapy beams [92,93]. In this work, EBT3 film was implemented in a bespoke heterogenous phantom (e.g solid water, bone, and lung-equivalent materials) to assess treatment planning system range predictions against measurement. Using Monte Carlo and experimental measurements, EBT3 film measurements were shown

to provide repeatable simple depth dose measurements with an average relative uncertainty of 0.5% at the R_{80} depth. In addition, a range calibration factor (1.012 ± 0.002) between optical density and dose for R_{80} values was proposed for range measurements within a 115 MeV scanning proton beam. This is the first phantom prototype developed for range verification within a proton dosimetry audit setting.

iii) Development of an optimised head and neck phantom with patient-weight variation feature for proton therapy

The oropharyngeal site is challenging to treat and differing planning approaches are applied when it comes to clinical treatment plans. To date, head and neck phantoms developed for proton therapy have either tested a different clinical site or used photon-equivalent phantoms materials in the phantom design [37,72,80]. This work has developed a novel PRoton heaD and NeCk Evaluation phantom (PRuDeNCE) to assess the accuracy of treatment to the oropharyngeal site (with inclusion of weight-loss feature). The phantom is made of proton optimised tissue-equivalent materials to ensure accurate dosimetry measurements. The phantom includes internal dosimeters to provide absolute dose and relative dose distribution measurements. The phantom has been tested as part of a national end-to-end pilot audit study. The results showed 2% agreement between ionisation chamber and alanine within the clinical target volume (CTV) region to treatment planning system predictions, while film analysis showing a >95% pass rate for 4%/3 mm gamma analysis (global and local) for both proton therapy centres where the phantom was tested. This phantom will provide quality assurance support for the first national proton trial of oropharyngeal cancer.

2. Development of a heterogeneous phantom to measure range in clinical proton therapy beams

The work presented in this chapter has been published in Physica Medica:

Cook H., Lambert J., Thomas R., Palmans H., Hussein M., Clark C.H., Royle G., Pettingell J., & Lourenço A. Development of a heterogeneous phantom to measure range in clinical proton therapy beams. Physica Medica **93**, 59-68, (2022)

It has also been presented at the following conferences via oral and poster format:

Cook H., Lambert J., Thomas R., Palmans H., Hussein M., Clark C.H., Royle G., Pettingell J., & Lourenço A. Development of RALPH (proton RAnge Length PHantom) for proton range uncertainty audit. 58th Annual conference of the particle therapy co-operative group 2019; *Manchester, U.K. (Oral Presentation)*

Cook H., Lambert J., Thomas R., Palmans H., Hussein M., Clark C.H., Royle G., Pettingell J., & Lourenço A. Measurement of range uncertainties using radiographic film and a bespoke phantom. Proton Physics Research Implementation Group Workshop 2019; *Teddington, U.K. (Poster Presentation)*

My contribution to this publication were as follows; development of phantom design and setup protocol, electron experiments at National Physical Laboratory (NPL) and proton experiments at Rutherford Cancer Centres (South Wales and North East) were performed by me with the assistance of NPL staff and clinical centre

medical physics staff; analysis and interpretation of the results and Monte Carlo simulations were performed by myself under guidance of my supervisors and NPL staff; the paper was written by me and proof read by the co-authors.

2.1 Introduction

Although the finite range of protons is a key advantage of proton beams compared to photon beams for radiotherapy, it is also one of the main sources of uncertainty. Due to the way protons interact with matter, varying human tissue types can result in significant changes to range within the patient. A comprehensive study of range uncertainties by Paganetti [35] identified multiple sources that contribute to this uncertainty including patient imaging, patient anatomical changes, and dose calculations, [35] and reasoned the overall range uncertainty to be the combination of a 2.7% relative uncertainty and an absolute uncertainty of 1.2 mm. Figure 2.1 provides a schematic of sources that contribute to range uncertainty [94].

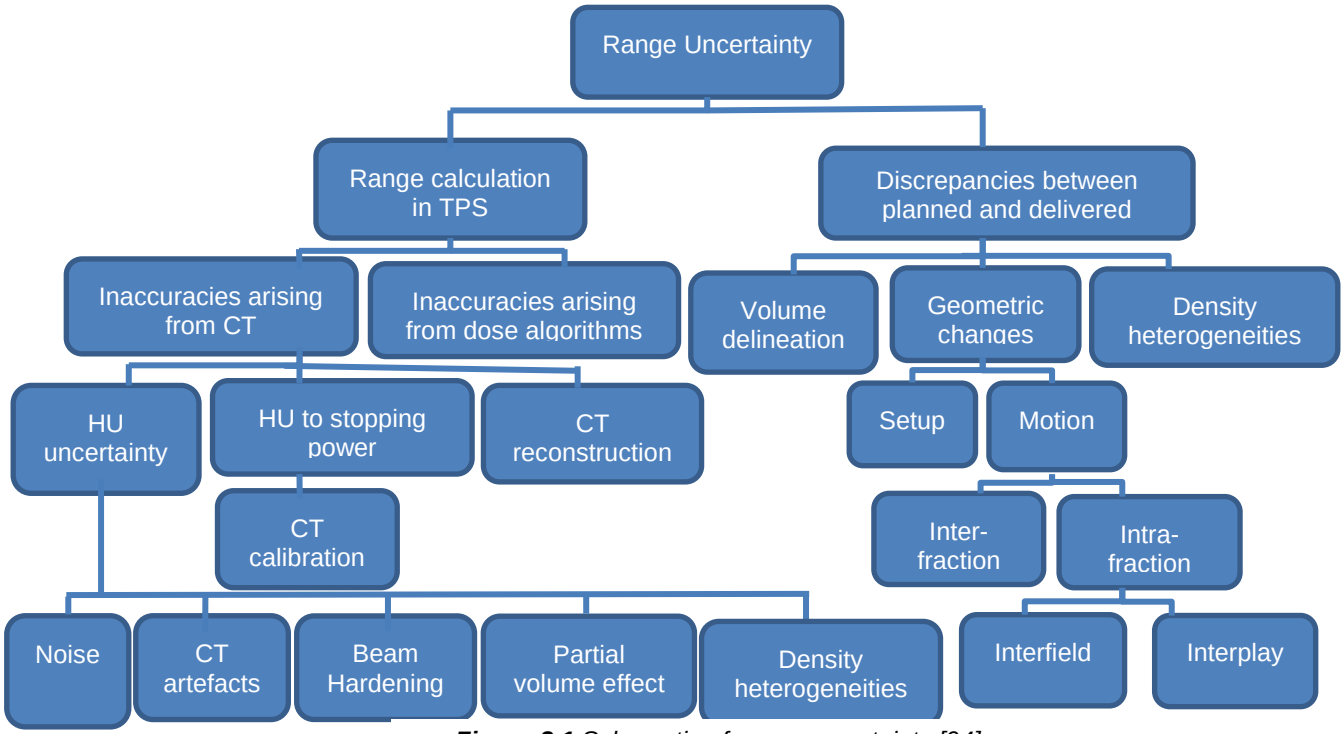

Figure 2.1 *Schematic of range uncertainty [94]*

As a consequence of range uncertainty, a large clinical margin is applied to proton treatment plans to guarantee full coverage of the tumour. Clinical margins vary between centres but typically a cautious 3.5% of the range plus an additional absolute value depending on the site is applied [35]. Furthermore, robust planning techniques and specific beam selection are typically applied, such as selecting multiple beam angles that do not pass through regions of daily patient variability [95]. This approach tries to ensure the clinical target is accurately covered without delivering unwanted dose to neighbouring OAR. Due to these constraints used in planning techniques and large clinical margins, the full potential of proton therapy is not exploited. Therefore, range verification is clinically highly desirable to be able to establish estimates of range uncertainties in proton therapy.

A variety of approaches are in development for on-line range verification including *in vivo* beam monitoring such as through the use of Positron Emission Tomography (PET) and prompt γ ray detection [96]. However, many of the solutions are still in the research stage and not yet implemented in clinical centres. Until on-line range verifications methods are clinical available, the use of phantoms could provide an insight into the measurement of the range within a heterogenous scenario by an off-line method.

As proton range estimation is a main source of uncertainty, it is important to validate range measurements in more realistic and complex phantom geometries to enable the evaluation of the full patient workflow as a means of an end-to-end audit [97]. For proton therapy, most audit phantoms are anthropomorphic in design; including IROC head, paediatric spine, liver, lung and prostate phantoms as well as

the CIRS head phantom [37,65,68]. The use of anthropomorphic phantoms for the purpose of dosimetric audit should mimic the full treatment workflow (imaging, treatment planning and dose delivery) and provide detailed information about the dose distribution by using embedded dosimeters. Although absolute dose and homogeneity of the dose is typically measured in existing audits [37,68], proton range is not quantified due to the complexity of range measurements within the phantom's design. Typically, only the lateral beam profile is investigated [37].

Audit work by Taylor *et al.* (2016) highlighted that although proton centres are typically able to achieve acceptable dose to the tumour target, errors in range calculation impacts many phantom audits [68]. Kim *et al.* (2018) used a CT calibration phantom to investigate range accuracy of a TPS dose algorithm and Monte Carlo simulation against measurements for eight different tissue-equivalent material rods [98]. They found range prediction accuracy for heterogenous tissues, in particular lung tissue, to be worse for the TPS, compared to the Monte Carlo simulations. Consequently, methods to independently verify range should be an essential part of any multi-centre dosimetry audit for proton therapy.

Currently, range measurements are typically performed with an ionisation chamber in a water phantom or with the use of array based detectors placed behind slabs of either water, tissue-substitute materials or real biological tissues [99]. But radiochromic film has also been previously shown to have potential as a detector for measuring proton range [93,100] and the response of different types of radiochromic film (MD 55, MD 55 2, HD 810, EBT, EBT2, EBT3, EBT XD films) in proton beams has been well documented [92,93,100–102].

In this work, radiochromic film was proposed for range measurements as it allows quick and easy determination of a full 2D distribution with high spatial resolution within one irradiation [103]. A bespoke Range Length Phantom (RaLPh) has been developed specifically to measure proton range using radiochromic film within a dosimetry audit setting. The key point of our design is a phantom which allows testing of a variety of material configurations, including bone and lung density interfaces to mimic complex clinical scenarios. This work tests whether EBT3 film can provide accurate range measurements within an heterogenous phantom in a scanning proton therapy beam. Validation measurements were performed by Monte Carlo simulations as well as ionisation chamber measurements to provide confidence in the film measurements. To the best of our knowledge, this is the first phantom prototype developed for range verification within a multi-centre dosimetry audit setting.

2.2. Methods and materials

2.2.1. Phantom Design

The RaLPh phantom was developed to be compact in design for simple and easy setup to enable efficient imaging and irradiation. The phantom was made of stacked 10 x 10 cm^2 slabs comprising a total length of 12.5 cm. The first 2.5 cm of the phantom can be interchanged with different combinations of water-equivalent material, lung, and bone substitute material plates (Figure 2.2 a). The remainder of the phantom is made of water-equivalent material; the blocks were arranged to enable a 10 cm x 10 cm piece of radiochromic film (EBT3, Gafchromic^{TM}, Ashland Inc. Wayne, NJ, henceforth referred to as EBT3 film) to be placed parallel to the beam, behind the variable section of the phantom (Figure 2.2 b). The phantom is encased in a PMMA

frame to keep the blocks tightly packed together to avoid air gaps between them as well as to ensure setup reproducibility (Figure 2.2 a). Laser alignment markers were positioned on the PMMA frame sides and top of the phantom to allow for easy positioning and identification of the centre point of the phantom.

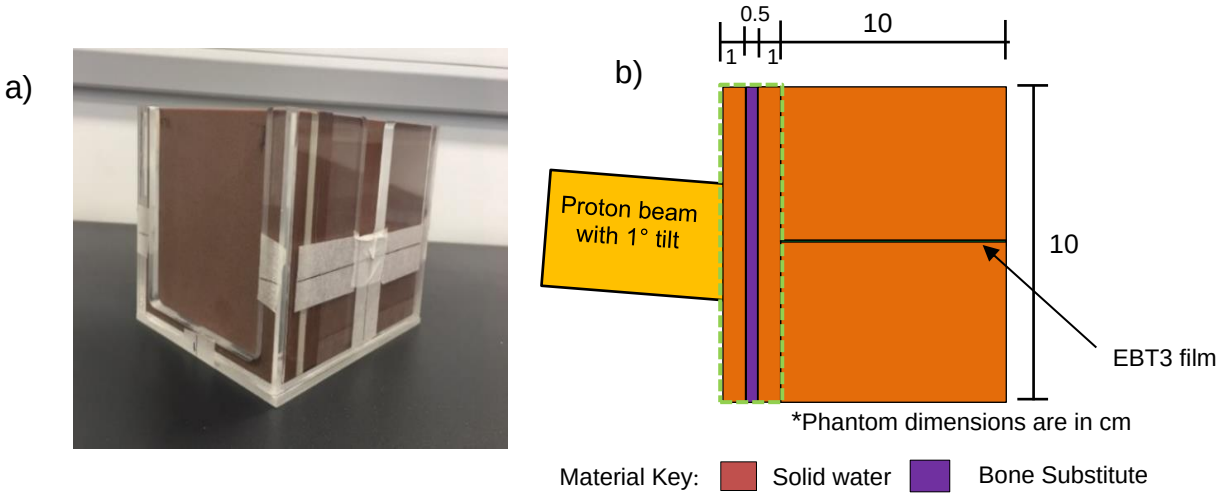

Figure 2.2 *a) RAnge Length PHantom (RaLPh), b) Schematic diagram of RaLPh with an example configuration. The varying tissue substitute configuration is shown in green box on diagram. Thickness of EBT3 is nominally 278μm)*

The solid water-equivalent materials (SW 1471 and SW 1472, BARTS Health NHS Trust London, UK) used in the phantom were epoxy resin based plastics and were previously optimised to match the proton nuclear interaction cross sections of water [90]. Both were shown to provide better water-equivalence in terms of proton fluence compared to commercial solid water-equivalent materials [14]. While it was concluded that SW 1472 was the most water equivalent, it is inhomogeneous due to the practicalities of mixing compounds into the epoxy resin mixture, which results in batch variability that impacts the measured range and TPS calculations. Therefore, the more homogenous SW 1471 was also considered in this study, despite it being less water equivalent in terms of fluence (within 1% for a maximum depth of 10 cm)

[90]. Consequently, this study investigated the feasibility and limitations of using the two different solid water types within RaLPh (Figure 2.3 a).

Figure 2.3b shows the tissue substitute materials used in the interchangeable section of the phantom which consisted of: SW 1471 (ρ =0.96 g/cm^3), SW 1472 (ρ = 1.04 g/cm^3) as water substitute materials, hard bone (SB5, Leeds Test Objects (UK), ρ = 1.86 g/cm^3) and Accura Bluestone (AC, 3D Systems Corporation, ρ = 1.76 g/cm^3), as bone substitute materials, and LN 330, Leeds Test Objects (UK) (lung inhale (L), ρ = 0.23 g/cm^3) as lung substitute material [91,104]. SB5 and LN 330 are commercial tissue-equivalent materials for photons while Accura Bluestone is a 3D printable material. The measured material density of the slabs was calculated by weighing them on a Mettler Toledo analytical balance (Model PG503 S) and performing length measurements with Mitutoyo Absolute IP 67 digital callipers (Model CD 8PSX).

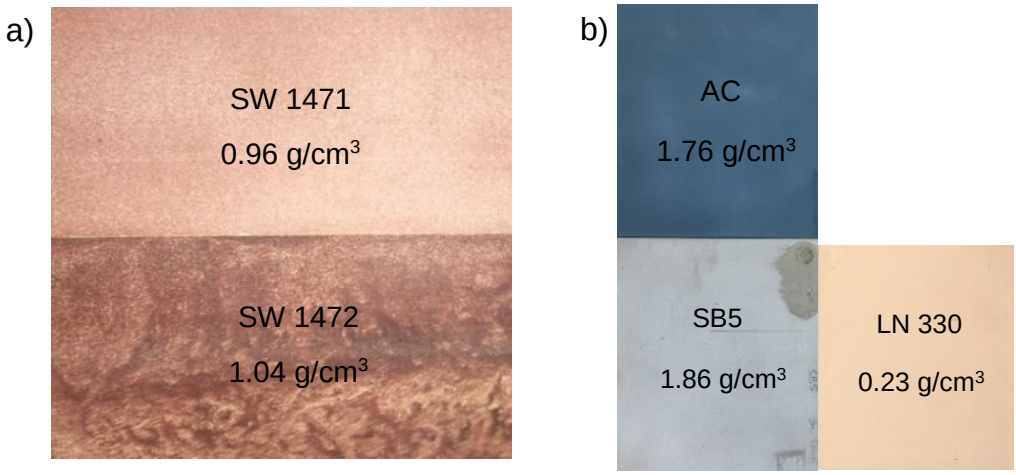

Figure 2.3 *a) Homogeneity comparsion between SW 1471 and SW 1472 b) Tissue substitute materials used in the RaLPh phantom. The non-uniformities observable on the material surfaces reflect heterogeneities except the dark grey marks on SB5 which are minor surface contamination.*

Table 2.1 shows the seven different material configurations tested experimentally in the variable section of the phantom. The configurations listed in Table 2.1 were

tested using both SW 1471 and SW 1472, hence, 14 configurations were considered in total.

Table 2.1 *Configurations tested in the variable section of the phantom. SW = Solid water (SW 1471 or SW 1472), SB5 = Hard bone, AC = Accura Bluestone, and Lung = LN 330*

Configuration (n)	Plates used in variable section of phantom
1	1 cm SW+ 0.5 cm SW + 1 cm SW
2	1 cm SW+ 0.5 cm SB5 + 1 cm SW
3	1 cm SW+ 0.5 cm AC + 1 cm SW
4	1 cm SW + 0.5 cm Lung + 1 cm SW
5	1 cm SW+ 0.5 cm SB5 + 0.5 cm Lung + 0.5 cm SW
6	1 cm SW+ 0.5 cm SB5 + 0.5 cm AC + 0.5 cm SW
7	1 cm SW + 0.5 cm SB5 + 0.5 cm Lung + 0.5 cm AC

2.2.2. EBT3 film range measurements with RaLPh

Film range measurements were performed in both electron and proton beams. Due to the similarity between electron and proton stopping powers, a preliminary study was performed with an electron beam at NPL to quantitatively test the phantom before using it as a proton audit device. Further details on the electron measurements can be found in the Appendices, section A.

2.2.2.1. Film handling, post-processing, and readout

All EBT3 films were handled following radiochromic film guidelines and best procedures to reduce film, scanner, and film-scanner uncertainties [105,106]. The following procedures were used to reduce film uncertainities; gloves were worn when handling the EBT3 film, EBT3 pieces were cut from the central region of each sheet

to reduce film hetergonieties, and kept in envelopes before and after irradiation to reduce light induced signal before scanning.

After irradiation, all the EBT3 films were scanned using an Epson Expression 10000 XL flatbed scanner after at least 24 hours post proton irradiation [103,106,107]. The scanner calibration was completed by the film calibration process, as this procedure calibrates the scanner signal to dose. The scanner bed was cleaned with ethanol before read-out of the films and warmed up by running five empty scans to ensure the scanner lamp is warm and stable before scanning of the film. To reduce film-scanner uncertainties, the EBT3 films were positioned in the centre of the scanner bed, scanned in the same orientation (short edge of EBT3 film perpendicular to scanning direction) to reduce scanning orientation effects and a glass compression plate was applied onto the EBT3 films before scanning [108]. One preview scan was performed on each EBT3 film before they were scanned and saved as 48-bit colour images with a resolution of 150 dpi in a TIFF image format. All colour corrections options were disabled to prevent the scanner software applying adjustments to the film scan data [109]. EBT3 films were analysed with FilmQA Pro 2016 software (Ashland Inc. Wayne, NJ, USA). For this study, a lateral scanner correction was not implemented in the FilmQA Pro 2016 software, as the film piece was scanned in the central region of the scanner (10 cm width) where the lateral response artefacts are negligible [110].

2.2.2.2. Calibration for EBT3 film

A calibration curve is required for film measurements due to the non-linear relationship between optical density and dose [105]. The optical density (OD) was determined from each pixel value for each colour channel by [111]

$$\mathrm{OD} = \log_{10}\left(\frac{\mathrm{I}_0}{\mathrm{I}}\right)$$

where I is the incident light intensity from the scanner and I_0 is the transmitted light intensity.

Calibration of the EBT3 film against an ionization chamber was performed by acquiring an eight-point calibration curve between dose and OD (Figure 2.4).

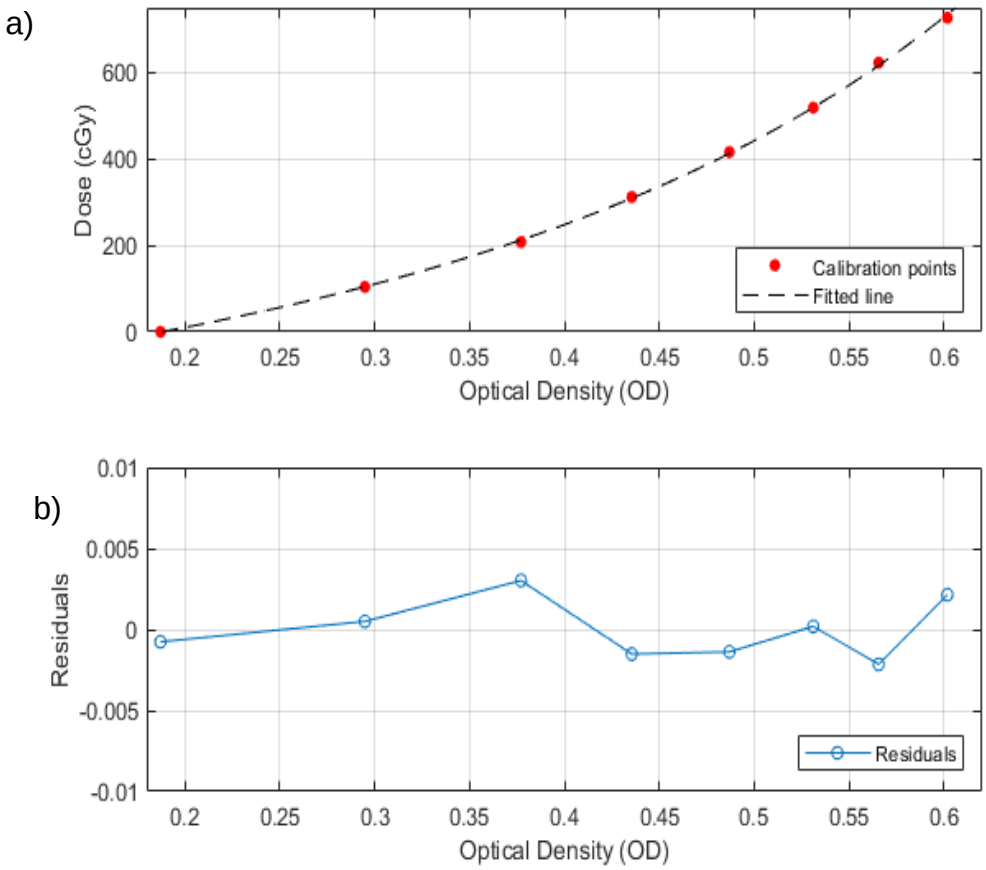

Figure 2.4: *a) Calibration curve (Dose vs OD) for the red channel, b) Residuals between calibration point values and fitted response*

The EBT3 film calibration was performed in solid water; a PTW Roos chamber 34001 (PTW dosimetry, Freiburg, Germany) operated at -400 V was placed in a Gammex HE solid water holder with the EBT3 film positioned on top of the chamber and a 2 cm of solid water (RW3 (IBA Dosimetry, Schwarzenbruck, Germany)) as build up. A single mono-energetic layer of 115 MeV with a 10 x 10 cm^2 field was applied vertically. The calibration was performed in the plateau region of the proton depth dose profile; the gradient correction factor (1.005 for 115 MeV in water) between the film and chamber was not applied as the difference was believed to not affect the relative depth dose measurements needed for range determination. A single 10 x 10 cm^2 piece of EBT3 film was used for each measurement and fiducials were marked on the EBT3 film before irradiation to align the EBT3 film and the ionisation chamber. Dose to water, $D_{w,Q}$, was derived from the ionisation chamber measurements following the recommendations of IAEA TRS 398 Code of Practice [21]:

$$D_{w,Q} = M_Q N_{D_w,Q_0} k_{Q,Q_0} \tag{2.1}$$

where M_Q is the ionisation chamber reading corrected for temperature, pressure, the polarity effect, and ion recombination, N_{D_w,Q_0} is the absorbed dose to water calibration coefficient in a ^{60}Co beam and k_{Q,Q_0} is the beam quality correction factor. Ion recombination was determined via the two voltage method (-100 V and -400 V) for a pulsed proton beam [21].

A central square region of interest (3.4 x 3.4 cm^2) was positioned directly over the projected area of the ionisation chamber's sensitive volume (with a radius of 0.78 cm) for each calibration EBT3 film piece and the average scanner signal determined over this region. The following function was fitted to the data:

$$X(D) = \frac{(a+b)}{(D-c)} \tag{2.2}$$

where $X(D)$ is the scanner response at dose (D), $a, b,$ and c are the fitting function constants. Separate film calibrations were performed for the beam tilt measurements (section 2.2.2.3.1.) and for the film irradiation (section 2.2.2.3.) in the variable phantom configurations. The same experimental setup and film analysis procedure were used for both proton beam calibrations.

2.2.2.3. EBT3 film irradiations for variable phantom configurations

All proton measurements were performed at a Rutherford Cancer Centre, UK, equipped with a IBA Proteus 230 MeV proton synchrocyclotron. RaLPh was tested using a 115 MeV mono-energetic scanning proton beam to allow the proton beam to stop in the centre of the EBT3 film at around 10 cm depth in the phantom. The field size applied was a 4 x 4 cm^2 delivering 289 spots (0.65 Monitor Units (MU)/spot) resulting in a dose of 5 Gy at the Bragg peak.

For the variable phantom configuration measurements, the front face was initially set up perpendicular to the beam and the isocentre was aligned with the front edge of the phantom. A one-degree gantry tilt was applied to avoid the tunnelling of the protons through the gap containing the EBT3 film. To enable repeatable positioning after configuration changes throughout the experiment, the phantom was positioned against a treatment indexing bar to ensure the orientation of the front face remained fixed to the beam as well as position markers were drawn around the phantom. These allowed to keep the front face of the phantom at the same angle of 89 degrees to the

beam throughout the measurements. Each setup shown in Table 2.1 was repeated four times on separate EBT3 films.

2.2.2.3.1. Beam tilt measurements

A study was undertaken to assess if beam tunnelling influences proton range measurements within the phantom. Previous research has shown that a tilt is required for film measurements when film is parallel to the beam within a phantom to prevent dosimetric artefacts due to the protons tunnelling through a possible air gap [100,101]. An optimal degree of tilt has yet to be established, but work by Zhao and Das suggest a tilt as little as 1 degree can reduce tunnelling effects [100]. This study was performed to assess the optimal degree tilt to be used with RaLPh.

The proton beam delivery was performed with the same settings as stated in section 2.2.2.3. SW 1471 configuration 1, as described in Table 2.1, was used throughout the experiment. A customised RaLPh bed (Figure 2.5) was developed to avoid movement of the phantom on the treatment couch when a tilt was applied. A series of different tilt angles were applied to the phantom/couch, the gantry, or both; 0 to 5 degrees of couch tilt, 1 to 5 degrees of gantry tilt (both with 1-degree intervals) and 5 degrees of couch tilt and 5 degrees of gantry tilt in the opposing direction (resulting in a total tilt of 10 degrees). The latter was considered as the couch tilt was limited to a maximum of 5 degrees. It should be noted that the 10-degree tilt was performed as an exaggerated tilt condition to investigate the impact of larger degrees of tilt on range.

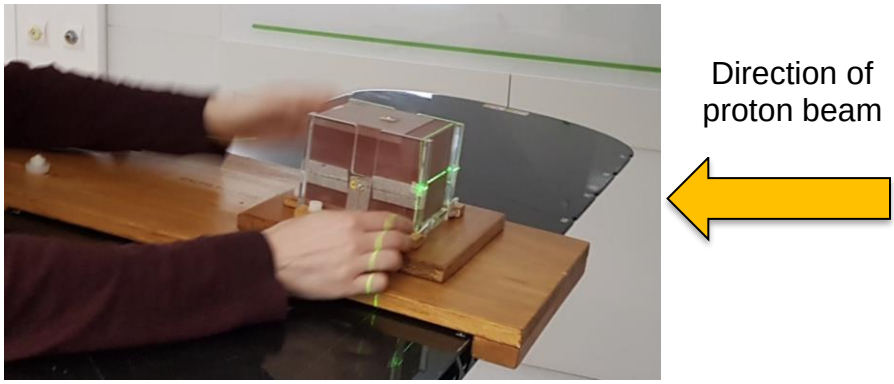

Figure 2.5 *RaLPh in the customised bed for tilt measurements*

2.2.2.4. EBT3 film analysis

For all film analysis, the film was cropped and aligned using FilmQA Pro 2016 software settings. The central horizontal axis was determined by calculating the distance between the top and bottom edge of the film with the cursor function. The horizontal line tool was then used to obtain the central horizontal axis optical density (OD) or dose profile (Figure 2.6 a) and 2.6 c)) which averaged the profile over a 9-pixel width. The start position of the film was defined where the first dose value was measured along the horizontal axis. The range of the proton beam was then obtained in two ways; firstly, from the OD profile on the central horizontal axis (see Figure 2.6 b)), secondly after the film calibration was applied, from the depth dose profile on the same central horizontal axis (see Figure 2.6 d)). No correction for signal quenching was applied as previous research as shown that range can be determined from the uncorrected depth dose profiles [100]. The impact of minor positioning errors was investigated as well as its impact on the derived range. Results showed minor deviations which were within the 0.5% film positioning uncertainty value with respect to the phantom given for each setup.

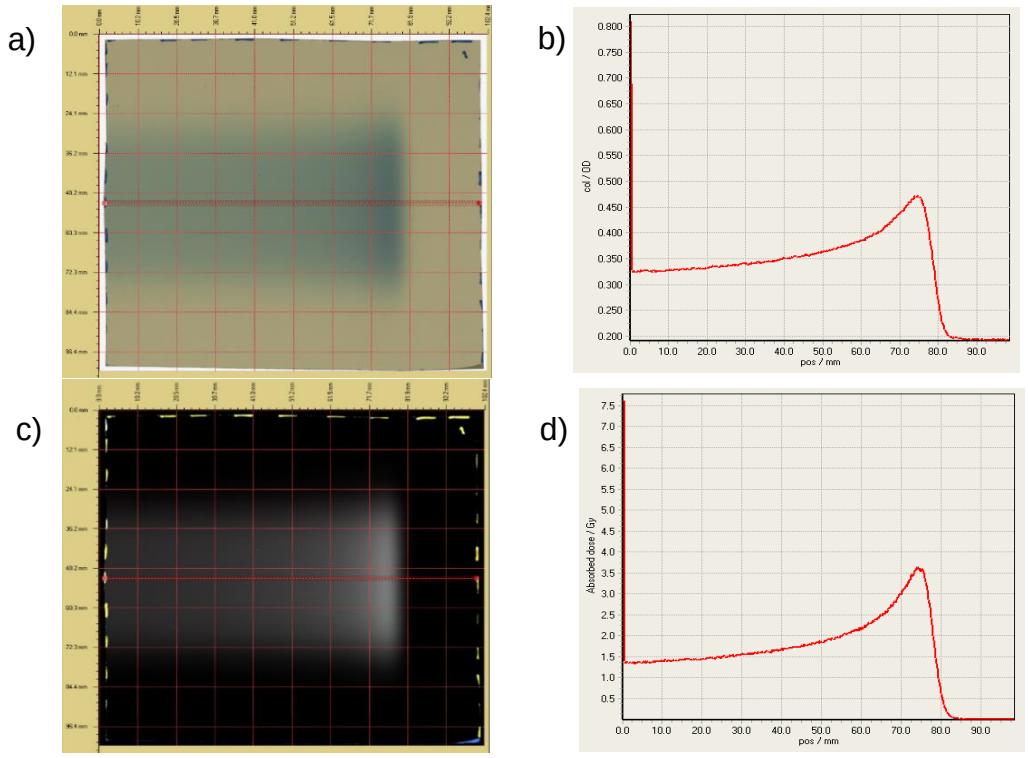

Figure 2.6 *a) Image of irradiated film, b) Example of the depth OD profile obtained with film, c) Image of irradiated film after calibration is applied, d) Example of depth dose profile obtained with film*

The proton range was defined as R_{80}, the depth distal to the Bragg peak where the percentage depth dose drops (PDD) to 80%. The R_{80} range was chosen instead of the R_{90} range due to it being associated with the mean projected range of the protons as well as being independent of the beam's energy spread [35] for the setup.

The position of the peak was calculated by determining a 2nd order polynomial fit of the points around the peak value and the results were then normalised to the peak value to determine the distal R_{80} depth of the curve. The R_{80} value was then interpolated from a linear fit around the 80% dose of the distal edge of the profile. The red channel was used for the OD analysis because it exhibits the highest absorption

from the three colour channels [112]. For the dose profiles, the red channel was also used, the multichannel optimisation setting automatically corrected the red channel for film variations through use of information from the other two colour channels; this algorithm is described in [113]. The multichannel method has been shown to reduce the uncertainty due to EBT3 film variations including artefacts, varying thickness of the active layer, scanner nonlinearity and noise [112]. A comparison of the range values was carried out to investigate if a range calibration factor could be determined for EBT3 film range measurements. The use of only the OD profiles would provide improved efficiency for the audit process by not requiring a film calibration (section 2.2.2.2.).

2.2.3. Validation of EBT3 film measurements

Proton beam film measurements were validated by comparing the results with ionisation chamber measurements and Monte Carlo simulations.

2.2.3.1. Ionisation chamber measurements

Ionisation chamber (IC) measurements were performed to determine the water-equivalent thickness ($\mathrm{WET_m}$) and relative water-equivalent thickness ($\mathrm{rWET_m}$) of the materials (m) used within RaLPh, using equations 2.3 and 2.4, respectively [3].

$$\mathrm{WET}_m = R^{\mathrm{IC}}_{80,\mathrm{w}} - R^{\mathrm{IC}}_{80,\mathrm{w,m}} \tag{2.3}$$

$$\mathrm{RSP} \approx \mathrm{rWET_m} = \frac{\mathrm{WET_m}}{t_{\mathrm{m}}} \tag{2.4}$$

$R_{80,\mathrm{w}}^{\mathrm{IC}}$ corresponds to the range in water, $R_{80,\mathrm{w,m}}^{\mathrm{IC}}$ is the range in water when including the material slab in front of the water phantom and t_{m} the thickness of the material slab.

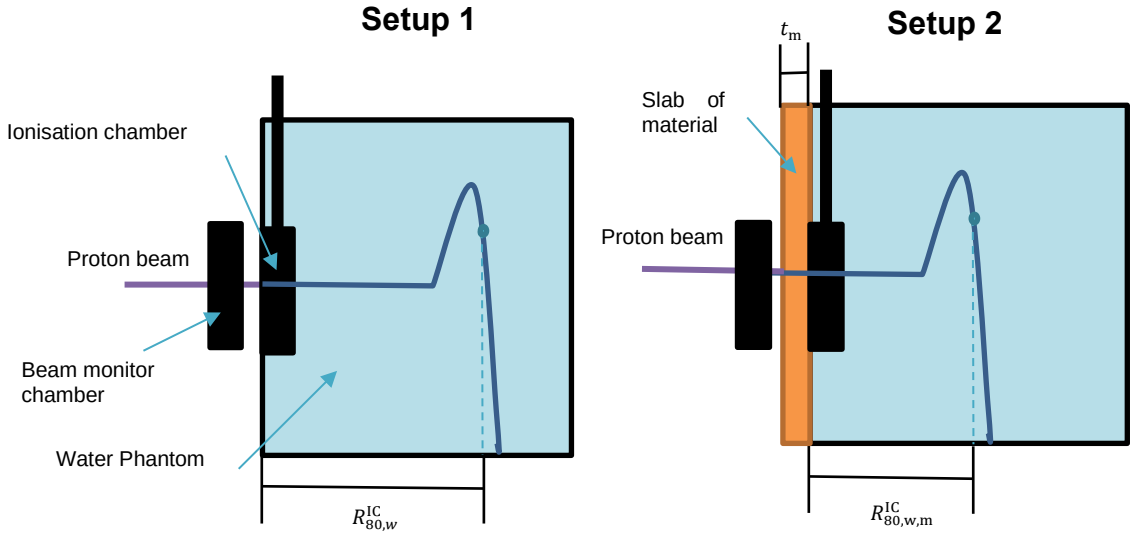

Figure 2:7 *Two water phantom setups Left: Setup 1 – without RaLPh materials, and Right: Setup 2, RaLPh material in front of water phantom) considered in the ionisation chamber experiments and the Monte Carlo simulations.*

A water phantom was setup with a large area PTW Bragg peak chamber 34070 operated at –400 V positioned 0.5 mm from the internal front face of the water phantom and an external PTW beam monitor chamber 7862 was positioned in front of the beam right in front of the water phantom, and its signal used for normalisation. The Bragg peak chamber was moved from the front face of the water phantom in 1 mm steps until the distal fall off region of the beam so that the whole percentage depth ionisation (PDI) curve could be measured with the ionisation chamber (Figure 2.7, Setup 1). The PDI measurement was repeated in smaller steps of increment (0.2 mm) around the Bragg peak to determine a more accurate R_{80} value. The $\mathrm{PDI_w}$ curve was measured for a mono-energetic 115 MeV pencil beam in water and then slabs of solid water (1 cm), lung (0.5 cm) and bone substitutes (0.5 cm) were placed individually in front of

the water phantom and for each configuration the new $\mathrm{PDI}_{\mathrm{w,m}}$ was measured (Figure 2.7, Setup 2). Bragg Peak chamber and beam monitor ratio calculated as this accounts for any beam variations. The determination of ranges $R_{80,\mathrm{w}}^{\mathrm{IC}}$ and $R_{80,\mathrm{w,m}}^{\mathrm{IC}}$ by the interpolation of the PDI followed the same approach as range determination method described in section 2.2.2.4

2.2.3.2. Empirical determination of solid water scaled depths

An empirical method was used to derive the R_{80} ranges for each phantom configuration (Table 2.1). The method applied the RaLPh material $\mathrm{WET}_{\mathrm{m}}$ and $\mathrm{rWET}_{\mathrm{m}}$ values calculated from the ionisation chamber measurements (section 2.2.3.1.). The method empirically determined the R_{80} ranges for each configuration (Table 2.1) by calculating the range shift caused by using tissue-equivalent materials within the variable section of the phantom compared to the solid water only configuration. These independently derived ranges were then compared with the EBT3 film measurements (section 2.2.2.3.) to validate the film range results.

To understand the empirical determination of solid water scaled depth, the key equations with regards to $\mathrm{WET}_{\mathrm{m}}$ measurements are defined below. In IAEA TRS-398 report [21], the following equation for scaling the depths of plastics materials, m, to water-equivalent depths, w is defined in equation ..

$$z_{\mathrm{w}} = z_{\mathrm{sw}} c_{\mathrm{pl}} \tag{2.5}$$

where z_{sw} is the depth in the solid water plastic (in gcm^{-2}), z_{w} is the depth in water (in gcm^{-2}), and c_{pl} is the depth scaling factor, defined by the ratio of the ranges (in

g/cm^2) in water, $R_{\mathrm{w}}^{\mathrm{MT}}$, and in the solid water plastic, R_{sw}^{MT} (note that the superscript MT is used to denote the ranges are defined in mass thickness units).

$$c_{\mathrm{pl}} = \frac{R_{\mathrm{w}}^{\mathrm{MT}}}{R_{\mathrm{sw}}^{\mathrm{MT}}} \tag{2.6}$$

Equation 2.6 can be converted into units of cm and used to approximate the WET_{sw} of a solid water plastic.

$$t_{\mathrm{w}} = t_{\mathrm{sw}} \cdot \frac{\rho_{\mathrm{sw}}}{\rho_{\mathrm{w}}} c_{\mathrm{pl}} = t_{\mathrm{sw}} \cdot \frac{R_{\mathrm{w}}}{R_{\mathrm{sw}}} \tag{2.7}$$

where t_{w} (=WET) and t_{sw} are the thicknesses in water and in the plastic material respectively and R_{w} (=$R_{80,\mathrm{w}}^{\mathrm{IC}}$) and R_{sw} (=$R_{80,\mathrm{sw}}^{\mathrm{IC}}$) are the measured range with an ionisation chamber (IC) in water and solid water respectively.

$\mathrm{WET}_{\mathrm{sw}}$ measurements have been described in several publications [3,114–116] and can be determined by equation 2.3. Equation 2.3 can then be substituted into equation 2.8 instead of t_{w}.

$$R_{80,\mathrm{w}}^{\mathrm{IC}} - R_{80,\mathrm{w,sw}}^{\mathrm{IC}} = t_{sw} \cdot \frac{R_{80,\mathrm{w}}^{\mathrm{IC}}}{R_{80,\mathrm{sw}}^{\mathrm{IC}}} \tag{2.8}$$

The equation is then rearranged to calculate

$$R_{80,\mathrm{sw}}^{\mathrm{IC}} = \frac{R_{80,\mathrm{w}}^{\mathrm{IC}}}{\frac{R_{80,\mathrm{w}}^{\mathrm{IC}} - R_{80,\mathrm{w,sw}}^{\mathrm{IC}}}{\mathrm{t_{sw}}}} \tag{2.9}$$

Equation 2.9 can be simplified to

$$R_{80,\mathrm{sw}}^{\mathrm{IC}} = \frac{R_{80,\mathrm{w}}^{\mathrm{IC}}}{\mathrm{rWET_{sw}}} \tag{2.10}$$

Equation 2.10 was used to calculate the $R_{80,\mathrm{sw}}$ range for the solid water material. This equation provides the $R_{80,\mathrm{sw}}$ range of the proton beam through the solid water phantom configuration, determined using the ionisation chamber measurements.

To then calculate the range of the proton beam for the other phantom configurations, the solid water-equivalent thickness of each individual tissue-equivalent material tested was determined by using equation 2.4 and 2.10

$$t_{\mathrm{sw-eq,m}} = \frac{\mathrm{WET_m}}{\mathrm{rWET_{sw}}} \tag{2.11}$$

The solid water thickness of each heterogenous configurations (Table 2.1, configuration 2-7) was then determined. For example, configuration 2 with SW 1471:

$t_{\mathrm{sw-eq,m}}^{\mathrm{config.2}}$ = 1 cm of SW 1471 + 0.853 cm solid water equivalent thickness of SB5 + 1 cm of SW 1471

The solid water-equivalent thickness of each configuration $\mathrm{t}_{\mathrm{sw-eq,m}}^{\mathrm{config.n}}$, (Table 2.1, configurations 2-7) was then compared to the solid water only configuration, $\mathrm{t}_{\mathrm{sw-eq,m}}^{\mathrm{config.1}}$, (Table 2.1, configuration 1) to determine a solid water-equivalent thickness difference, $\Delta t_{\mathrm{sw-eq,m}}^{\mathrm{config,n}}$.

$$\Delta t_{\mathrm{sw-eq,m}}^{\mathrm{config,n}} = \mathrm{t}_{\mathrm{sw-eq,m}}^{\mathrm{config.n}} - \mathrm{t}_{\mathrm{sw}}^{\mathrm{config.1}} \tag{2.12}$$

The difference in solid water-equivalent thickness was then related to the change in depth of the solid water range for the heterogenous configuration. This enables the range in the heterogenous phantom configurations to be calculated via equation 2.13.

$$R_{80,\mathrm{sw,m}}^{\mathrm{config.n}} = R_{80,\mathrm{sw}} - \Delta z_{\mathrm{sw}}^{\mathrm{config,n}} \tag{2.13}$$

2.2.3.3. Monte Carlo Calculations

The RaLPh phantom was also modelled to derive ranges numerically by Monte Carlo simulations. The Monte Carlo derived ranges were then compared to EBT3 film measurements to provide validation of experimental measurements.

2.2.3.3.1. Beam Characterisation

The 115 MeV pencil proton beam in water was simulated using the Monte Carlo simulation. The Monte Carlo simulation parameters are summarised in Table 2.2. Dose was scored with a resolution of 0.01 cm within a cylindrical volume with a diameter equal to the sensitive area of the PTW Bragg peak chamber. The incident beam parameters (beam energy and energy spread) were tuned to achieve a match between the simulated and the 115 MeV beam's depth dose profile measured with the ionization chamber (described in section 2.2.3.1.).

Table 2.2: *Monte Carlo parameter for the beam characterisation simulation*

Item name	Description	References
Title	Beam characterisation for 115 MeV pencil beam	
Code and version	FLUKA 2011.2x.8 and Flair 2.3.0 codes	[24,117,118]
Geometry	Cylinder target = 30 cm in length and radius. The geometry was surrounded by vacuum.	
Materials	Liquid water (276 FLUKA water material card). I-value of water set to 78 eV by the material property card (MAT-PROP).	[119]
Source	Proton pencil beam. Energy = 114.79 MeV, energy spread = FWHM is 0.9 MeV, momentum spread = gaussian, divergence = 0 and beam shape (X and Y) = rectangular.	
Physics and Transport parameters	Default hadrotherapy (HADROTHErapy card) physics with full heavy ion transport (IONTRANS set to full transport).	

Table 2.2 continued

Scoring	Dose (URSBIN card), R–Φ–Z (no symmetry), length of scoring = 30 cm radius of scoring = 4.08 cm, number of R bins = 1, number of Φ = 1 and number of Z bins = 3000.	
Number of histories	7×10^6 primary protons.	
Postprocessing	Normalisation of dose profile to area under the curve.	

2.2.3.3.2. Material characterisation

The transport of the characterised beam was simulated through a setup that replicated the experiment described in section 2.2.3.1. The Monte Carlo simulation parameters are summarised in Table 2.3. The *I*-value of the different materials listed in Table 2.3 were determined by adjusted the value until the R_{80} range matched that of the ionisation measurements in section 2.3.1 within 0.01%. It should be noted that average density measurements were used for the solid water slabs (density values can be found in Figure 2.3).

Table 2.3: *Monte Carlo parameter for the material characterisation*

Item name	Description	References
Title	Material characterisation (RaLPh materials)	
Code and version	FLUKA 2011.2x.8 and Flair 2.3.0 codes	[24,117,118]
Geometry	Cylinder target 1 = 0.5 cm length and 30 cm radius. Cylinder target 2 = 30 cm in length and radius. Cylinder 2 follow on from Cylinder 1 in geometry. Both cylinders are surrounded by vacuum.	
Materials	Cylinder 1 material = RaLPh materials were inputted from their elemental composition and measured density data. The I-value of each material was tuned for each simulation (see table 2.4 for further details). Cylinder 2 material = Liquid water (276 FLUKA water material card).	[119]

Table 2.3 continued

	I-value of water set to 78 eV by the material property card (MAT-PROP).	
Source	Proton pencil beam. Energy = 114.79 MeV, energy spread = FWHM is 0.9 MeV, momentum spread = gaussian, divergence = 0, and beam shape (X and Y) = rectangular.	
Physics and Transport parameters	Default hadrotherapy (HADROTHErapy card) physics with full heavy ion transport (IONTRANS set to full transport).	
Scoring	Dose (URSBIN card), R–Φ–Z (no symmetry), length of scoring = 30 cm radius of scoring = 4.08 cm, number of R bins = 1, number of Φ = 1, and number of Z bins = 3000.	
Number of histories	7×10^6 primary protons.	
Postprocessing	R_{80} range was determined from the dose depth profile.	

Table 2.4 shows the *I*-values used in the RALPH variable configurations simulations. These values were derived by the method described in section 2.2.3.3.2.

Table 2.4 *I-values of RaLPh materials derived from Monte Carlo simulations*

Material	*I*-value
SW 1471	56.79
SW 1472	74.00
SB5	116.00
Accura Bluestone	89.00
Lung (LN 330)	100.60

2.2.3.3.3. Phantom simulations

The characterised beam and tuned material *I*-values were used in a box geometry surrounded by a vacuum that replicated the seven different phantom configurations

for the two types of solid water. The Monte Carlo simulation parameters are summarised in Table 2.5. These results were used to determine the range in the phantom and were compared to the EBT3 film measurements.

Table 2.5 *Monte Carlo parameter for the RaLPh configurations*

Item name	Description	References
Title	RaLPh configuration simulations	
Code and version	FLUKA 2020.0.3 and Flair 2.3.0 codes	[24,117,118]
Geometry	Replication of phantom geometry defined in section 2.2.1. The geometry was surrounded by vacuum.	
Materials	Material configurations defined in Table 2.1 were simulated. The materials composition, density, and I-values (Table 2.4) were defined for each material.	[61,91,104]
Source	Proton pencil beam. Energy = 114.79 MeV, energy spread = FWHM is 0.9 MeV, momentum spread = gaussian, divergence = 0, and beam shape (X and Y) = rectangular. A 4 x 4 cm^2 mono-energetic field was simulated.	
Physics and Transport parameters	Default hadrotherapy (HADROTHErapy card) physics with full heavy ion transport (IONTRANS set to full transport).	
Scoring	Dose (URSBIN card), R–Φ–Z (no symmetry), length of scoring = 12.5 cm radius of scoring = 1 cm, number of R bins = 1, number of Φ = 1, and number of Z bins = 3000.	
Number of histories	7×10^6 primary protons.	
Postprocessing	R_{80} was determined from the dose depth profile.	

2.2.4. RaLPh in a treatment planning workflow

The phantom was tested as an audit device by acquiring a CT scan of the phantom at the Rutherford Cancer Centre and performing TPS calculations to

determine the TPS predicted range. The TPS predicted ranges were then compared to the EBT3 film measurements.

2.2.4.1. CT scanning protocol

RaLPh was scanned with a Phillips Big Bore CT scanner. The following scanner settings were used; axial scan, tube voltage of 120 kV, voxel size of 0.117 x 0.117 x 0.1 cm^3, average tube current of 155 mA, helical reconstruction mode and scan reconstruction option of Brain. The 14 configurations tested were scanned in the CT scanner. Ball bearings were applied to the midpoints of the phantom surface to allow for correct alignment in the TPS.

2.2.4.2. TPS Calculations

The CT data were imported into Pinnacle^3 (version 16.0) to create a treatment plan and the proton range was calculated for the difference tested configurations. The plan was designed to replicate the experimental setup: a proton beam with a field size of 4 x 4 cm^2 delivering 289 spots field (0.650519 MU/spot) and the gantry was set to 89 degrees to apply the same tilt as in the experiments. A dose grid with a resolution of 0.1 cm^3 was applied for each plan. The HU to stopping power calibration curve for the specific scanner used was entered into Pinnacle^3 for the dose calculation. The depth dose profile was extracted as a line profile aligned with the beam axis with start and end point corresponding to the central coordinates of the phantom at the front face and the end of the phantom. The Bragg peak as well as range, R_{80}^{TPS}, were determined as in section 2.2.2.4. The density override option was also applied to the TPS plans by contouring the different materials and inputting the measured material density values (density values defined in section 2.2.1.) which in turn overrides the

RSP of the materials. It should be noted that averaged solid water density measurements were used in the density override option. TPS range predictions were then compared to the measured range values from the film measurements.

2.2.5. Summary of analysis

Figure 2.8 schematic summarises how measurements taken at the proton centre were implemented in the analysis process. $R_{80,\mathrm{D}}^{\mathrm{Film}}$ were compared to measured and/or calculated data to: i) validate the EBT3 film measurements and ii) to investigate the application of the phantom in the clinic.

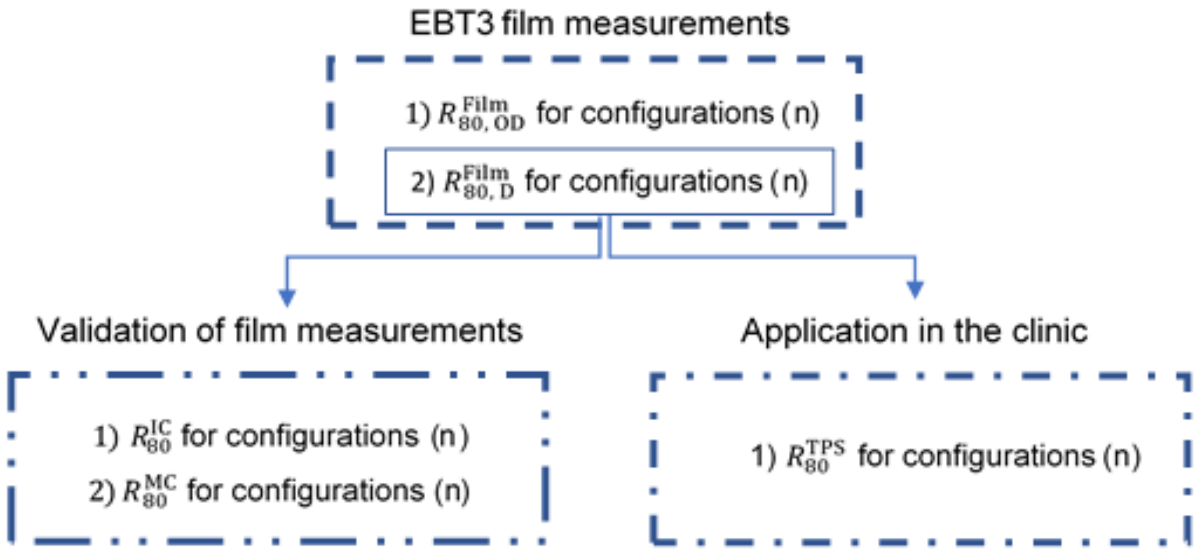

Figure 2.8 *Schematic of RaLPh measurements, calculations, and analysis, where n is the configuration number, $R_{80,OD}^{Film}$ are the R_{80} measurements from the depth OD profiles of EBT3 film, $R_{80,D}^{Film}$ are the R_{80} measurements from the depth dose profiles of EBT3 film, R_{80}^{IC} are scaled R_{80} values determined based on the ionisation chamber measurements, R_{80}^{MC} are the R_{80} values calculated from the depth dose profiles of Monte Carlo simulations and R_{80}^{TPS} are the R_{80} values calculated from the TPS depth dose profiles. , $R_{80,D}^{Film}$ values were compared to other range measurements and calculated data, this is shown via the straight line box and directional arrows shown in the schematic.*

2.3. Results

2.3.1. Beam tilt measurements

Table 2.6 shows the $R_{80,\mathrm{OD}}^{\mathrm{Film}}$ and $R_{80,\mathrm{D}}^{\mathrm{Film}}$ for the EBT3 film results for all the tilts considered in this study. In addition, the $\Delta R_{80,\mathrm{D}}^{\mathrm{Film}}$, was determined by calculating the difference in $R_{80,\mathrm{D}}^{\mathrm{Film}}$ ranges between zero-degree tilt and each specific degree tilt measurement. The results from Table 2.6 also show that no tunnelling effect was seen for zero-degree tilt. The standard variation of the in $R_{80,\mathrm{D}}^{\mathrm{Film}}$ range was shown to be within 0.3 mm with the largest variation in range being for the exaggerated 10 degrees tilt. A beam tilt range correction wasn't applied to range measurements. The correction was considered negligible as it was determined to be within the 0.5% uncertainty of the measurement.

The ratio between $R_{80,\mathrm{OD}}^{\mathrm{Film}}$ and $R_{80,\mathrm{D}}^{\mathrm{Film}}$ for the EBT3 film measurements is also provided. The results show that a range calibration factor could be applied to the depth-OD profiles as a constant value of 1.012 ± 0.001 mm which was found by the ratio of the OD and dose EBT3 film measurements at R_{80} value.

Table 2.6 *R_{80}range measurements from tilt setups considering the $R_{80,OD}^{Film}$ and $R_{80,D}^{Film}$ ranges for the EBT3 film measurements. As well as the ratio comparison between $R_{80,OD}^{Film}$ and $R_{80,D}^{Film}$.*

Degree of tilt	Tilt	$R_{80,OD}^{Film}$ (mm)	$R_{80,D}^{Film}$ (mm)	$\Delta R_{80,D}^{Film}$ (mm)	Ratio
0 degrees	Couch tilt	102.64	101.43	N/A	1.012
1 degree	Couch tilt	102.56	101.28	-0.2	1.013
2 degrees	Couch tilt	102.63	101.43	0.0	1.012
4 degrees	Couch tilt	102.70	101.64	0.2	1.010
5 degrees	Couch tilt	102.66	101.50	0.1	1.011
10 degrees	Couch tilt and Gantry	101.91	100.83	-0.6	1.011
5 degrees	Gantry	102.84	101.70	0.3	1.011
4 degrees	Gantry	102.51	101.27	-0.2	1.012
2 degrees	Gantry	102.57	101.31	-0.1	1.012
1 degree	Gantry	103.12	101.80	0.4	1.013

2.3.2. EBT3 film irradiations for variable phantom configurations

Figure 2.9 shows the average depth-dose profiles for the seven SW 1471 configurations (Figure 2.9a) and the seven SW 1472 configurations (Figure 2.9b). The average depth-dose profiles were calculated from the four repeat measurements of each configuration. The uncertainty for each measurement was the propagation of both the 0.5% relative standard uncertainty in positioning of EBT3 film in the phantom as well as the repeatability of measurement. All uncertainties are expressed as standard uncertainties (at 68% confidence level) and are presented in the error bars shown in Figure 2.9. The range of average relative standard uncertainty for all configurations was between 0.50 – 0.58%.

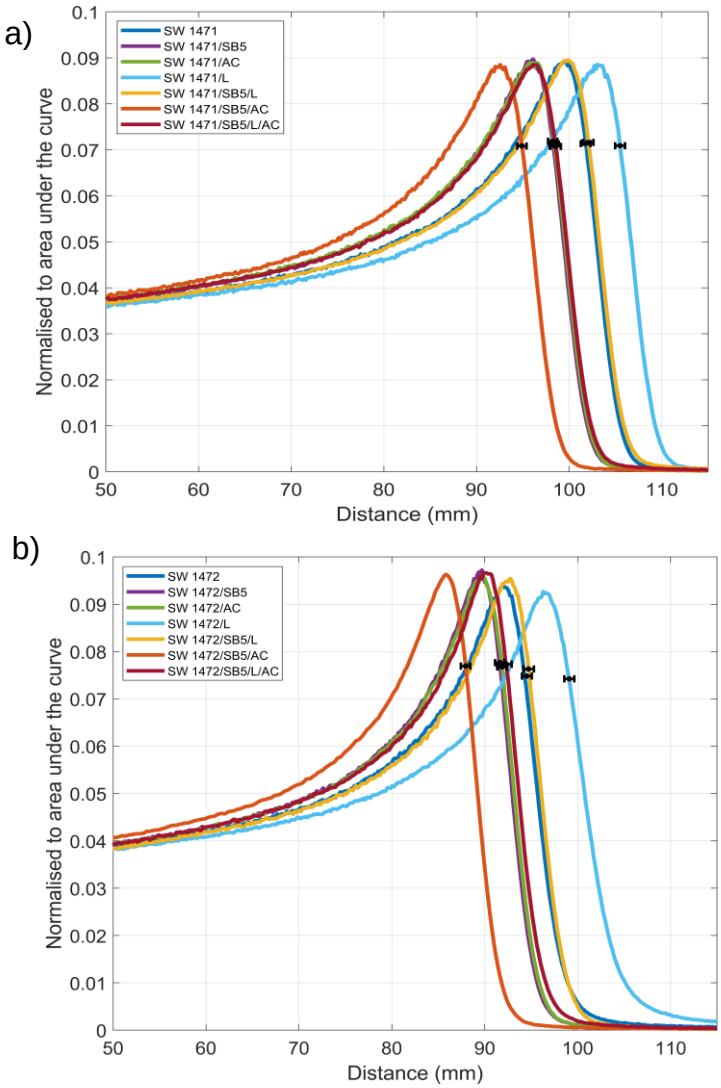

Figure 2.9 *Average depth-dose profile for a) SW 1471 configurations and b) SW 1472 configurations, normalised to the area under the curve. The points on the profiles are the* R_{80} *for each configuration.*

Table 2.7 shows the R_{80} values calculated from the depth-OD and depth-dose profiles for the 14 different RaLPh configurations. $\mathrm{R}_{80,\mathrm{D}}^{\mathrm{Film}}$ data points have been extracted from depth-dose profiles as illustrated in Figure 2.9. As with the results reported in section 2.3.2.2., the results show that a range calibration factor value of 1.012 ± 0.002 was found by the ratio between the OD and dose measurements at R_{80} value.

Table 2.7 *Comparison of R_{80} value between depth-OD and depth-dose profiles for RaLPh phantom*

Configuration (n)	$R_{80,OD}^{Film}$ (mm)	$R_{80,D}^{Film}$ (mm)	Ratio comparison
SW 1471	102.91	101.78	1.011
SW 1471/SB5	99.30	98.22	1.011
SW 1471/AC	99.49	98.37	1.011
SW 1471/Lung	106.90	105.50	1.013
SW 1471/SB5/Lung	103.10	102.05	1.010
SW 1471/SB5/AC	96.02	94.90	1.012
SW 1471/SB5/Lung/AC	99.70	98.53	1.012
SW 1472	95.64	94.53	1.012
SW 1472/SB5	92.79	91.61	1.013
SW 1472/AC	92.62	91.84	1.009
SW 1472/Lung	100.82	99.09	1.017
SW 1472/SB5/Lung	96.03	94.72	1.014
SW 1472/SB5/AC	88.97	87.93	1.012
SW 1472/SB5/Lung/AC	93.53	92.32	1.013

2.3.3. Validation of EBT3 film results

2.3.3.1. Ionisation measurements in a water phantom

Table 2.8 shows the R_{80} data calculated from the ionisation chamber measurements and calculated $\mathrm{WET_m}$ and $\mathrm{rWET_m}$ for RaLPh materials using equations 2.3 and 2.4.

Table 2.8 *Ionisation R_{80} values, WET_m, and $rWET_m$ for RaLPh materials*

Material	R_{80} (mm)	$\mathrm{WET_m}$ (mm)	$\mathrm{rWET_m}$
Water	98.85		
SB5 (0.5 cm)	90.59	8.27	1.65
AC (0.5 cm)	90.95	7.90	1.58
Lung (0.5 cm)	97.77	1.09	0.21
SW 1471 (0.5 cm)	93.98	4.87	0.97
SW 1472 (0.5 cm)	93.50	5.35	1.07

Table 2.8 continued

SW 1471 (1.0 cm)	89.21	9.64	0.96
SW 1472 (1.0 cm)	88.00	10.85	1.09

2.3.3.2. Empirical determination of solid water scaled depths

$\mathrm{WET_m}$ and $\mathrm{rWET_m}$ for the individual materials (Table 2.8) were used to calculate the R_{80}^{IC} values for the configurations by applying equations 2.10-2.15. These results are shown in Table 2.9 and were compared to EBT3 film measurements ($R_{80,\mathrm{D}}^{\mathrm{Film}}$) shown in Table 2.7. Results from this table show that the agreement between EBT3 film and empirical scaled depths was on average 0.3% for SW 1471 whilst for SW 1472 the agreement was within 1.7%.

Table 2.9 *Comparison of empirical calculations of proton range from the solid water scaled depth with the EBT3 film range measurements $R_{80,D}^{Film}$ (Table 2.7)*

Configuration (n)	$R_{80,\mathrm{D}}^{\mathrm{Film}}$ (mm) (Table 2.5)	R_{80}^{IC} (mm)	% difference
SW 1471	101.78	101.91	0.12
SW 1471/SB5	98.22	98.39	0.17
SW 1471/AC	98.37	98.77	0.41
SW 1471/Lung	105.50	105.79	0.28
SW 1471/SB5/Lung	102.05	102.26	0.20
SW 1471/SB5/AC	94.90	95.24	0.36
SW 1471/SB5/Lung/AC	98.53	99.12	0.60
SW 1472	94.53	92.38	-2.27
SW 1472/SB5	91.61	89.67	-2.11
SW 1472/AC	91.84	90.02	-1.98
SW 1472/Lung	99.09	96.38	-2.73
SW 1472/SB5/Lung	94.72	93.67	-1.11
SW 1472/SB5/AC	87.93	87.30	-0.72
SW 1472/SB5/Lung/AC	92.32	91.30	-1.10

2.3.3.3. Monte Carlo Simulations

The average R_{80} percentage difference between the ionisation chamber measurements and the simulations was 0.01% for the water phantom setup. The point-to-point dose difference between the ionisation chamber measurements and simulated Bragg Peak curves was within 2%. Differences were larger towards the Bragg peak due to the steep dose gradient.

2.3.3.3.1. Beam characterisation

The simulated beam was characterised against the water phantom ionisation chamber measurements and Monte Carlo results was within 2% for dose values up to 10.1 cm. The larger percentage differences in the Bragg peak region between the ionisation chamber and Monte Carlo results are due to the high dose gradient at the Bragg peak but the range is not affected (Figure 2.10). The beam energy was tuned to 114.79 MeV and the energy spread to FWHM=0.9 MeV.

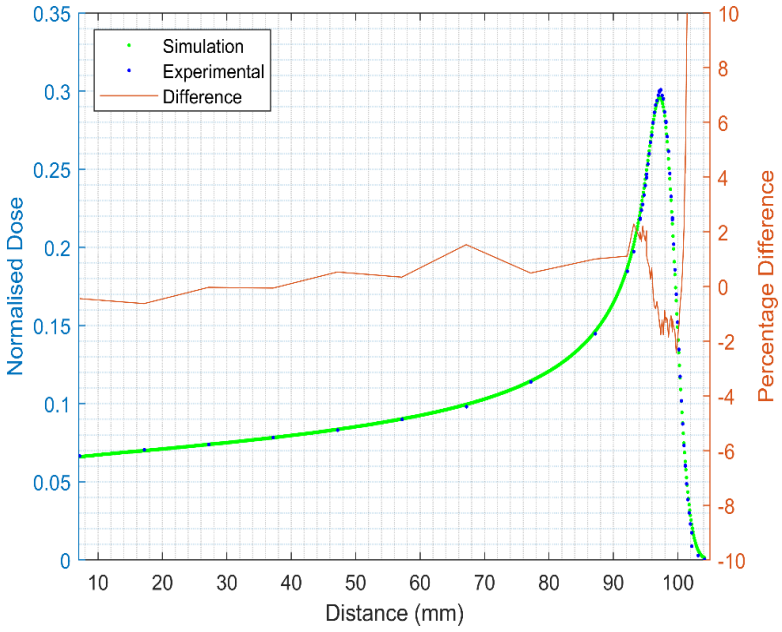

Figure 2.10 *Comparison between ionisation chamber and Monte Carlo simulation data for 115 MeV proton beam in a water phantom*

2.3.3.3.2. Material characterisation

Table 2.10 shows the simulated R_{80}^{MC} ranges and comparison with EBT3 film range dose measurements $(R_{80,\mathrm{D}}^{\mathrm{Film}})$ shown in Table 2.7. The relative standard uncertainty for the repeated simulation range calculations was 0.2% for water depth-dose profiles, 0.4% for SW 1471 configurations and 0.6% for the SW 1472 configurations.

Table 2.10 *Comparison of Monte Carlo simulated ranges with EBT3 film range measurements* $R_{80,D}^{Film}$ *(Table 2.7)*

Configuration (n)	$R_{80,\mathrm{D}}^{\mathrm{Film}}$ (mm) (Table 2.5)	R_{80}^{MC} (mm)	% difference
SW 1471	101.78	101.81	0.03
SW 1471/SB5	98.22	98.26	0.04
SW 1471/AC	98.37	98.64	0.27
SW 1471/Lung	105.50	105.72	0.21
SW 1471/SB5/Lung	102.05	102.17	0.12
SW 1471/SB5/AC	94.90	95.10	0.21
SW 1471/SB5/Lung/AC	98.53	99.00	0.48
SW 1472	94.53	96.18	1.75
SW 1472/SB5	91.61	93.12	1.65
SW 1472/AC	91.84	93.48	1.79
SW 1472/Lung	99.09	100.14	1.06
SW 1472/SB5/Lung	94.72	97.13	2.54
SW 1472/SB5/AC	87.93	90.46	2.88
SW 1472/SB5/Lung/AC	92.32	94.43	2.29

2.3.4. RaLPh in a treatment planning workflow

Table 2.11 shows the TPS predicted R_{80}^{TPS} ranges when considering without and with density override for the phantom materials. The TPS results were then compared to EBT3 film measurements ($R_{80,\mathrm{D}}^{\mathrm{Film}}$) shown in Table 2.7.

Table 2.11 *Comparison of TPS predicted ranged with EBT3 film range measurements* $R_{80,D}^{Film}$ *(Table 2.7)*

Configuration (n)	$R_{80,D}^{Film}$ (mm) (Table 2.5)	No density override		Density override	
		R_{80}^{TPS} (mm)	% difference	R_{80}^{TPS} (mm)	% difference
SW 1471	101.78	106.31	4.45	102.25	0.46
SW 1471/SB5	98.22	103.74	5.62	97.95	-0.27
SW 1471/AC	98.37	103.62	5.34	98.42	0.05
SW 1471/Lung	105.50	112.86	6.98	109.77	4.05
SW 1471/SB5/Lung	102.05	110.62	8.40	103.96	1.87
SW 1471/SB5/AC	94.90	100.62	6.03	96.63	1.82
SW 1471/SB5/Lung/AC	98.53	106.91	8.51	101.48	2.99
SW 1472	94.53	99.80	5.57	95.91	1.46
SW 1472/SB5	91.61	96.93	5.81	92.10	0.53
SW 1472/AC	91.84	98.48	7.23	93.04	1.31
SW 1472/Lung	99.09	106.59	7.57	101.89	2.83
SW 1472/SB5/Lung	94.72	103.66	9.44	98.51	4.00
SW 1472/SB5/AC	87.93	94.51	7.48	90.58	3.01
SW 1472/SB5/Lung/AC	92.32	99.20	7.45	97.77	5.90

2.4. Discussion

This work was completed to address the current lack of phantoms in proton beam therapy that can verify range. RaLPh is a compact, easily transportable phantom which enables quick and easy setup as well as irradiation.

The proton beam tilt study (Table 2.6) showed that no tunnelling effect was seen for zero-degree tilt which has been observed in other film studies [101]. This may be due to the variable slab section in front of the film causing scattering effects before the beam enters the film or the phantom not having significant airgaps between slabs. The average range measured was 101.4 mm and the setup that showed the largest deviation of the averaged range value (0.6%) was the setup with a 10 degrees tilt. For this setup, the film only captures the edge of the field, thus the range seen in the film

is reduced to 100.83 mm. Consequently, this study suggests a small degree tilt may not be required for measurement with the phantom. The gantry (standard deviation (SD) = 0.27 mm) and couch tilt (SD = 0.13 mm) appear to have comparable range measurements, but the gantry shows a slightly larger variation in range measurements. If a small tilt (1-5-degrees) is applied, the couch will provide the most repeatable measurements.

This work also shows the phantom design enables a range of water and tissue-equivalent material configurations to be assessed via measuring range shift with EBT3 film. RaLPh shape and linear interfaces did not perturb the beam and the proton beam travels by direct transmission through the phantom to produce a sharp Bragg peak (Figure 2.9). Consequently, EBT3 film can provide a simple full range measurement which allows for relative comparison of Bragg peaks and R_{80} depths for a range of material configurations.

Varying the phantom plate configurations allow for measurable range differences, as shown in Figure 2.9. The shift of each of the fourteen different configurations was individually determined within a range of 1 cm. These allowed for a range of varying density material configurations to be experimentally tested and compared against TPS calculations. The EBT3 film measurements in this study showed good repeatability and range measurements had an average uncertainty of 0.5% when considering the relative standard uncertainty in positioning of EBT3 film in the phantom and repeatability of measurement. This work agrees with findings from previous studies which showed EBT film was capable of range measurements with a 0.5 mm uncertainty [93,100]. Our findings also suggest the possibility of using a constant

range calibration factor (1.012 ± 0.002) to be applied to the depth-OD measured ranges. Typically, one of the disadvantages of using EBT3 film is that a calibration curve is required to convert OD to dose. The calibration of EBT3 film can be a time-consuming process as it requires additional set up and multiple irradiations over a range of dose values; however, our results suggest a constant range calibration factor can be derived from the ratio of OD and dose values (Table 2.6 and 2.7). Hence the range calibration factor could be applied to future EBT3 film measurements for range measurements to simplify the audit process. However, further work needs to be completed to assess if the same factor can be applied for other proton beam energies.

An extensive investigation into the validation of EBT3 film range measurements was performed. For SW 1471, the EBT3 film ranges agreed within 0.3%, whilst for SW 1472, the agreement was within 1.7% with the empirically determined scaled depths method (Table 2.9). With regards to the Monte Carlo simulation results, the EBT3 film range measurements were also in good agreement (within 0.2%) for SW 1471 (Table 2.10), whilst for SW 1472, deviation were significant larger (1.9%). This is due to the variability in density due to the inhomogeneities of SW 1472 which were not simulated in the Monte Carlo simulations. Although in previous work SW 1472 was found to be superior to SW 1471, and other commercial solid water-equivalent materials, in terms of proton nuclear interaction cross sections [23], homogeneity of the materials is a more important characteristic for range measurements and the results from this study support the use of SW 1471 in future range audit purposes. Overall, the validation results showed that EBT3 film can be used within a heterogeneous phantom for accurate range measurements.

In the second stage, the phantom was assessed for independent range verification capability in the clinic as part of a dosimetry audit for proton beam therapy. Table 2.11 shows there was a large discrepancy between the measured EBT3 film ranges and the TPS predictions when the latter automatically assigned densities to the various materials within the phantom based on the CT calibration curve. This was due to the materials in RaLPh not being tissue-equivalent in terms of photon interactions resulting in their stopping power to be wrongly derived from the stoichiometric calibration curve [120]. Some uncertainty could also be attributed to the ability to accurately distinguish each sample per voxel in the CT scan as some samples were relatively thin (5 mm thick) compared to the scan resolution of 1 mm per slice. Thicker slabs could reduce CT imaging uncertainty, though it should be noted that regions of thin tissue and bone can be found within the body. Nevertheless, some of this range discrepancy can be traced to the uncertainty in the TPS proton beam transport algorithm as well. When the density of the material was manually overridden (density override changes the Hounsfield unit of the material, which in turn changes the RSP in Pinnacle) in the TPS the discrepancy decreased to less than 1% if lung configurations are not considered. The lung-equivalent material used is very spongy in nature so there is a larger uncertainty on the measured density of this material.

Results from this study suggest that the RaLPh phantom could be used as a range audit device, if the correct material override values were provided to centres for their TPS system. This corresponds to a known issue and, for example, IROC applies a material override to some of the materials used in their Radiological Physics Centre (RPC) phantoms, due to some of the phantom materials having a relative linear stopping power (RLSP) greater than 5% from the TPS predicted values [78].

Consequently, the phantom cannot be used to validate the CT calibration curve as part of an audit. For a full treatment workflow audit, work needs to be undertaken into the development of materials that are tissue-equivalent in both photon and proton beams. In Chapter 3, I will discuss work undertaken to develop new tissue materials that are optimised for photon and proton therapy beams for a range of properties that will include attenuation, stopping power, range, scattering and nuclear interactions [121] . Materials developed during this section of work could be applied to the RaLPh as this will facilitate the TPS to correctly assign accurate RLSP. The full treatment workflow audit would provide a more comprehensive testing of the TPS system, including the CT calibration process. In future work, quenching corrections could also be applied to EBT3 film to achieve reference dose measurements [76,100] as well as investigation into possible batch or energy dependent corrections of EBT3 film with regards to the range calibration factor.

2.5. Conclusion

The RaLPh phantom is compact, of simple setup and provides good repeatable range measurements with EBT3 film. EBT3 film can provide repeatable simple depth dose measurements with an average relative uncertainty of 0.5% at the R_{80} depth. A 1.012 range calibration factor from optical density to dose R_{80} values could be applied for proton range measurements. EBT3 film measurements have been validated via Monte Carlo simulations and an empirically determined scaled depths method using ionisation chamber measurements. The phantom can be used as an audit device provided density override for the materials is used in the TPS. For the phantom to be

implemented as a full treatment workflow audit device, future work needs to improve the elemental formulation of the tissue-equivalent materials.

This work has shown EBT3 film to be an accurate range detector for scanning proton beam depth dose measurements within a heterogeneous phantom and that RaLPh can serve as a range audit device that can complement reference dosimetry audits and end-to-end test based dosimetric audits.

2. Investigation of proton optimised tissue-equivalent materials

The work presented in this chapter has been submitted to IOP Physics in Medicine and Biology:

Cook H., Simard M., Niemann N., Gillies C., Osborne M., Hussein M., Rompokos V., Bouchard H., Royle G., Pettingell J., Palmans H., Royle G., Pettingell J., & Lourenço A. Development of optimised tissue-equivalent materials for proton therapy. Physics in Medicine & Biology **68,** 075009, (2023)

It has also been presented at the following conferences via oral and poster format:

Cook H., Royle G., Palmans H., & Lourenço A. Simulations for the improvement of bone-equivalent materials for proton beam dosimetry. International Conference on Monte Carlo Techniques for Medical Applications 2019; *Montreal, C.A.(Oral presentation)*

Cook H., Royle G., Palmans H., & Lourenço A. Development of a bone-equivalent material for the dosimetry of proton therapy beams. *58th Annual Conference of the Particle Therapy Co-Operative Group 2019*; Manchester, U.K. *(Poster presentation)*

Cook, H., Simard M., Niemann N., Gillies C., Palmans H., Hussein M., Bouchard H., Royle G., & Lourenço A. Optimising tissue-equivalent materials for proton therapy. European Society for Therapeutic Radiology and Oncology Conference 2022; *Copenhagen, D.K. (Oral presentation)*

My contributions to these publication and conference proceedings were as follows; adaptation of semi-analytical model for tissue-equivalent materials as well as development of the mathematical model to produce proton optimised tissue-equivalent materials were conducted by me. The implementation of the cost-function approach mathematical model within MATLAB was performed by me with the assistance of Dr. Mikaël Simard. The formulation of new proton optimised tissue-equivalent materials (bone and muscle) was performed by me. Manufacture of the bone and muscle-equivalent materials was in collaboration with BARTS NHS Trust. Proton experiments and CT scanning performed at Rutherford Cancer Centres (North-East and Thames Valley), university College London Hospital (UCLH) Proton Centre and NPL were performed by me with the assistance of NPL staff as well as staff at the clinical facilities. Dual CT analysis was calculated by Dr. Mikaël Simard under my guidance. Analysis and interpretation of the results and Monte Carlo simulations were performed by myself under guidance of my supervisors and NPL staff; the paper was written by me and proof-read by the co-authors.

3.1 Introduction

Tissue-equivalent phantoms are a vital tool for plan and dosimetric verification in end-to-end radiotherapy audits [20,36,37,68,72]. Over the past 50 years, a variety of phantoms have been developed for radiation modalities such as X-ray and electron treatments [78]. However, due to differences in radiation interaction with matter between photon and proton beams [12,122], phantom materials previously used for X-ray phantoms [52] are not optimised, or sometimes unsuitable, for proton therapy.

Existing phantom materials have been developed to mimic electron density and Hounsfield Unit (HU) for imaging and X-ray treatments [52]. However, for proton

therapy, HU, and proton interactions such as RSP should be mimicked as closely as possible for suitable phantom materials. Uncertainties caused by phantom materials have been highlighted by Farr *et al.* (2021) [99] for the commissioning of intensity-modulated proton therapy systems. In addition, the IAEA TRS-398 report [21] states that solid phantom materials should not be used for reference dosimetry due to the lack of information regarding water to plastic fluence corrections. Proton phantom development work by the IROC group [72,73,78,123] emphasises the importance of appropriate selection of suitable phantom materials to ensure the phantom can be used for proton dosimetry measurements. In particular, bone materials were shown to result in large uncertainties which could produce up to 35% error in proton range [73]. Consequently, there is a need for phantom materials that have been optimised specifically for proton therapy interactions.

A range of approaches have been used for the development of tissue-equivalent materials in radiotherapy. The elemental equivalence method attempts to formulate a mixture with the same elemental composition of the target tissue, however, this was shown to be challenging for complex compositions [55,124,125]. The effective atomic number [126,127] was also proposed to characterise materials for photon beams. Typically, Compton scatter is considered as it is the dominant interaction for clinical photon beams. However, this method is limited as it only characterises the material for a specific energy. Therefore, more complex methods were proposed by White (1974), e.g. the basic data and extended $\bar{Y}(x)$ methods [52]. These methods were then used to formulate phantom materials for photons in the energy range from 10 keV to 100 MeV and low energy electrons, with the goal of tailoring the tissue-equivalent materials to mimic selected radiation properties within 1% of the target

material. Many tissue-equivalent materials used today are still based on the work of White *et al.* (1974) [52,91]. Their work was then furthered by Constantinou (1978) [52,56,128–130], who developed solid and gel-based tissue-equivalent materials for particle therapy (neutrons and protons). For proton therapy dedicated substitute materials, only mass density and mass stopping power were used within their model [56]. The new formulations were tested in a collimated scattered proton beam and the proton range as well as lateral profiles of the formulated materials compared to real tissue samples.

Water-equivalent materials for proton dosimetry were explored by Lourenço *et al.* (2017) [90] who assessed the particle fluence in commercial plastics against new plastic formulations. Their work highlighted a possible avenue of improvement of current tissue-equivalent materials for proton therapy by formulating new water-equivalent plastics which matched water within 1% for low- and high-energy proton beams in terms of particle fluence. As presented in Chapter 2, these materials were implemented in the proton range phantom (RaLPh) and results showed the materials are not tissue-equivalent for range calculations within clinical TPS [131]. Consequently, for the development of tissue-equivalent materials, suitable for end-to-end audit purposes, a variety of radiation properties need to be accurately matched to the specific human tissues.

In this work, a semi-analytical model was adapted, and a cost-function approach model developed that formulates epoxy-resin-based tissue-equivalent materials. For this study, the focus was the development of phantom materials to be used in end-to-end audit phantoms to mimic the patient workflow from patient data acquisition, treatment planning to dose delivery and perform overall dose verification for this entire

workflow. Consequently, the phantom materials needed to be tissue-equivalent for both imaging photon energies as well as therapeutic proton energies to ensure the materials are correctly characterised and provide accurate dosimetry of the target tissues. To our knowledge, this is the first cost-function approach model that enables the formulation of water and tissue-equivalent materials which considers not only photon interactions but also proton stopping power, nuclear absorption, and scattering interactions. The tissue-equivalence of the optimised materials were also compared against alternative commercial tissue-equivalent materials to evaluate their performance. A short study was performed to assess commercial bone-equivalent materials against real bone samples (Appendix, section C). Through the use of the cost-function model, new epoxy-resin based vertebra bone and muscle materials were made at the Barts Health NHS Trust using the manufacture process developed by White (1974) [128]. These manufactured materials were characterised by experimental testing and Monte Carlo simulations to assess their suitability for clinical use.

3.2 Methods

3.2.1. Epoxy-resin-based manufacture

In this study, the tissue-equivalent materials developed were based on epoxy-resin base mixtures (Figure 3.1). This technique was previously used by White (1974) and Constantinou (1978) [52,56,128–130]. This method is still used by Barts Health NHS Trust for the manufacture of many water- and tissue-equivalent plastics used in clinical photon and electron beams.

a) b) c)

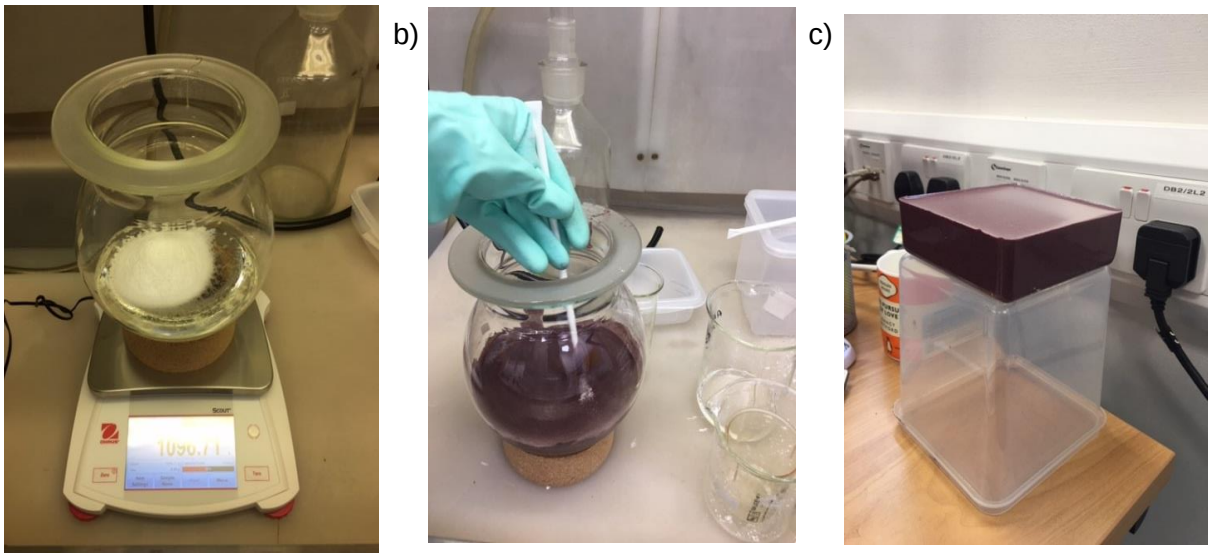

Figure 3.1 *Epoxy resin manufacture trial at the NPL. a) Weighing of resin, hardener and power into mixing vessel, b) Stirring of mixture until homogenous, c) Final cured block of water-equivalent plastic*

In summary, for the development of tissue-substitute materials, an epoxy resin, hardener, and selected powders or liquids are mixed to achieve a formulation with the required radiation properties of a desired target tissue. For successful hardening of the tissue-equivalent material, a specific mix ratio of epoxy resin and hardener is required; the different epoxy resin and hardener ratios were defined by White (1974) [52] and were given the names CB1, CB2, CB3, and CB4. In this work, CB4 was used as this combination has been thoroughly tested and can be used to produce larger cast volumes required for phantom development. Typically, the mass density of epoxy resins are greater than that of soft issue [132], hence low density microspheres, such as phenolic microspheres, are typically added to the mixture to achieve the required mass density of the material without significant change to the elemental formulation [129]. The mixture is vacuumed during and/or after mixing to remove any possible air bubbles and left to cure over a few days.

3.2.2. Formulation models for tissue-equivalent materials

During this project, two models were used for developing proton optimised tissue-equivalent materials: i) a semi-analytical model and ii) a cost-function approach

To create a material, CB4 was theoretically mixed with phenolic microspheres, and *N* additional compounds. The elemental mass ratios in which the epoxy, phenolic microspheres, and components were mixed dictate the final radiation properties of the mixture. The aim of the model was to find which material ratios produce adequate target tissue mimicking properties for photon imaging beams as well as therapeutic proton beams.

3.2.2.1. Semi-analytical model

The semi-analytical model was based upon the work of Palmans *et al*., (2002) [88], Al-Sulaiti *et al.,* (2012) [89], and Lourenço *et al.,* (2017) [90] . The model was modified to include a series of equations which analytical describe both photon and protons interaction properties. For example, the model implemented equations such as the Bethe stopping power equation [12], Gottschalk's scattering length equation [133], and Palmans *et al*., (2002) analytical approach for determination of fluence correction factors of materials [88].

The model was used to try to determine an optimised high density bone material formulation. High density bone was chosen as it is one of the most difficult tissues to replicate due to its density and composition. Secondly, due to it being a dry tissue material it would be simpler to produce a real bone sample for comparison within the experimental set up. ICRP cortical bone formulation was selected as the target tissue [48]. This work attempted to formulate a bone-equivalent material via a manual iterative approach by changing the mixture elemental composition based on a small

library of powders, and subsequently calculating its radiation properties in comparison to the target tissue.

3.2.2.2. Cost-function model

The formulation of tissue-equivalent materials by manual iterations with the semi-analytical model was found to be slow and inefficient. Thus, a more effective mathematical approach was developed to optimise new formulations via a cost function model based on the semi-analytical descriptions of photon and proton interaction properties. A cost function was implemented due to the inability to mimic all radiation properties without the use of human tissues. The cost function was designed to quantify the similarity between a mixture and a target material and empirically weighted the radiation properties on the relative importance of each quantity. Further details on the cost function can be found in section 3.2.4.3.

The cost-function model focussed on the formulation of skeletal muscle and vertebra bone materials for the development of a head and neck phantom. The tissues were based on Woodard and White and ICRP reference tissue data [47,48]. A library of epoxy, resin and powders elemental compositions were collated from previous tissue-equivalent material research [52,56]. The model used the elemental composition libraries and a constrained nonlinear least squares algorithm to find the formulation which provides the local minimum cost function value. The model was constrained to reduce the complexity of the possible mixtures in addition to tailoring the formulations to the manufacturer limitations, e.g., minimum epoxy and hardener requirements of 40% in the formulation. The formulation with the lowest cost function amongst the *N* solutions was chose as the optimal formulation.

The summary radiation properties implemented in the two models are defined in table 3.1 and the details of the equations discussed in sections 3.2.3.1-7.

3.2.3. Radiation properties used in models

Table 3.1 highlights which physical and radiation properties were calculated with each model. For the semi-analytical model, mass density was not considered as it was assumed the material density could be adjusted via the use of phenolic microspheres. For radiation properties which required density, for radiation properties such as HU, the target tissue density was used. For the cost-function model, a density estimation calculation was implemented into the model.

Table 3.1 *Material properties and radiation parameters considered in models (semi-analytical model and cost-function model).*

Material property/ Radiation parameter	Semi-analytical model	Cost-function model
Mass density		X
Mass attenuation coefficient	X	X
Hounsfield Unit	X	X
Mass stopping power	X	
Relative stopping power		X
Range	X	
Nuclear interactions: nuclear reaction cross-section and linear energy transfer	X	X
Nuclear interactions: fluence correction factor	X	
Scattering Length	X	X

3.2.3.1. Mass density

The mass density of the material, ρ_m, needs to be mimicked to ensure that beam characteristics such as photon attenuation and proton range are the same as the target tissue. The conservation of volumes for material mixtures was assumed, which implies that no air is added into the mixture, that solid powders dissolve into the liquid

without reducing the total volume and that chemical reactions also do not alter the volume. This results in the following formulation for the material's mass density:

$$\rho_m = \left(\sum_{l=1}^{L} \frac{w_i}{\rho_i} \right)^{-1} \tag{3.1}$$

The index l represents one of the L mixture materials, and $w_i,\ \rho_i$ are respectively the mass fractional weight and mass density of the material constituents (i) of the mixture.

3.2.3.2. Mass attenuation coefficient

For photon interactions, the photon mass attenuation coefficient of the material, $\left(\frac{\mu}{\rho}\right)_m$, is the main beam interaction that needs to be considered for CT imaging [12]. For mixtures, it is obtained as:

$$\left(\frac{\mu}{\rho}\right)_m = \int \psi(E) \sum_{l=1}^{L} w_i \left(\frac{\mu(E)}{\rho}\right)_i \mathrm{d}E \tag{3.2}$$

where $\left(\frac{\mu(E)}{\rho}\right)_i$ is the energy-dependent mass attenuation coefficient of the i^{th} material in the mixture, and $\psi(E)$ represents the normalised spectrum of the polyenergetic X-ray source used for imaging. A 100 kVp clinical spectrum was used in the model.

3.2.3.3. Hounsfield unit

The HU is an important value to consider to calculate the respective RSP of the material via the stoichiometric calibration curve [120]. Multiplying $\left(\frac{\mu}{\rho}\right)_m$ by the density

provides the linear attenuation coefficient of the material, μ_m, which can be used to calculate the HU of the material:

$$\mathrm{HU}_m = 1000 \times \frac{\mu_m - \mu_w}{\mu_w} \tag{3.3}$$

where μ_w is the linear attenuation coefficient of water. For the semi-analytical model, HU was determined via the stoichiometric calibration method developed by Schneider *et al.,* (1996) [120], using data from the NPL Mediso AnyScan SCP scanner at 120 kVp. A linear regression fit of the CIRS electron density phantom HU values were used to determine parametrization of interaction cross-sections constants (photoelectric effect (K^{ph}), coherent scattering (K^{coh}), Klein-Nishina (K^{KN})). The derived interaction constants were reapplied to determine the total attenuation, and in turn the theoretical HU (Equation 3.3) for human tissues and plastic materials from the elemental composition data.

3.2.3.4. Mass stopping power and relative stopping power

The predominant way that a proton beam loses energy through a material is via inelastic interactions with electrons, which is described by the electronic stopping power. For the semi-analytical model, the mass electronic stopping power was calculated due to research focusing on density independent calculations $\left(\frac{S_{\mathrm{el}}}{\rho}\right)_m$, whereas for the cost-function model, the linear electronic stopping power, $(S_{\mathrm{el}})_m$, was considered. The electronic stopping power is calculated via the Bethe equation assuming that other terms in the stopping power expression do not play a significant role in the clinical proton energy range.

$$(S_{el})_m = \frac{\rho_m 4\pi r_e^2 m_e c^2}{u} \frac{1}{\beta^2} \left(\frac{Z}{A}\right)_m \left[\ln\left(\frac{2mc^2\beta^2}{(1-\beta^2)I_m}\right) - \beta^2\right] \quad (3.4)$$

where r_e is the electron radius, m_e is the electron rest mass, c the speed of light, u is the atomic mass unit, β is the proton velocity in units of the velocity of light. $\left(\frac{Z}{A}\right)_m$ of the material was calculated using the rule of mixtures, where Z and A respectively represent the atomic number and atomic mass of the mixture. I_m is the mean excitation energy of the mixture in the condensed phase calculated using the Bragg additivity rule [12]:

$$\ln(I_m) = \frac{\sum_{i=1}^{I} w_i \left(\frac{Z}{A}\right)_i \ln(I_i)}{\left(\frac{Z}{A}\right)_m} \quad (3.5)$$

For the cost-function model, the electronic stopping power was determined over the energy range 50 to 250 MeV in energy steps of 1 MeV and then averaged. The average RSP of the mixed material, RSP_m, is calculated as the ratio of the electronic stopping power of the material to that of water:

$$RSP_m = \frac{(S_{el})_m}{(S_{el})_w} \quad (3.6)$$

3.2.3.5. Range

The range was calculated using the following equation [134]:

$$r_o = \rho \int_{T_f}^{T_0} [S_{el}(E)]^{-1} dE \quad (3.7)$$

The continuous-slowing-down approximation (CSDA) range of a particle slowing down from an initial energy E_0 to a final energy E_f was calculated from the integration

of the reciprocal of the electronic stopping power over the final and initial energy values. In this work, the initial energy was set to be 200 MeV. Range straggling was not accounted for in this work.

3.2.3.6. Nuclear interactions

Another significant way that energy is removed from a proton beam is via nuclear interactions. Non-elastic nuclear interactions result in a difference in fluence when comparing different materials at equivalent depths. Therefore, fluence correction factors are important when comparing dose between materials [135].

Firstly, the nuclear reaction cross-section was calculated as it represents the probability of a primary proton being removed from the beam by a nuclear interaction. The linear energy transferred to secondary protons and alpha particles was also calculated at low and high proton beam energies ($E_1 = 50$ and $E_2 = 200$ MeV). Secondary proton and alpha particles were chosen due to their significant contribution to dose [136]. It should be noted that nuclear cross sectional data was limited to carbon, nitrogen, oxygen, aluminium, silicon, phosphorus, calcium, iron, copper, tungsten, and lead [137]. Therefore, the elemental composition was scaled to consider the possible small discrepancy due to unavailable cross-sectional data.

The nuclear reaction cross section of the mixture at energy E_p per atomic mass $\left(\frac{\sigma_{\mathrm{nucl}}(E_p)}{A}\right)_m$, in units of cm^2g^{-1}, was calculated with the rule of mixtures [12]:

$$\left(\frac{\sigma_{\mathrm{nucl}}(E_p)}{A}\right)_m = \sum_{l=1}^{L} w_i \left(\frac{\sigma_{\mathrm{nucl}}(E_p)}{A}\right)_i \tag{3.8}$$

The linear energy transferred from a proton of energy E_p to a secondary particle k, where k is a proton or an alpha particle, is defined as $\left(\frac{\sigma_{\mathrm{tr},k}(E_p)}{A}\right)_m$ with units of MeVcm^{2}g^{-1}, and is calculated using:

$$\left(\frac{\sigma_{\mathrm{tr},k}(E_p)}{A}\right)_m = \sum_{l=1}^{L} w_i \left(\frac{\sigma_{\mathrm{tr},k}(E_p)}{A}\right)_i \bar{W}_k(E_p) \tag{3.9}$$

where $\bar{W}_k(E_p)$ is the average emission energy of the recoil spectrum.

The sum of the nuclear interactions cross section values was calculated via Equation 3.10. This is not a physical quantity but deemed as an appropriate quantity for the cost function.

$$\left(\frac{\bar{\sigma}_{\mathrm{nucl}}}{A}\right)_m = \sum_{E_p=50,200\ \mathrm{MeV}} \left[\left(\frac{\sigma_{\mathrm{nucl}}(E_p)}{A}\right)_m + \left(\frac{\sigma_{\mathrm{tr,proton}}(E_p)}{A}\right)_m + \left(\frac{\sigma_{\mathrm{tr,alpha}}(E_p)}{A}\right)_m\right] \tag{3.10}$$

For the semi-analytical model, the nuclear reaction cross-section and linear energy transferred to secondary protons, alpha particles, deuterons, tritons and ^{3}He and recoils were used to directly determine the fluence correction factor (k_{fl}^{AM}) of the material [135]. The fluence correction factor was calculated at high proton beam energy (E_2 =200 MeV).

The following simplifications are used [135];

- Secondary particles considered are protons, alphas, deuterons, tritons, ^{3}He and recoils.
- The energy given to any secondary charged particles from a nuclear interaction is deposited at the place of the interaction.
- The energy transferred to neutrons and gamma rays aren't included.

Dose $D_m(z_m)$ to medium was calculated as:

$$D_m(z_m) = \Phi_m^{\mathrm{P_{Prim}}}(z_m).\left(\frac{S_{el}(E_p)}{\rho}\right)_m + \Phi_m^{\mathrm{P_{Prim}}}(z_m) \cdot N_A \cdot \sum_k \sum_i w_i \left(\frac{\sigma_{\mathrm{tr},k}(E_p)}{A}\right)_i \bar{W}_k(E_p) \quad (3.11)$$

where $\Phi^{P_{\mathrm{prim}}}$ is the primary proton fluence, calculated from the nuclear reaction cross sections, $\left(\frac{S_{\mathrm{col}}(E_p)}{\rho}\right)_m$ is the mass stopping power of the material, and N_A is Avogadro's constant. The first term can be described as the energy loss of primary protons while the second term describes the energy loss due to nuclear interactions. $k_{\mathrm{fl}}^{\mathrm{AM}}$ is computed as:

$$k_{\mathrm{fl}}^{\mathrm{AM}} = \frac{D_{(Z_{t-eq})}}{D_m(z_m) \cdot \left(\frac{S_{\mathrm{el}}(Ep)}{\rho}\right)_t \Big/ \left(\frac{S_{\mathrm{el}}(Ep)}{\rho}\right)_m} \quad (3.12)$$

where $D_{(Z_{t-eq})}$ is the dose in the tissue at an equivalent thickness, $D_m(z_m)$ is the dose in the plastic material, $\left(\frac{S_{\mathrm{el}}(E_p)}{\rho}\right)_t$ is the mass electronic stopping power for tissue and $\left(\frac{S_{el}(E_p)}{\rho}\right)_m$ is the mass electronic stopping power for the equivalent material. If $k_{\mathrm{fl}}^{\mathrm{AM}}$=1, the target tissue and plastic material are regarded equivalent in terms of particle fluence.

3.2.3.7. Scattering Length

Besides energy loss, directional spread should also be considered to achieve the same dose distribution as in tissue. The scattering length of a material, $X_{s,m}$, can be related to scattering power and can be interpreted as the distance a 15 MeV proton would have to travel in a medium for the scattering angle to increase by 1 rad. Generally, the scattering length $X_{s,i}$ is a material property defined as:

$$\frac{1}{\rho X_{s,i}} = \alpha\, N_A\, r_e^2 \left(\frac{Z^2}{A}\right)_i \left(2\log\left(33219(AZ)^{-\frac{1}{3}}\right) - 1\right) \tag{3.13}$$

where α is the fine structure constant. This equation comes from the simplification of the scattering power devised by Rossi (1952) [138] when considering the scattering for clinical proton beam energies.

The scattering length of mixtures is obtained with equation 3.14.

$$\left(\frac{1}{\rho X_s}\right)_m = \sum_{l=1}^{L} w_i \left(\frac{1}{\rho X_s}\right)_i \tag{3.14}$$

3.2.4. Implementation of the models

The main challenge of this work was the ability to formulate materials that could be successfully mixed, poured, and result in a cured homogeneous material. Although the models provided a fast method for the formulation of theoretical proton optimised tissue-equivalent materials; the manufacture process remained a trial-and-error method and multiple materials were developed during this study. This was mainly due to the selected component powders not being fine enough to ensure homogenous mixing into the CB4 mixture; crystalline powders were shown to sink during the curing process. Therefore, the component library was adapted through the project and the manufacture process limitations were tailored into the constraints of the cost-function model to reduce the trial-and-error approach.

3.2.4.1. Semi-analytical model

To create a material, I theoretically mixed CB4 and 1-2 additional compounds. 3 powders were considered: calcium carbonate, tricalcium phosphate, and hydroxyapatite due to their calcium-based formulations. The model was used to

formulate one cortical bone (DB#1) formulation based on ICRP cortical bone [48]. Photon and proton interactions were also calculated for current commercial tissue-equivalent materials [91,139] that mimic selected target tissues, e.g. for cortical bone (1.85 g/cm^3), commercial bone-equivalent plastic materials with similar density (1.83-1.91 g/cm^3) [91,104] were considered, CIRS Cortical bone and Dense Bone (1250 mg/cc), Gammex Cortical Bone (SB3) and Hard Bone (SB5) [91,140,141]. Delrin (1.43 g/cm^3) was considered due its accessibility to purchase and use in phantoms as a bone-equivalent material such as the Catphan-CT404 phantom [142]. Two 3D printable bone materials were also considered; NPL bone (1.32 g/cm^3) which has been developed to enable the manufacture of a 3D printable pelvis phantom to test gamma ray detection probes for intra-operative cancer detection [143] as well as Accura Bluestone which is typically used to print high stiffness parts such as for wind tunnels [104].

3.2.4.2. Cost-function model

To create a material, I theoretically mixed CB4 with phenolic microspheres and 1 or 2 additional compounds. A list of 89 components was created based on the work of White (1974) and Constantinou (1978) [52,56]. The selected components were affordable (<£2 per gram), non-hazardous, and powders or liquids.

The model was used to formulate a vertebra bone (where two samples were formulated, VB#1 and VB#2) based on ICRP skeleton vertebra bone excluding cartilage formulation [48]. A skeletal muscle-equivalent material (where seven samples formulated, MS#1, MS#2, MS#3, MS#3 v2, MS#4, MS#5, and MS#6) based on Woodard and White's Skeletal Muscle 2 formulation [47]. Photon and proton interactions were also calculated for current commercial tissue-equivalent materials

[91,139] that mimic selected target tissues, e.g. for bone, commercial bone-equivalent materials with similar density (ρ= 1.34-1.56 g/cm^3) were selected, these were CIRS Bone (600 mg/cc), Gammex Bone #480 and #484 and Leeds Test Object (Average Bone) [91,140,141]. The commercial muscle materials assessed were CIRS muscle and Gammex Muscle [140,141]. The elemental compositional of all commercial materials assessed in this work can be found in the Appendices, section B.

3.2.4.3. Cost function

Accurately matching a target material's properties as well as photon and proton interactions with a mixture of I components is impossible without the use of real human tissues. For the cost-function model, a cost function was designed to quantify the similarity between a mixture and a target material. The cost function was applied to weight the sum of the square of relative differences between $Q = 6$ properties of the target and mixture material. The 6 quantities (noted later with index q) are the mass density ρ_m (equation 3.1), mass attenuation coefficient $\left(\frac{\mu}{\rho}\right)_m$ (equation 3.2), HU$_m$ (equation 3.3), relative stopping power RSP_m (equation 3.6), scattering length $X_{s,m}$ (equation 3.14) and one defined as $\left(\frac{\bar{\sigma}_{\mathrm{nucl}}}{A}\right)_m$, which is the sum of the nuclear interactions cross sections reported in section 2.2.5.

Ultimately, all 6 quantities depend upon the mass fractional weights w_i of the I components of the mixture, which is the optimization variable. The cost function is defined as:

$$\mathrm{C}(w_i) = \sum_{q=1}^{Q} \delta_q \Delta_q^2 \qquad (3.15)$$

where $\Delta_q$is the relative difference on the q^{th} quantity between target material and the proposed mixture, and δ_q is an empirically defined weight that empirically sets the relative importance of each quantity. Table 3.2 shows the material formulation input settings and cost function weightings (δ_q) for each quantity (q) considered in the model for each mixture. Mass density, mass attenuation, and RSP were assigned higher weights due to their impact on the materials ability to be correctly characterised during imaging and on the TPS as well as providing accurate proton dosimetry measurements.

The optimisation of the new formulation was achieved using the $fmincon$ function [144,145] in Matlab R2020b (MathWorks, Natick, MA, U.S.A.). This function finds a local minimum of a cost function using a constrained nonlinear least squares algorithm.

The function was constrained by a set of conditions mainly linked to the manufacturing process for epoxy resin-based materials:

- A minimum of $w_i = 30$ or 60% of CB4 was set as the lower limit for the epoxy resin in the model dependent on either bone or muscle was being formulated. This ensures that the components would be easily mixable and pourable in the manufacturing stage. A maximum of $w_i =$ 80-85% of CB4 was also implemented to try and improve homogenous mixing of small amounts of powder for muscle formulations.
- The number of mixture components was set to N = 1 or 2 components to reduce the complexity of the manufacture process. Phenolic microspheres were always considered in the mixture formulation to ensure easily matching the density of the targeted material. Overall, this results in I = 3 parameters to

optimise (mass fractional weight of CB4, mass fractional weight of phenolic microspheres and one or two components).

A starting point formulation was implemented into the optimising function. It was defined as a formulation containing 1.1 times the minimum percentage constraint of epoxy resin amount, while the remaining percentage of the formulation was equally divided between the number of components (N) defined in the model iteration. It should be noted the model's defined cost function is not necessarily a convex function and so the global minimum may not be found within the function. The solution with the lowest cost function was used as the optimal material for this work as the best approximation of the global minimum of the function among the N solutions.

Table 3.2 presents the material input information, constraints, and cost function weightings and used for the formulation of the vertebra bone and skeletal muscle formulations. For VB#1-2 and MS#1, the HU was determined after the optimisation, while for MS#2, MS#3 and MS#4, a weighting value was used for HU in the cost function, as earlier stage tissue formulation research highlighted the importance of matching this quantity. Also, after the manufacture of MS#3, the formulation was adjusted by the addition of less than 1% of phenolic microspheres to alter the density to better mimic the target tissue density, this formulation was named MS#3 v2. During this project, the development of a homogenous muscle material which could be accurately characterised by CT scans was found to be particularly challenging. For MS#5 and MS#6, the optimisation was focused on a small component library of powders known to be able to successfully mix with CB4 to produce a more homogenous mixture. The cost function weightings were adjusted as optimising all radiation parameters with a small library was shown to formulate a material with

generally large uncertainties of 5-10% differences for proton interactions compared to the target tissue. For this, only density and mass attenuation weightings were applied due to their importance for characterisation of the material as well as the density's impact on both photon and proton interactions. The other proton interaction properties were then assessed after the optimisation to ensure the radiation parameters were within an acceptable uncertainty.

Table 3.2 *Description of material formulation input settings and cost function weighting, δ_q, used for each formulation. For VB#1, MS#5, and MS#6 the compound library was limited to only components used in current manufacture of photon tissue-equivalent materials at Barts Health NHS Trust or had been shown to mix well with CB4 during the study. For the other iterations, VB#2, MS#1-#3 the full component library was considered minus the powder previously used in earlier formulations. For MS#4, the compound library was simplified to only components defined as powders. *A 2% correction to the density calculation was also applied to the model due to results from previous sample iterations showing an underestimation of density calculations to compared to experimental values.*

Material formulation	Varied Material formulation input				Cost function weightings					
	Component Library (N)	Component properties	I parameter	% of CB4 (min and max)	Density	Spectrum weighted mass attenuation	Relative Stopping Power	Scattering Length	Average Nuclear interaction	HU
VB#1	3	Fine powders	3	30 and 100	0.21	0.26	0.26	0.13	0.13	0
VB#2	89	Liquid and Powders	3	30 and 100	0.21	0.26	0.26	0.13	0.13	0
MS#1	89	Liquid and Powders	3	60 and 100	0.21	0.26	0.26	0.13	0.13	0
MS#2	88	Liquid and Powder	3	60 and 100	0.17	0.22	0.22	0.11	0.11	0.17
MS#3	87	Liquid and Powders	3	60 and 100	0.17	0.22	0.22	0.11	0.11	0.17
MS#4	49	Powders	3	60 and 80	0.17	0.22	0.22	0.11	0.11	0.17
MS#5*	3	Fine powders	4	60 and 85	0.5	0.5	0	0	0	0
MS#6*	4	Fine powders	4	60 and 85	0.5	0.5	0	0	0	0

3.2.5. Monte Carlo validation of the mixtures

Monte Carlo simulations were performed for the further validation of the theoretical radiation properties of the materials calculated via the semi-analytical and cost-function model. The Monte Carlo method was used to simulate transport of a high-energy mono-energetic proton beam travelling through a given thickness of human tissue and tissue-equivalent materials. The Monte Carlo simulation parameters are summarised in Table 3.3. For newly formulated materials, the cost-function model derived densities were used. The model derived density values were used as any manufactured formulations with densities greater than the target density were corrected via the use of phenolic microspheres to match the density without significantly affecting the elemental formulation.

Table 3.3: *Monte Carlo parameter for the tissue-equivalence of materials simulation*

Item name	Description	References
Title	Tissue-equivalence of materials	
Code and version	FLUKA 2011.2x.2/.4 and FLUKA 2021.2.1 and Flair 2.3.0	[24,117,118]
Geometry	Cylinder target =26 cm in length and radius of 30 cm. The geometry was surrounded by vacuum.	
Materials	The materials composition, density, and I-values were defined for each material. Composition of commercial materials found in Appendices, section B. I-values were theoretically calculated (Equation 3.5).	
Source	Proton pencil beam. Energy = 200 MeV, energy spread = 0, momentum shape = gaussian, divergence = 0, beam shape (X and Y) = rectangular	
Physics and Transport parameters	Default hadrotherapy (HADROTHErapy card) physics. Full heavy ion transport (IONTRANS set to “full transport”). Coalscence mechanism (COALscence) was activated. New evaporate model with heavy fragment transport (EVAPORAT se to “New Evap with heavy frag” option) activated. Ion spit (IONSPLIT) activated with minimum and maximum energy defined as 5 MeV and 115 MeV, respectively. Secondary electrons set to deposit locally with EMFCUT (transport and prod-cut). The energy transport (PART-THR) cut-off energies for proton and heavier particles were set to 100 keV.	
Scoring	Dose (URSBIN card), R–Φ–Z (no symmetry), length of scoring = 26 cm radius of scoring = 10 cm, number of R bins = 1, number of Φ = 1 and number of Z bins = 1301. Dose was simulated for primary protons, secondary protons, alpha, He^3, deuterons and tritons. Fluence (URSTRACK), linear binning, energy scoring (min-max) = 0-200 MeV, 800 bins.	
Number of histories	6×10^6 primary protons.	
Postprocessing	Depth dose profiles were used to determine R_{80}. Fluence data were used to determine the fluence correction factor for the material.	

3.2.5.1. Range and RSP

The PDD for the proton beam in each material was calculated. The range was determined from the PDD and was defined as the R_{80}, the depth distal to the Bragg peak where the PDD drops to 80%. The range also provides the RSP ($\mathrm{RSP}_m^{\mathrm{MC}}$), which is determined by the following equation:

$$\mathrm{RSP}_m^{\mathrm{MC}} = \frac{R_{80,w}^{\mathrm{MC}}}{R_{80,m}^{\mathrm{MC}}} \tag{3.16}$$

where $R_{80,w}^{\mathrm{MC}}$ is the distal R_{80} range in water and $R_{80,m}^{\mathrm{MC}}$ is the distal R_{80} range in the mixture.

3.2.5.2. Fluence correction factor

The fluence correction factor, $k_{\mathrm{fl}}^{\mathrm{MC}}$, provides information on the difference in fluence between materials [135,136]. The fluence difference provides an understanding of the differences in non-elastic nuclear cross sections of the material compared to the target tissue. Consequently, if $k_{\mathrm{fl}}^{\mathrm{MC}} = 1$, this suggests that the material and target tissue are equivalent in terms of particle fluence [135].

$$k_{\mathrm{fl}}^{\mathrm{MC}}\left(z_{\mathrm{t-eq}}\right) = \frac{\sum_k [\int_{E\,\min,k}^{E_{\max,k}} \Phi_{t,k}(E) \cdot \left(\frac{S(E)}{\rho}\right)_t \mathrm{d}E]}{\sum_k [\int_{E\,\min,k}^{E_{\max,k}} \Phi_{m,k}(E) \cdot \left(\frac{S(E)}{\rho}\right)_t \mathrm{d}E]} \tag{3.17}$$

where $z_{\mathrm{t-eq}}$ represents equivalent depths in the target tissue, k represents the charged particle types, $E_{\max,k}$ the maximum energy and $E_{\min,k}$ the minimum energy of particle type k in the fluence distribution, $\Phi_{t,k}(E)$ the fluence differential in energy for either the material (m) or the target tissue (t) for each particle type *k*, and $\left(\frac{S(E)}{\rho}\right)_t$ the energy-dependent mass stopping power of the target tissue.

3.2.6. Experimental validation of mixtures and commercial materials

3.2.6.1. Semi-analytical model

Manufacture of DB#1 formulation showed the low percentage of CB4 and high percentage of powder resulted in a thick mixture consistency which was not pourable into a mould. Moreover, the development of tissue-equivalent plastic materials using the semi-analytical model by manual interactions was slow and inefficient hence no further cortical bone materials were manufactured using this model. Research moved onto the development of tissue-equivalent plastic materials through the cost-function model.

A preliminary study was designed to compare real bone material against commercial bone-equivalent materials for photon and proton measurements. Further information on the bone-equivalent study can be found in the Appendices, section C.

3.2.6.2. Cost-function model

Selected vertebra and muscle formulations derived by the cost-function model were manufactured by the Barts Health NHS Trust: VB4#1 and VB4#2 as well as MS#1, MS#2, MS#3, MS#3 v2, MS#4, MS#5, and MS#6. A series of tests were performed at the NPL, UCLH Proton Centre, and Rutherford Cancer Centre Thames Valley to characterise the plastic materials to ensure they were within suitable uncertainties for use in proton therapy. For each formulation, three blocks were manufactured with the following dimensions: 10 cm x 10 cm slabs of 0.5 cm, 1.0 cm, and 2.0 cm thick.

3.2.6.2.1. Density

The measured material density of the three individual slabs was calculated by weighing them individually on a Mettler Toledo analytical balance (Model PG503 S) and performing length measurements with Mitutoyo Absolute IP 67 digital callipers (Model CD 8PSX).

3.2.6.2.2. Relative Stopping Power

Measurements were taken at UCLH Proton Centre using a mono-energetic scanning proton beam. An IBA Giraffe device (IBA Dosimetry, Schwarzenbruck, Germany), a multi-layer ionization chamber consisting of 180 large-area ionisation chambers (12 cm diameter), was used to provide a complete Bragg peak depth-dose curve in one irradiation. For VB#1 and VB#2 a 140 MeV proton beam was used. For MS#1. MS#2, MS#3, MS#3 v2, MS#4, MS#5, and MS#6 a 200 MeV proton beam was used. It should be noted that water-equivalent thickness measurements are approximately independent of energy over the clinical proton energy range. Ionisation chamber measurements were performed to determine the water-equivalent thickness (WET) and RSP of the tissue-equivalent materials ($\mathrm{RSP}_m^{\mathrm{Exp}}$) by the same method described in Chapter 2, section 2.3.2.1. The R_{80} values were determined via the IBA detector software which applied the Bortfeld fit to the Bragg peak curve before interpolating the R_{80} range [146]. Thickness measurements of the slabs were taken from the length measurements from mass density calculations (Chapter 3, section 3.2.6.2.1.).

3.2.6.2.3. Single-energy CT and Dual-energy CT

Each slab was scanned in a Mediso AnyScan SCP scanner at the NPL. Once again, the samples were placed centrally within custom made inset within bolus sheets

and solid water was placed above and below the setup on the carbon fibre CT couch. The following scanner settings were used; axial scan, 80 kV, 100 kV, 120 kV, and 140 kV tube voltages, voxel size of 0.098 x 0.098 x 0.125 cm^3, tube current of 300 mA and scan reconstruction of abdomen. Each slab (0.5 cm, 1.0 cm, and 2.0 cm) was scanned separately as well as scanned together as a 10 cm x 10 cm x 3.5 cm block.

CT scans were also performed on two clinical CT scanners; the Phillips CT 5700 scanner at the UCLH Proton Centre and the Phillips Big Bore CT scanner at the Rutherford Cancer Centre Thames Valley. The custom bolus and solid water setup were also used at both clinical centres. At UCLH Proton Centre, the following scanner settings were used; axial scan, Brain CT reconstruction, 120 kV tube voltage, voxel size of 0.049 x 0.049 x 0.1 cm^3, and variable mA. The 0.5 cm, 2.0 cm and 3.5 cm thickness slabs were scanned separately. Due to time constraints the 1.0 cm slab was not scanned. Whilst at the Rutherford Cancer Centre Thames Valley, the following scanner settings were used; Helical scan, Abdomen CT reconstruction, 120 kV tube voltage, voxel size of 0.117 x 0.117 x 0.2 cm^3, and variable mA. Each slab was scanned separately (0.5 cm, 1.0 cm, and 2.0 cm) as well as scanned together as a 10 cm x 10 cm x 3.5 cm block.

3.2.6.2.3.1. Homogeneity

Homogeneity of the samples was tested through visual assessment of the single energy CT (SECT) images taken from the NPL. Visual examination looked for any air bubbles and marbling effects in slices from the CT images as well as assessment of the materials variability through HU SD calculations for each sample. The SD of the average of HU values of the samples was compared to WT1 to quantitively assess their homogeneity. WT1 is a commercial photon solid water-equivalent material that

has been shown to be acceptably homogeneous and it is extensively used in conventional radiotherapy. A plastic bottle filled with distilled water was also scanned alongside the samples to provide information on HU variation due to CT scanner noise.

3.2.6.2.3.2. HU and CT-based RSP estimation

Raystation 10B (version 10.1.100) was used to determine the HU of the material by manually contouring the central regions of each slab. The average HU values of the materials were derived from taking the HU value of the individual slabs (0.5 cm, 1.0 cm, and 2.0 cm) as well as the combined 3.5 cm thick slab setup. The HU values for the three individual slab thicknesses were then applied to the stoichiometric calibration curves for each scanner and the assigned RSP compared to experimentally derived RSP values. The average predicted RSP and respective SD were determined. Dual energy CT (DECT) analysis was also completed to predict RSP according to the stoichiometric method of Bourque *et al.* [147] with the 100 kVp and 140 kVp scan data from NPL.

3.3 Results

3.3.1. Model predicted material radiation parameters

Table 3.4 shows the semi-analytical model results for the new cortical bone formulation and commercial bone materials against human cortical bone. The Z/A and lnI are provided in the table as they offer an understanding of the electron density of the formulation and the energy to excite the atom from the ground to an excited state respectively. These factors in turn impact the stopping power of the material. Tables 3.5 and 3.6 show the cost-function model results for new vertebra bone and muscle formulations as well as commercial tissue-equivalent materials against respective

target tissues. As a relative comparison of new formulations and commercial materials, each materials cost value was determined. The smaller the cost function the better agreement between the plastic formulation to the target tissue. The following cost function weightings were used; i) cost function (1) used the weighting seen in Table 3.2 for VB#1-2 and MS1, ii) cost function (2) used the weighting seen in Table 3.2 for MS#2-4

Table 3.4 *Comparison of new formulation and commercial cortical bone-equivalent materials against their target tissue. Cell colour key: green box = within ±1%, yellow box = within ±2% and orange box = within ±5%*

Physical and Radiation properties	Cortical Bone (ICRP)	DB#1	Accura Bluestone	CIRS Cortical Bone	CIRS Dense Bone (1250 mg/cc)	Delrin	Gammex Cortical bone (SB3)	Hard Cortical (SB5)	NPL Bone
Density (g cm^{-3})	1.85	1.84	1.78	1.91	1.82	1.43	1.83	1.84	1.32
% difference to target tissue	N/A	-0.54	-3.78	3.24	-1.62	-23.0	-1.35	-0.54	-28.6
Z/A	0.52	0.52	0.51	0.51	0.52	0.53	0.52	0.51	0.53
% difference to target tissue	N/A	-1.15	-1.54	-1.34	-0.96	2.3	-0.96	-1.73	1.00
LnI (eV)	4.67	4.67	4.66	4.71	4.69	4.35	4.65	4.68	4.42
% difference to target tissue	N/A	0.00	-0.21	0.86	0.43	-6.9	-0.43	0.21	-5.40
HU	1120.00	1107.00	839.00	1190.00	1307.00	372.51	1115.00	1120.00	466.98
% difference to target tissue	N/A	-1.16	-25.09	6.25	16.70	-66.7	-0.45	0.00	-58.3
Mass Stopping power (MeV cm^2 g^{-1})	6.98	6.87	6.88	6.84	6.87	7.44	6.93	6.84	7.27
% difference to target tissue	N/A	-1.48	-1.43	-1.95	-1.46	6.60	-0.69	-1.88	4.20
Scattering length (g cm^{-2})	33.66	34.31	38.89	33.35	33.14	50.25	34.48	34.23	42.21
% difference to target tissue	N/A	1.93	15.54	-0.92	-1.54	49.3	2.44	1.69	25.4
Range (cm) (at 200 MeV)	15.63	15.93	16.48	15.44	16.12	19.05	15.95	16.02	21.93
% difference to target tissue	N/A	1.92	5.44	-1.22	3.13	21.9	2.05	2.50	34.5

Table 3.5 *Comparison of new formulations and commercial bone materials against vertebra bone. Cell colour key: green box = within ±1%, yellow box = within ±2% and orange box = within ±5%*

Physical and Radiation properties	Vertebra Bone	VB#1	VB#2	CIRS Bone 800 mg/cc HA	Gammex Bone #480	Gammex Bone #484	Leeds Test Object (Average Bone)
Mass Density *	1.42	1.44	1.43	1.53	1.56	1.34	1.40
% difference to target tissue	N/A	1.41	0.70	7.75	9.86	-5.99	-1.41
Z/A	0.530	0.522	0.523	0.526	0.523	0.532	0.528
% difference to target tissue	N/A	-1.49	-1.25	-0.67	-1.25	0.53	-0.38
Ln(I) (eV)	4.51	4.52	4.52	4.54	4.54	4.39	4.44
% difference to target tissue	N/A	0.04	0.21	0.65	0.46	-2.72	-1.65
Electron Density ($cm^{-3)}$	1.36	1.35	1.35	1.45	1.47	1.28	1.33
% difference to target tissue	N/A	-0.10	-0.55	7.02	8.49	-5.49	-1.78
Mass attenuation coefficient ($cm^2\ g^{-1}$) *	0.333	0.336	0.334	0.395	0.360	0.296	0.309
% difference to target tissue	N/A	1.16	0.46	18.83	8.09	-10.90	-6.96
RSP *	1.32	1.32	1.31	1.41	1.43	1.27	1.31
% difference to target tissue	N/A	-0.12	-0.67	6.63	8.20	-4.02	-0.85
Scattering Length (cm) *	27.2	27.5	27.4	24.1	24.5	32.9	30.2
% difference to target tissue	N/A	1.02	0.54	-11.45	-10.20	20.57	10.85
Average Reaction Cross-section *	0.0208	0.0211	0.0209	0.0206	0.0209	0.0215	0.0214
Average Production Cross-section* (secondary protons)	0.557	0.576	0.565	0.548	0.564	0.600	0.592
Average Production Cross-section (alpha particles)	0.156	0.155	0.155	0.156	0.156	0.154	0.154
% difference to target tissue	N/A	2.61	1.65	1.82	1.57	5.42	4.47
Cost function (1)	NA	1.79	0.66	133.66	68.76	101.43	31.09

Table 3.6 *Comparison of new formulation and commercial muscle materials against skeletal muscle. Cell colour key: green box = within ±1%, yellow box = within ±2% and orange box = within ±5%*

Physical and Radiation properties	Muscle	MS#1	MS#2	MS#3	MS#4	MS#5	MS#6	CIRS Muscle	Gammex Muscle
Mass Density *	1.05	1.07	1.06	1.06	1.06	1.05	1.05	1.06	1.05
% difference to target tissue	NA	1.94	0.97	1.00	1.36	0.00	0.00	1.14	0.00
Z/A	0.550	0.534	0.536	0.536	0.530	0.542	0.53	0.544	0.540
% difference to target tissue	NA	-2.91	-2.52	-2.49	-3.72	-1.37	-1.31	-1.02	-1.91
Ln(I)	4.31	4.34	4.28	4.28	4.36	4.23	4.23	4.22	4.25
% difference to target tissue	NA	0.54	-0.75	-0.75	1.16	-1.82	-1.81	-2.19	-1.41
Electron Density	1.04	1.03	1.02	1.02	1.02	1.04	1.03	1.04	1.02
% difference to target tissue	NA	-1.06	-1.59	-1.56	-2.42	-0.53	-0.93	0.12	-1.91
Mass attenuation coefficient*	0.221	0.223	0.219	0.219	0.218	0.221	0.221	0.219	0.219
% difference to target tissue	NA	1.00	-0.93	-0.97	1.33	0.00	0.00	1.06	0.83
HU	46.7	77.3	46.8	46.4	46.8	46.7	46.7	47.4	37.9
% difference to target tissue		65.61	0.25	-0.54	0.16	0.00	0.00	1.53	-18.71
RSP *	1.042	1.028	1.029	1.029	1.010	1.037	1.038	1.055	1.029
% difference to target tissue	NA	-1.34	-1.20	-1.16	-3.02	-0.41	-0.35	1.28	-1.18
Scattering Length (cm) *	45.7	45.9	49.1	49.2	46.5	50.8	50.6	50.8	50.5
% difference to target tissue	NA	0.62	7.60	7.67	1.75	11.16	10.87	11.24	10.51
Average Reaction Cross-section*	0.0219	0.0218	0.0222	0.0222	0.0220	0.0222	0.0218	0.0223	0.0223
Average Production Cross-section* (secondary protons)	0.607	0.618	0.639	0.640	0.632	0.644	0.643	0.647	0.643
Average Production Cross-section (alpha particles)	0.153	0.151	0.151	0.152	0.151	0.151	0.151	0.151	0.151
Average nuclear interactions % difference to target tissue	NA	2.86	4.93	5.06	4.11	5.60	5.48	5.84	5.44
Cost function (1)	NA	2.61	11.46	11.76	5.82	20.30	19.29	21.86	18.75
Cost function (including HU) (2)	NA	N/A	9.70	9.99	4.91	17.18	16.32	18.88	75.39

3.3.2. Validation of material radiation parameters

3.3.2.1. Monte Carlo simulations

3.3.2.1.1. Range and RSP

Figures 3.2-4 graph a) show the $R_{80,m}^{\mathrm{MC}}$ range values determined from the simulation for the new formulations and commercial tissue-equivalent materials as well as their corresponding target tissue, $R_{80,t}^{\mathrm{MC}}$, for a 200 MeV proton beam. Figures 3.2-4 graphs b) represent the $\mathrm{RSP}_m^{\mathrm{MC}}$ values determined from the simulation for the new formulations and commercial tissue-equivalent materials as well as their corresponding target tissue, against water for a 200 MeV proton beam. Figures 3.2-4 graph c) and d) show the absolute relative difference of new formulations and commercial tissue-equivalent materials to their corresponding target tissues for $R_{80,m}^{\mathrm{MC}}$ and the $\mathrm{RSP}_m^{\mathrm{MC}}$ values respectively. The relative difference between the semi-analytical model and Monte Carlo simulation predicted ranges was 1.0% (SD = 0.5%). The relative difference between the cost-function model and Monte Carlo simulation predicted RSP was 0.4% (SD = 0.4%).

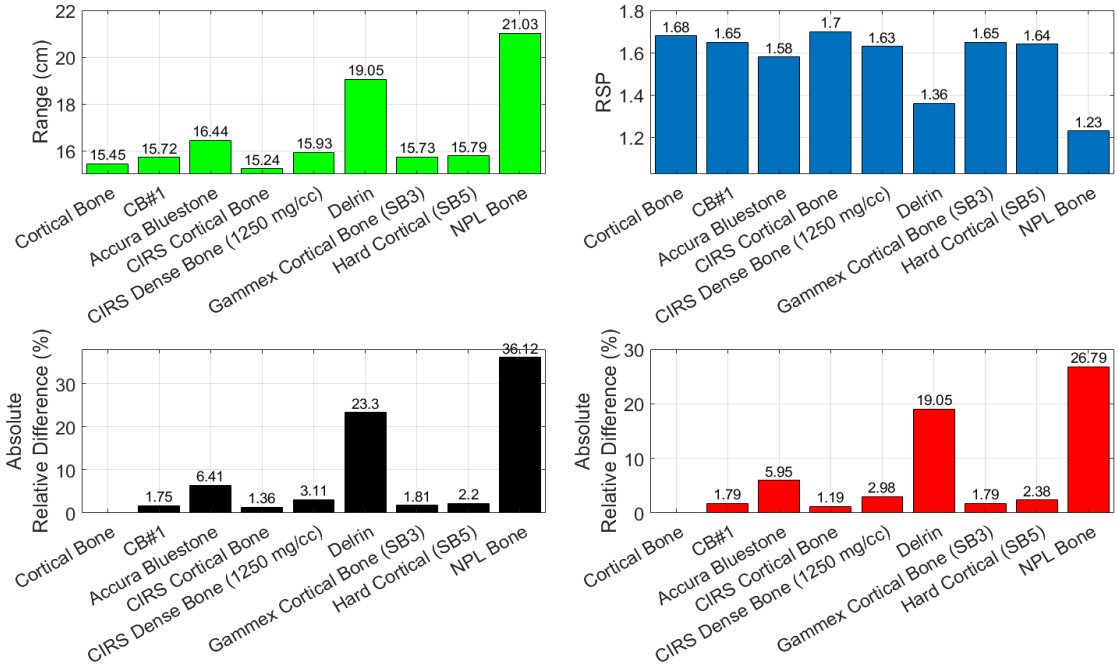

Figure 3.2 *Monte Carlo derived $R_{80,m}^{MC}$ and RSP_m^{MC} values for cortical bone and cortical bone plastics are presented in Figure 3.2 a) and b). Their respective relative difference to the target tissue are presented in Figure 3.2 c) and d)*

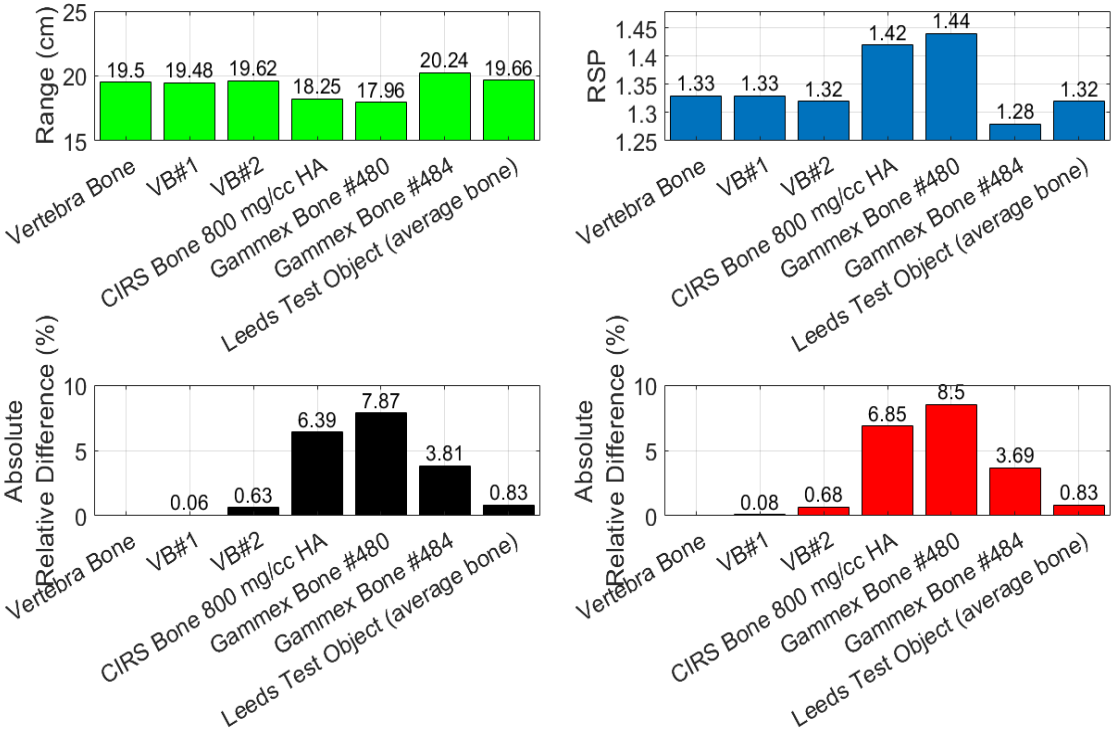

Figure 3.3 *Monte Carlo derived $R_{80,m}^{MC}$ and RSP_m^{MC} values for vertebra bone and bone plastics are presented in Figure 3.3 a) and b). Their respective relative difference to the target tissue are presented in Figure 3.3 c) and d) .*

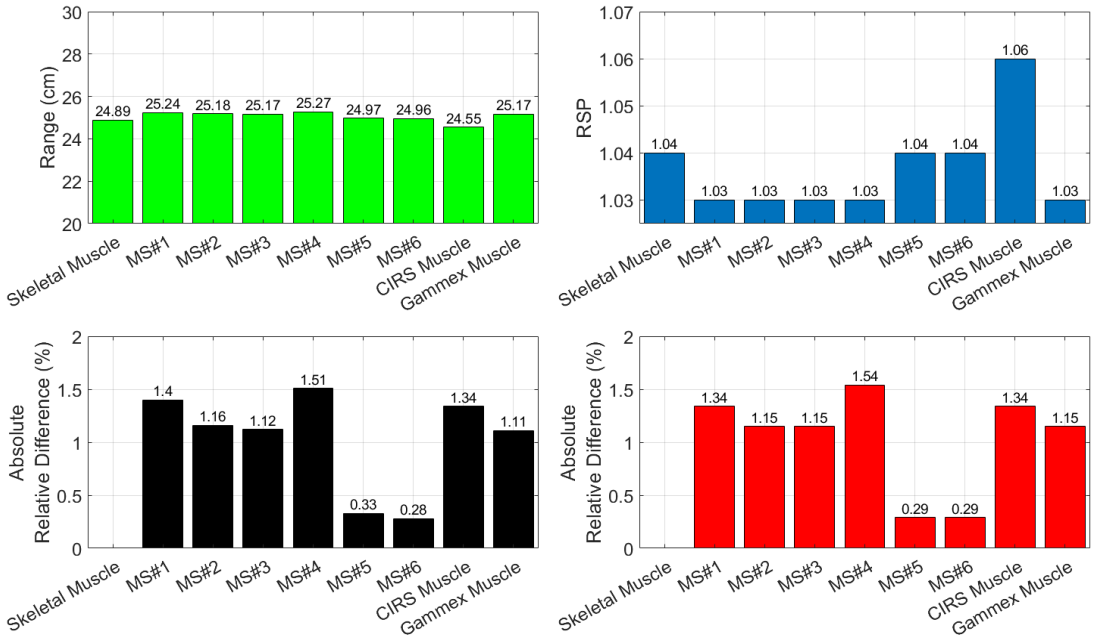

Figure 3.4 *Monte Carlo derived $R_{80,m}^{MC}$ and RSP_m^{MC} values for muscle and muscle plastics are presented in Figure 3.4 a) and b). Their respective relative difference to the target tissue are presented in Figure 3.4 c) and d) muscle and muscle plastics are present in Figure 3.4 a) and b). Their respective relative difference to the target tissue are presented in Figure 3.4 c) and d) .*

3.3.2.1.2. Fluence correction factor

Figure 3.5 a) shows the comparison of the fluence correction factor between semi-analytical model (lines) and Monte Carlo simulation (dots) for CB#1. Figure 3.5 b) shows the comparison of fluence correction factor for all charged particles for CB#1 and bone-equivalent materials from Monte Carlo simulation data. The depth was scaled to the range of the target tissue.

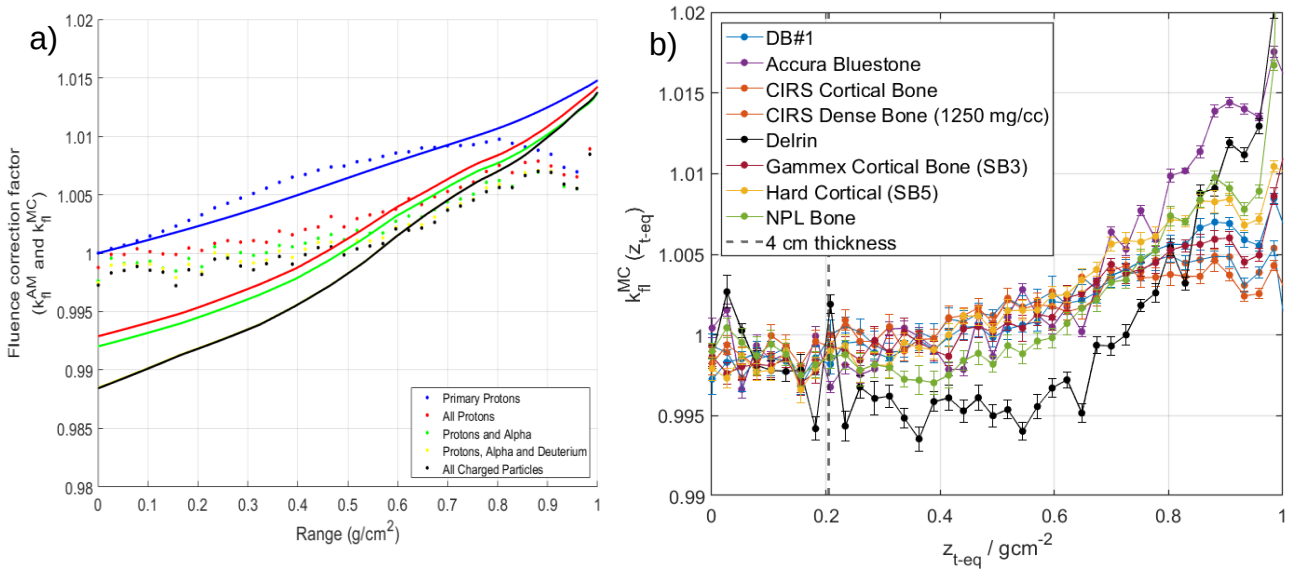

Figure 3.5 *a) shows the fluence correction factor between semi-analytical model (lines) and Monte Carlo simulation (dots) for CB#1. b) shows the comparison between CB#1 and commercial bone-equivalent materials. Reference dashed lines highlighted maximum tissue thicknesses of each target tissue a proton may pass through in a patient (4 cm for bone). Type A uncertainties are presented with each error bar.*

Figure 3.6 a) and b) shows the fluence correction factor for new vertebra bone and muscle formulations, respectively as well as commercial tissue-equivalent materials against respective target tissues. The depth was scaled to the range of the target tissue.

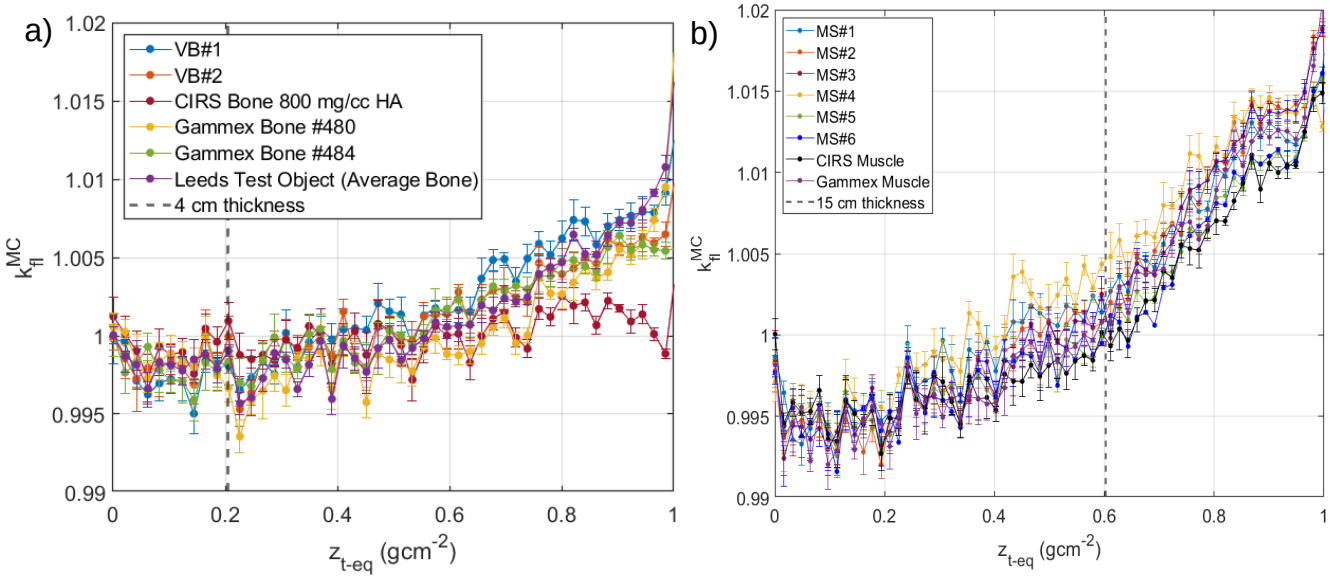

Figure 3.6 *Fluence correction factor comparison between new vertebra bone formulations and commercial bone-equivalent materials, b) Fluence correction factor comparison between new muscle formulations and commercial muscle-equivalent materials. Reference dashed lines highlighted maximum tissue thicknesses of each target tissue a proton may pass through in a patient (4 cm for bone and 15 cm for muscle). Type A uncertainties are presented with each error bar.*

3.3.2.2. Experimental validations

3.3.2.2.1. Homogeneity

Table 3.7 shows the HU values and SD for each material. Figure 3.7 shows an example slice of each new formulation, VB#1, VB#2, MS#1, MS#2 MS#3, MS#3 v2, MS#4, MS#5, MS#6. A 5 HU variation was attributed to scanner noise. CT scans were checked for air bubbles as well as assessing the heterogeneity of the materials. MS#2 was shown to have air bubbles within the sample (highlighted in red on Figure 3.7) and heterogeneity of samples can be seen visually as well as quantitively by the large SD of MS#1, MS#2, and MS#4. Powder settlings can be seen in MS#1 and MS#4 (Figure 3.7). The overall SD of the other samples (VB#1, VB#2, MS#3, MS#3 v2, MS#5 and MS#6) was on the same level as WT1, in particular for MS#5 and MS#6.

Table 3.7 *HU values and standard deviation of vertebra bone, muscle samples and solid water (WT1).*

Material	Min HU	Mean HU	Max HU	SD
WT1	-38	9.17	44	8
VB#1	546	634	705	20
VB#2	490	611	675	20
MS#1	-178	82	439	190
MS#2	-388	47	141	59
MS#3	-44	52	110	21
MS#3 v2	-116	26	86	24
MS#4	1	99	232	78
MS#5	-6	51	81	9
MS#6	6	48	79	10

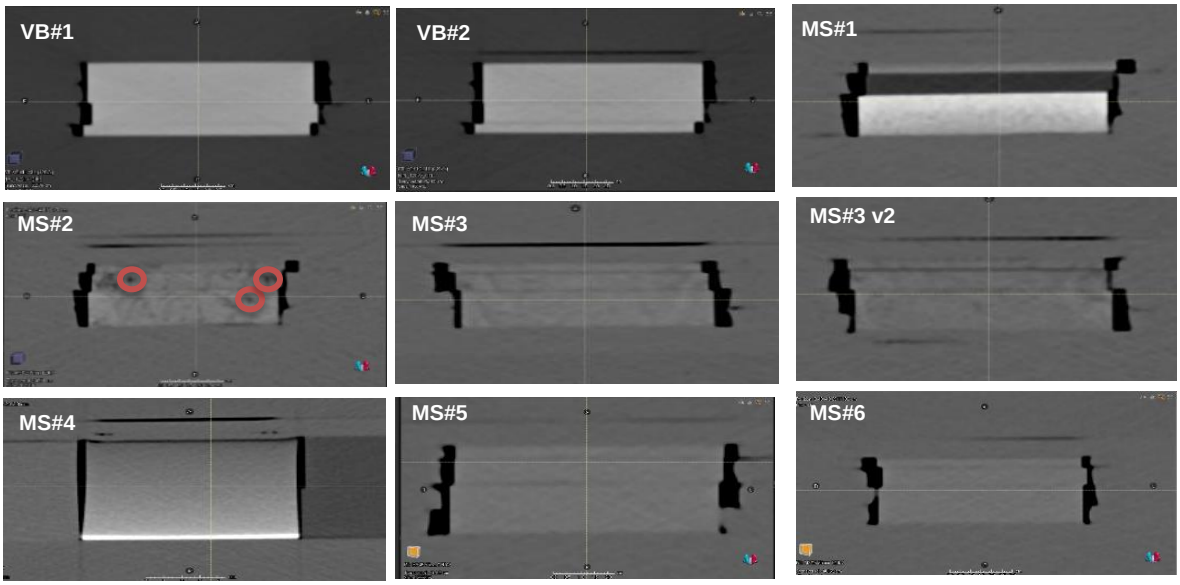

Figure 3.7 *Example CT slices of new formulations. For MS#4 the sample was not cut into slabs to better evaluate the powder setting properties. Air bubbles shown in red circles on figure.*

3.3.3.2. Density and RSP measurements

Table 3.8 shows the experimental calculated density and RSP values for the new formulations. The table also shows the relative difference comparisons between experimental and model predicted values of mass density and RSP as well as comparing experimental values against target tissues. The cost-function model on average predicted the experimental material density within 1.3% (SD = 0.76%) and RSP within 3.0% (SD=1.27%) when MS#1 and MS#4 were excluded. MS#1 and MS#4 showed significant variation in density between measured slabs shown by the large SD value in HU. For the vertebra bone materials, the experimental values were on average within 2.0% (SD = 0.6%) for mass density and RSP with target human vertebra bone formulation. For the muscle materials (excluding MS#1 and MS#4), the experimental values were on average within 1.7% (SD = 1.0%) for mass density and RSP with target human skeletal muscle formulation. For MS#3 and MS#3 v2, the

addition of phenolic microspheres reduced the relative percentage point difference to the target skeletal muscle by 1.7% for mass density and 2.4% for RSP.

Table 3.8 *Mass density and RSP measurements of samples. Due to MS#1 and MS#4 clearly not being suitable for clinical use due to powder settling within sample, their mass density and RSP are not presented in the table.*

Radiation Property	VB#1	VB#2	MS#2	MS#3	MS#3 v2	MS#5	MS#6
Average mass density (SD)	1.458 (0.003)	1.443 (0.004)	1.056 (0.04)	1.080 (0.01)	1.055 (0.02)	1.059 (0.001)	1.054 (0.001)
Average relative % difference to model prediction (SD)	1.25 (0.24)	0.91 (0.25)	2.67 (1.43)	1.79 (0.98)	1.04 (0.22)	0.83 (0.06)	0.36 (0.11)
Average relative % difference to target tissue (SD)	2.69 (0.25)	1.62 (0.25)	2.37 (2.20)	2.85 (1.03)	1.11 (1.13)	0.84 (0.06)	0.37 (0.11)
Average RSP (SD)	1.354 (0.003)	1.342 (0.001)	1.052 (0.01)	1.067 (0.01)	1.051 (0.01)	1.064 (0.01)	1.061 (0.003)
Average relative % difference to model prediction (SD)	2.43 (0.23)	2.08 (0.06)	2.14 (1.28)	4.34 (0.65)	2.08 (0.45)	2.82 (0.62)	2.21 0.23
Average relative % difference to target tissue (SD)	2.37 (0.24)	1.44 (0.06)	0.98 (1.33)	3.33 (0.07)	0.91 (0.48)	2.13 (0.65)	1.90 (0.24)

3.3.3.3. HU and CT-based RSP estimation

Table 3.9 compares predicted RSP from NPL, UCLH Proton Centre, and Rutherford Cancer Centre Thames Valley, CT stoichiometric calibrations against experimental RSP values. The table shows that at NPL all materials can be assigned the correct RSP on average within 1.4% (SD=0.5%) difference when using single-energy CT, this is reduced to on average within 1.3% (SD= 0.4%) if dual energy CT method is applied. At UCLH Proton Centre, all materials can be assigned the correct RSP on average within 2.3% (SD=0.9%) and for the Rutherford Cancer Centre Thames Valley all materials can be assigned the corrected RSP within 1.9% (SD = 1.3%).

Table 3.9 HU and CT-based RSP estimation results for CT scanners. Due to MS#1 and MS#4 having powder settling within sample, the sample were not CT scanned at UCLH Proton Centre as they were deemed unsuitable for clinical use. MS#5 and MS#6 were not yet developed when samples were tested at Rutherford Cancer Centre Thames Valley.

Location and type of CT scan	Radiation Property	VB#1	VB#2	MS#2	MS#3	MS#3 v2	MS#5	MS#6
NPL (SECT 120kV)	Average HU (SD)	633 (10)	609 (9)	50 (22)	52 (5)	26 (12)	51 (2)	48 (1)
	Average predicted RSP (SD)	1.377 (0.01)	1.364 (0.01)	1.049 (0.02)	1.054 (0.01)	1.034 (0.01)	1.054 (0.001)	1.051 (0.000)
	Average relative % difference to experimental RSP (SD)	1.67 (0.61)	1.62 (0.43)	0.57 (0.61)	2.04 (0.67)	1.61 (0.66)	0.95 (0.59)	0.96 (0.23)
NPL (DECT (100kV and 140kV)	Average HU (SD)	704 (7) and 581 (12)	674 (4) and 558 (11)	52 (22) and 49 (22)	49 (5.4) and 53 (6)	24 (12) and 29 (11)	54 (2) and 49 (2)	50 (1) and 46 (1)
	Average predicted RSP (SD)	1.355 (0.10)	1.346 (0.04)	1.049 (0.03)	1.060 (0.01)	1.035 (0.01)	1.053 (0.001)	1.050 (0.0002)
	Average relative % difference to experimental RSP (SD)	0.64 (0.48)	1.91 (1.61)	0.94 (0.82)	1.50 (0.71)	1.57 (0.89)	1.05 (0.59)	1.10 (0.23)
UCLH Proton Centre (Spectral CT)	Average HU (SD)	692 (6)	662 (7)	47 (23)	41 (9)	16 (10)	50 (1)	46 (1)
	Average predicted RSP (SD)	1.331 (0.003)	1.318 (0.003)	1.036 (0.02)	1.034 (0.01)	1.020 (0.01)	1.040 (0.001)	1.038 (0.001)
	Average relative % difference to experimental RSP (SD)	1.70 (0.36)	1.74 (0.29)	1.46 (0.65)	3.89 (0.59)	3.00 (0.39)	2.19 (0.69)	2.24 (0.23)
Rutherford Cancer Centre, Thames Valley (SECT 120kv)	Average HU (SD)	621 (11)	596 (10)	40 (22)	37 (6)	15 (9)	N/A	N/A
	Average predicted RSP (SD)	1.345 (0.01)	1.330 (0.01)	1.037 (0.02)	1.036 (0.01)	1.022 (0.01)	N/A	N/A
	Average relative % difference to experimental RSP (SD)	0.69 (0.55)	0.88 (0.43)	1.38 (0.60)	3.77 (0.69)	2.76 (0.32)	N/A	N/A

3.4 Discussion

The semi-analytical model highlighted the importance of careful selection of bone-equivalent materials for proton therapy. Table 3.4 clearly shows plastics such as Delrin are not suitable to mimic cortical bone and could cause up 19% uncertainty for range and 50% uncertainty in scattering properties. Gammex bone SB3 and Hard bone SB5 were shown to perform best from the commercial materials, with all physical and radiation properties within 3% of that of the target tissue. However, with the semi-analytical model it was possible to tweak the elemental formulation (CB#1) to further optimise the material to mimic both photon and proton properties within 2%. Semi-analytical model results were validated by Monte Carlo simulation data; with agreement of range within 1.0 % (SD = 0.53%). This first stage of work highlighted the potential of developing tissue-equivalent materials better optimised for proton therapy. However, the new formulations were unable to be successfully manufactured due to epoxy resin manufacture constraints and the semi-analytical model was found to be a slow and inefficient method for developing new formulations.

Therefore, the cost-function model was developed to formulate proton optimised tissue-equivalent materials using a non-linear optimisation framework which included manufacture constraints as part of the model. Tables 3.5-6 highlight the overall potential of the new formulations to perform better than current commercial tissue-equivalent materials when mass density, photon interactions and proton interactions are determined via a weighted cost function. Materials that scored well (close to zero) via the weighted cost function have the potential to provide accurate proton dosimetry.

From Tables 3.5-6, VB#1-2 and MS#1 were shown to provide the best optimisation of radiation parameters, however, manufacture challenges meant formulations didn't always result in suitable homogenous mixtures. Table 3.7 and Figure 3.7 highlight the unsuccessful mixing of MS#1 into a homogenous mixture due to the powdered material settling during the curing process. Table 3.7 shows MS#1-2 and MS#4 have significant variation in HU from the mean which suggest that these materials should not be used for clinical phantom use. Significant HU variation of the material is an undesirable material trait for certain applications such as phantoms for reference dosimetry and profile measurements. However, for use in anthropomorphic phantom for end-to-end audits, minor HU variation could be useful as this would simulate human tissue heterogeneity. This could provide rigorous testing of the TPS and dose calculations during the patient workflow audit. Nevertheless, the challenge of having inhomogeneous plastics is capturing HU variation which is clinically relevant and distinguished within the CT image.

After a review of muscle iterations, the optimisation was simplified to focus on the manufacture of a homogeneous material, MS#5-6. The development of a homogenous material was at the cost of optimising the phantom material for all proton interactions and resulted in a formulation more comparable to current commercial muscle materials. This study shows that phantom manufacture is still a trial-and-error process with no perfect formula for the manufacture of both a homogenous and optimised material.

The cost function model's ability to predict physical and radiation properties were assessed against measured values from the manufactured samples and Monte Carlo simulations. Overall, results from Table 3.8 indicated that the model can predict mass

density and radiation properties within the relative standard uncertainty of the method of calculation. The model predicted the RSP and mass density of the materials within 1.5% (when RSP calculations are corrected for experimental density values). In addition, RSP values were on average within 0.36% relative between the cost-function model and Monte Carlo simulations values. Monte Carlo simulations also provided further information on the dosimetric properties, in particular range and nuclear interactions.

Figures 3.3-4 show that all formulated materials match the target tissue ranges between 0.1-1.4%. These materials also perform better than commercial materials; the commercial bone materials showed relative difference up to 8% for range. Contrary to cost-function model predictions of improved nuclear interactions, Monte Carlo results showed the fluence correction factor of the new formulations were comparable to commercial tissue-equivalent materials. The fluence correction is shown to be around 0.5% for vertebra bone formulations (Figure 3.6 a)) and 1.0% for muscle formulations (Figure 3.6 b)). This suggests a higher weighting of the nuclear interaction parameters may be necessary or the current parameter does not fully capture the nuclear interactions of the targeted material.

Some uncertainty can be attributed to the nuclear data used in the model compared to Monte Carlo simulations. The model uses ICRU Report 63 data which reports uncertainties of uncertainties of the order of 5%-10% on the total non-elastic cross sections and 20%-30% on the angle-integrated production cross sections for secondary particles [137]; whilst for FLUKA, the PEANUT nuclear model was used. Work by Lourenço et al. (2017) [90] reported at least 2% differences in fluence correction factors depending on the Monte Carlo code. Previous research has also

highlighted the challenge of quantifying the probability of non-elastic nuclear interactions due to hydrogen content of compounds [148]. Consequently, considerations should be made to adapt the model to improve the optimisation for nuclear interactions.

With regards to the tissue-equivalence of the new plastics, Table 3.8 also shows for both the vertebra bone and muscle materials, that formulations were on average within 2% for mass density and $\mathrm{RSP}_m^{\mathrm{Exp}}$ of the human target tissues. Results indicate VB#2 and MS#3 v2 are the most suitable bone and muscle-equivalent materials and outperform many of the existing materials. Major improvements were achieved in comparison to commercial bone materials, which showed relative differences up to 10% and 8% respectively for mass density and $\mathrm{RSP}_m^{\mathrm{MC}}$ (Figure 3.3).

The materials were assessed for their use as phantom materials for audit purposes. As previously mentioned, the acceptance criteria of phantom materials for IROC phantom development is a 5% uncertainty in TPS assigned RSP [78]. Results from SECT and DECT scans at NPL and clinical centres suggest the materials $\mathrm{RSP}_m^{\mathrm{TPS}}$ can be correctly assigned within 1-3% (Table 3.9). The improved homogeneity of MS#5-6 also showed to improve the consistency and accuracy of $\mathrm{RSP}_m^{\mathrm{TPS}}$ assignment of the muscle material. Consequently, the $\mathrm{RSP}_m^{\mathrm{TPS}}$ uncertainty is likely to be masked within the uncertainty of other steps in the phantom audit process such as setup, TPS planning margins, and dosimeter measurement.

Future work will look to apply this model to manufacture proton optimised water and other human tissues (lung and denser bone) materials as well as being applied to support research into 3D printable based optimised phantom materials.

3.4. Conclusion

A model was developed which proved to be a powerful tool for the formulation of tissue-equivalent materials optimised for proton dosimetry. This model enabled the creation of new proton optimised tissue-equivalent materials which perform better than current commercial bone and muscle materials when both mass density, photon interactions and proton interactions are determined via a weighted cost function. Materials formulated by the model were manufactured and characterised by Monte Carlo simulations and experimental testing. The best optimised formulations produced during this study were shown to mimic their target human tissues within 1-2% for the mass density and RSP confirming their suitability as clinical phantom materials. The study formulations and future materials developed by the model will be used within clinical phantoms to improve phantom dosimetry measurements.

4. Design and testing of an optimised head and neck phantom with a patient-weight variation feature for proton therapy

The work presented in this chapter is being drafted with co-authors and it will be submitted soon:

Cook H., Niemann N., Gillies C., Rompokos V, Lowe M., Hussein M., Clark C.H., Thomas R., Nisbet A., Royle G., Palmans H., & Lourenço A. Development of the PRoton heaD and NeCk Evaluation (PRuDeNCE) phantom for proton therapy audit. (TBC) (2023) (in preparation)

Cook H., Hussein, M., & Lourenço, A. Report on Proton Head and Neck End-to-End Dosimetry Pilot Audit at University College London Hospital Proton Beam Therapy Centre. NPL audit report, (2023) (drafted)

Cook H., Hussein, M., & Lourenço, A. Report on Proton Head and Neck End-to-End Dosimetry Pilot Audit at The Christie Proton Beam Therapy Centre. NPL audit report, (2023) (drafted)

It has also been presented at the following conferences via oral and poster format:

Cook H., Niemann N., Gillies C., Rompokos V., Lowe M., Hussein M, Clark C.H., Thomas R., Nisbet A., Royle G., Palmans H., & Lourenço, A. A new audit tool for proton therapy: PRoton heaD and NeCk Evaluation (PRuDeNCE) phantom, 61st Annual Conference of the Particle Therapy Co-Operative Group 2023; *Madrid E.S.(Poster)*

My contribution to this publication were as follows; design of the phantom was performed by myself with the support and guidance of NPL staff. Manufacture of the phantom was in collaboration with UCL Electronic and Electrical Engineering workshop, Barts Health NHS Trust and NPL Engineering workshop under my guidance. The weight variation feature was designed by Peter Lovelock (NPL Senior Design Engineer) under my guidance. NPL experiments and proton beam experiments performed at Rutherford Cancer Centres Thames Valley, UCLH and The Christie were performed by me with the assistance of NPL scientists and clinical medical physicists. Analysis and interpretation of the results were performed by me under guidance of my supervisors and NPL scientists; the paper was written by me and proof-read by the co-authors.

4.1. Introduction

The dosimetric advantage of proton therapy for head and neck cancer has been highlighted in a variety of retro- and prospective proton therapy studies [149–154]. Results from these studies advocate protons for dose sparing of important non-target structures such as the oral cavity and parotid glands which has the possibility to reduce adverse side effects such as xerostomia [155] . Therefore, proton therapy has been proposed for the treatment of oropharyngeal cancer [149,151,153,156] and the site is currently subject to a UK clinical trial project (TORPEdO) [157]. The anatomical site can be challenging to treat due to a typically complex tumour target, numerous nearby OAR, heterogeneity and a varying patient shape. Anatomical changes, such as weight loss or tumour shrinkage, are common during the course of treatment and frequently result in treatment replanning [158]. Due to the complexity of the site, a multi-field

optimisation technique is used which is subject to a higher uncertainty in delivery due to the modulation of pencil beam spot weights [159]. Robust planning and quality assurance measures are required to ensure any inherent proton uncertainties and daily variation is considered during the patient treatment.

A vital tool for providing confidence and consistence for clinical trials and complex radiotherapy techniques are dosimetry audits. In a photon head and neck trial, poor radiotherapy quality assurance was shown to result in a 40% decrease in overall survival in patient outcome [160]. Pettersen *et al*. (2008) have shown that reducing uncertainties in dosimetry can strengthen clinical trials and reduce the number of patients required to provide support of a clinical trial hypothesis [161]. The Imaging and Radiation Oncology Group (IROC) have highlighted the importance of proton audits within the U.S. for the past ten years. Paige *et al.* (2022) demonstrated the worth of independent dosimetry audits within clinical proton therapy centres; with institutions receiving an average of three recommendations for improved practice. Therefore, audits can provide a solution to ensure the quality and best practice for clinical trials and radiotherapy treatments.

Previous work by the IROC team have looked to modify an Anderson Head and Neck phantom to assess the accuracy of proton treatment of the oropharyngeal cancer site. Film and thermo-luminescent detectors were used within the phantom to measure point doses and relative doses for comparison with the treatment planning system (TPS). Results show that the clinical centre passed the acceptance criteria set for the phantom (±7%/4 mm gamma analysis) [72]. Meanwhile Nenoff *et al.*, (2021) have looked to adapt a commercial head and neck phantom to include patient variation

features with a focus on nasal filling for testing of daily adaptive planning techniques for base of skull tumours [80].

In this work, a new PRoton heaD and NeCk Evaluation phantom (PRuDeNCE) was developed and tested as an end-to-end audit device to assess the full patient workflow (imaging, planning, in-room setup, and proton delivery). This phantom was developed to assess an oropharyngeal cancer site that required treatment of the nodal regions within the whole neck region of the patient. The phantom was manufactured from new proton-optimised tissue-equivalent materials developed specifically for end-to-end proton therapy audit phantoms. A prototype weight-variation shell was also developed to assess the influence of weight change on patient plans as well as to test adaptive planning techniques. The purpose of the current study was to design, evaluate, and test this new head and neck phantom for audit purposes to support clinical centres on the delivery of proton therapy to oropharyngeal cancer site.

4.2. Method

4.2.1. Proton tissue-equivalent materials

The phantom was designed to use plastics that are tissue-equivalent in photon imaging beams and high-energy proton scanning beams. The muscle (MS#6) and vertebra bone (VB#2) equivalent materials were selected for the head and neck phantom. A 3D printable nylon powder (CB PA12) was used to develop a prototype of a weight-variation shell to mimic water or fat gain/loss around the neck region. These materials were characterised by experimental testing at NPL and proton clinical centres, as well as Monte Carlo simulations to assess their suitability for clinical use (material characterisation is described in Chapter 3).

4.2.2. Selection of detectors

A preliminary study was completed at the Rutherford Cancer Centre Thames Valley using a simpler solid water phantom, irradiated by a proton beam, to provide a better understanding of the detectors to be used within the phantom. Results from this study can be found in the Appendices, section D. For absolute dose measurements, a PTW Semiflex Type 31010 ionisation chamber and alanine were selected, and for relative dose distribution measurements, EBT3 film was used in the phantom.

4.2.3. Phantom design and construction

Early-stage work looked to develop a simple cylinder phantom design to enable ease of manufacture (Figure 4.1 a)). Treatment planning on the virtual phantom design in Raystation showed the simplistic and symmetric design caused plan optimisation problems such as hotspots which were accentuated by the cylindrical outer shape. Therefore, a simplified anthropomorphic shape (Figure 4.1 b)) was developed from an anonymous oropharyngeal cancer patient external contour. The contour was simplified into a phantom shape through 3D Slicer [162] and Meshmixer (Autodesk Inc., San Francisco, U.S.A.) software packages. The smoothed external contour was then imported into Solidworks 2021 (Dassault Systèmes SolidWorks Corporation**,** Massachusetts, U.S.A**)** and internal spine region and airways channels were added to the phantom. The head, neck and shoulder regions were included in the phantom design to make the treatment delivery more realistic and challenging with regards to beam angles. The phantom was designed to include vertebra bone, airways, and muscle tissue equivalent regions to simulate the heterogeneous anatomy of a patient.

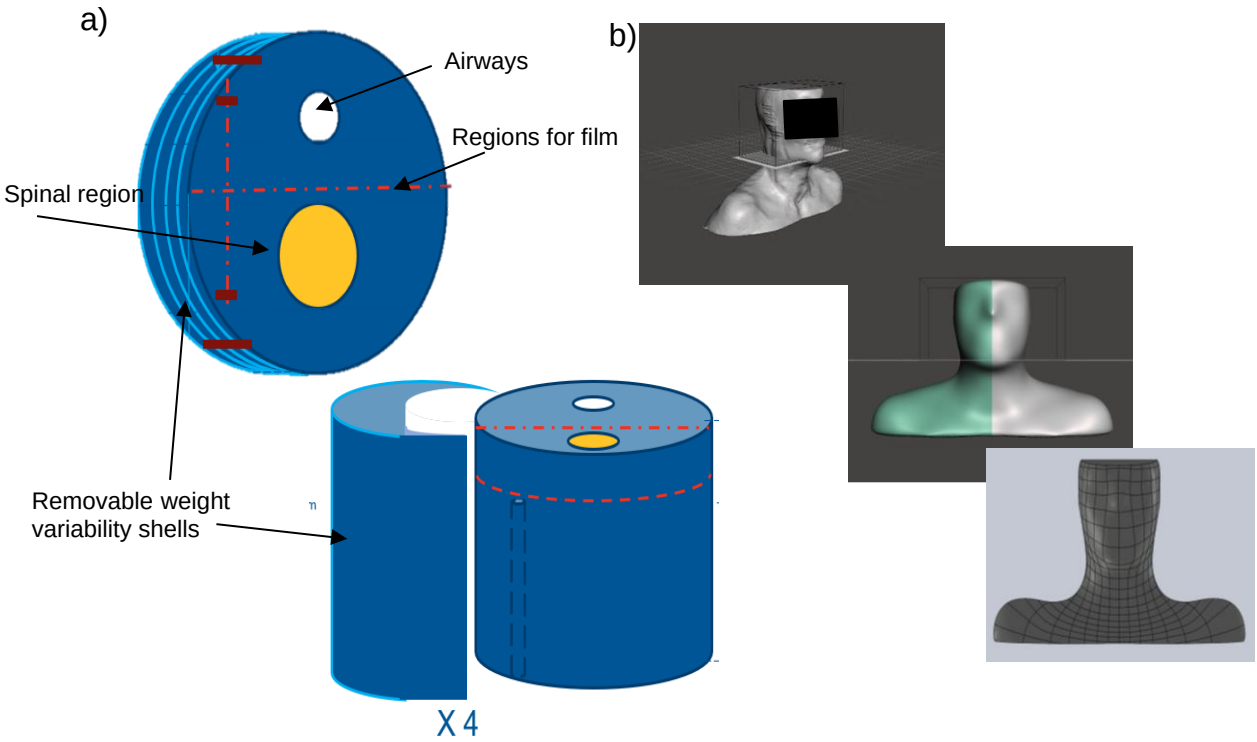

Figure 4.1 *a) Cylindrical phantom design (left to right: axial view, coronal view) b) Anthropomorphic phantom design (left to right: patient contour, smoothed and mirrored contour, phantom shape in Solid works)*

The phantom was designed to include two detector channels for the insertion of either 3 alanine pellets (NPL, UK) or a PTW Semiflex 31010 chamber with their points of measurement at the same location. The detector channels were designed to enable absolute dose measurements within the tumour target region and the spinal cord region of the phantom. It also allows the measurement of dose distribution profiles by EBT3 film (120 cm x 200 cm), in a coronal plane of the phantom which spans the neck region. A 5 mm thick weight-variation shell (Figure 4.2) was designed by extending the phantom contour in the neck region. A shell with a 5 mm thickness was chosen after discussion with clinical physicists and reviewing published data [163–165] on anatomical changes seen clinical in head and neck patients during a course of treatment. The thickness was also influenced by fragility concerns on producing a thin shell structure for use as part of an end-to-end audit. Due to the difficulty of

manufacture of a thin shell structure out of epoxy resin methods, 3D printing was utilised. The shell was printed out of nylon powder, CB PA12, at UCL on a HP Fusion Jet 580. The weight-variation shell was developed to investigate the effects of patient weight variability on complex proton head and neck plans.

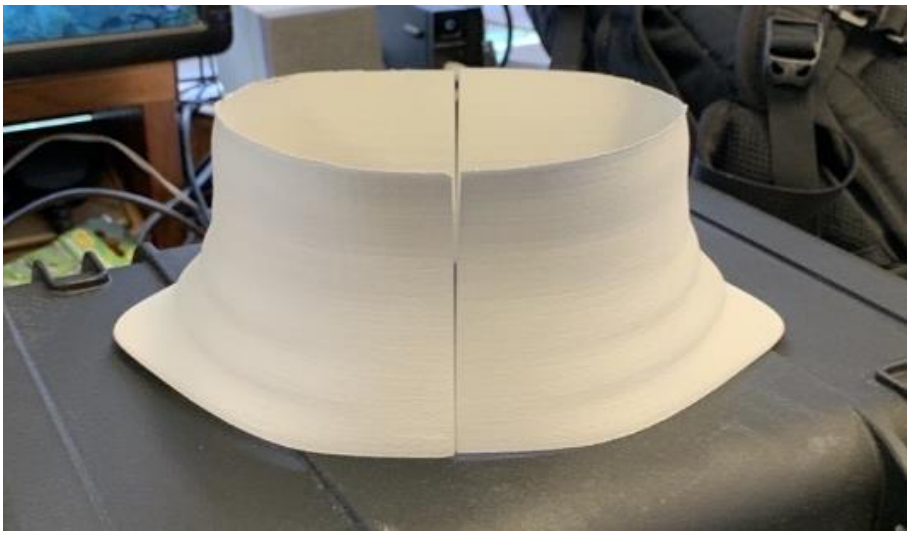

Figure 4.2 *Weight-variation shell*

The bespoke phantom was developed and manufactured in collaboration with UCL Electronic and Electrical Engineering workshop, Barts Health NHS Trust and NPL Engineering workshop. An aluminium mould (Figure 4.3 a)) was manufactured to cast the external shape of the phantom in two halves. The mould included internal rods (Figure 4.3 b) within the airways, spinal region, and tumour region to enable cavities to be created within the phantom which enabled the insertion of tissue-equivalent materials and detector rods without the need for complex cavity drilling into the phantom. The phantom was then milled using computer numerical control (CNC) machine (Figure 4.3 c)) to include the film detector regions, phantom connection regions and head support plate (Figure 4.3 d)). The detector rods were then machined

and tested within the phantom. The rods were CT scanned within the phantom to ensure the rods fitted correctly.

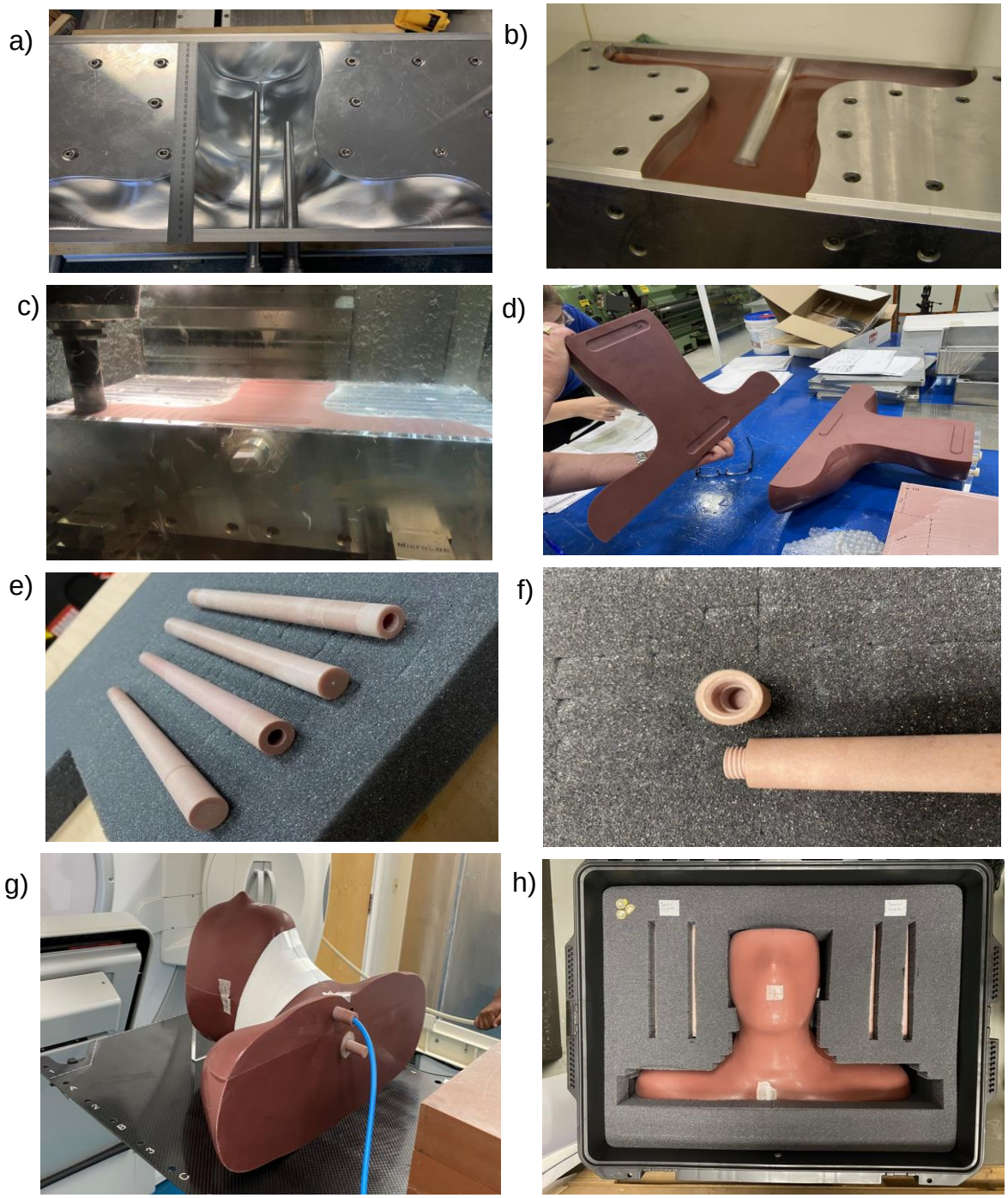

Figure 4.3 *Manufacture of phantom: a) Phantom Mould, b) Filling of mould, c) CNC milling of phantom d) Building of phantom., e) Detector holders (from left to right: Alanine holder for tumour region, ionisation chamber holder for tumour region, Alanine holder for spinal region, ionisation chamber holder for spinal region.) f) Screw cap of alanine holder for tumour region, g) Preliminary testing of phantom at NPL, h) Phantom ready for onsite proton centre visits.*

4.2.4. Initial testing

Once the phantom was constructed, it was scanned at NPL with the Mediso Any Scan. A typical phantom protocol was used to CT image the phantom: axial scan, 1.25 mm slices, 120 kVp, 300 mA tube voltage and abdomen reconstruction. The phantom was scanned with and without the weight variation shell. Dummy alanine pellets and film were also added in the phantom for the CT scan. Using the CT image, a primary and secondary clinical target volume (CTV) contour and OAR regions were registered onto the image for planning of the treatment. The phantom contours were based on anonymous patient contours and tailored to the shape of the simplified phantom geometry by an experienced clinical medical physicist. Initial testing was completed at NPL in a conventional megavoltage linear accelerator (Appendices, section E), before the phantom was used as part of a pilot proton audit study.

The CT image taken at NPL was then sent to the clinical centres before the pilot audit visit for the planning stage of the phantom to begin before arrival on site.

4.2.5. Pilot audit study

Measurements were performed at two protons centres within the U.K, labelled as Centre A and B throughout this work to anonymise the centres. Both centres are equipped with the Varian ProBeam proton therapy system.

4.2.5.1. CT scans

The phantom was scanned with each centre's clinical CT scanners following the centre's typically head and neck protocol: 2 mm slice thickness, 120 kVp, variable current, head reconstruction. The head plate was left on the phantom and positioned against a treatment bed index bar to ensure repeatable setup on the treatment couch.

The phantom was aligned to laser alignment markers and ball bearings were added to the surface of the phantom.

4.2.5.2. Treatment planning

The phantom was planned by clinical staff at both centres using their typical head and neck protocol, as well as following the clinical requirements of the TORPEdO planning protocol (Figure 4.4).

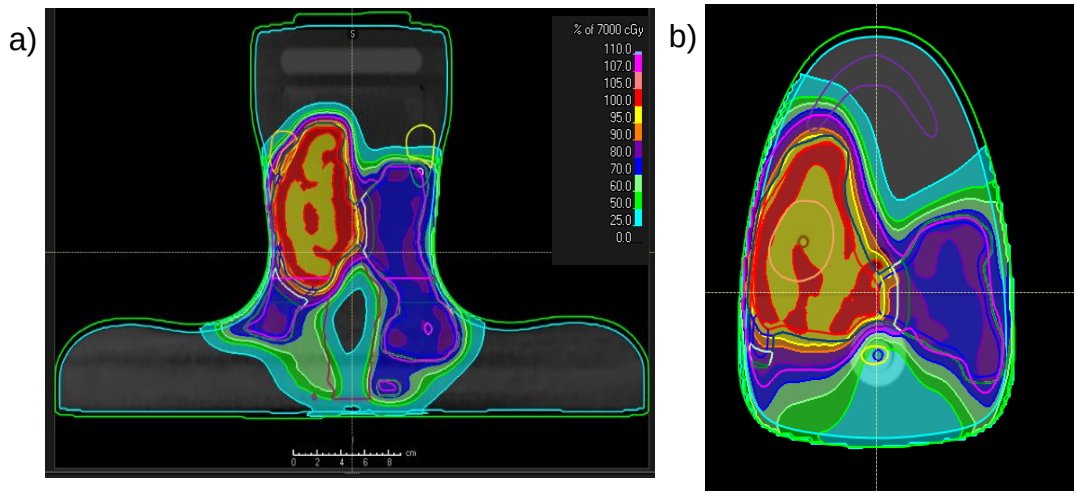

Figure 4.4 *Example of dose distribution within phantom (a) Coronal plane at location of radiochromic film (b) Axial plane at the location of alanine pellets or ionisation chamber*

Centre A and B used Varian Eclipse v16.1 with clinical dose calculation algorithm PCS version 15.6.05 and 16.1.0 respectively. The dose grid resolution of the plans were 2.5 mm. Both centres planned the treatment with a prescribed dose of 63.6 Gy in 33 fractions. Both centres used 3% ± 3 mm range uncertainty parameters. The OARs were kept to acceptable dose constraints. The right parotoid did receive a relatively higher dose compared to the left parotoid due to clinical protocols weighting greater importance to oral cavity dose sparing. The differences in the treatment planning and delivery details between the centres can be seen in Table 4.1.

Table 4.1 *Treatment planning details. CTVp = Primary clinical target volume, CTVn = Nodal clinical target volume, $D_{98\%}$= minimal dose to 98% of the target volume and $D_{0.1\%}$= maximal dose to 0.1% of the spinal cord region.*

Treatment planning and delivery details	Centre A	Centre B
Number of fields	4	5
Field angles (°)	0, 45 180, 315	0, 45, 100, 250, 315
Number of robust planning scenarios	14	8
$D_{98\%}$ CTVp (Gy)	62.5	62.0
$D_{98\%}$ CTVn (Gy)	49.4	50.2
Max dose to spinal cord $D_{0.1\%}$ (Gy)	38.9	35.6
Mean dose to parotid (L) (Gy)	25.2	18.6
Mean dose to parotid (R) (Gy)	46.8	53.5

The phantom was placed in the supine position and aligned with the gantry lasers and kV pair and Cone beam CT (CBCT) imaging. The imaging parameters used for the setup were the same as those recommended for patients.

4.2.5.3. Detector measurements

Measurements were performed with either two ionisation chambers or with the combination of alanine and film. Absolute dose measurements were taken by an ionisation chamber or alanine pellets in the CTV and OAR regions while the relative dose distribution was provided by film. All uncertainties in this work are reported at a confidence interval of 68%. All ionisation chamber and alanine measurements were corrected for daily output variations by assessing the relative difference between a PTW-Roos ionisation chamber output measurement to TPS calculated values for a single layer of 220 MeV at 2 cm water-equivalent depth delivering 10 MU per spot. Figure 4.5 shows the detector positions within the phantom relative to the primary and secondary clinical target volume, brainstem, spinal cord, and parotid gland contours.

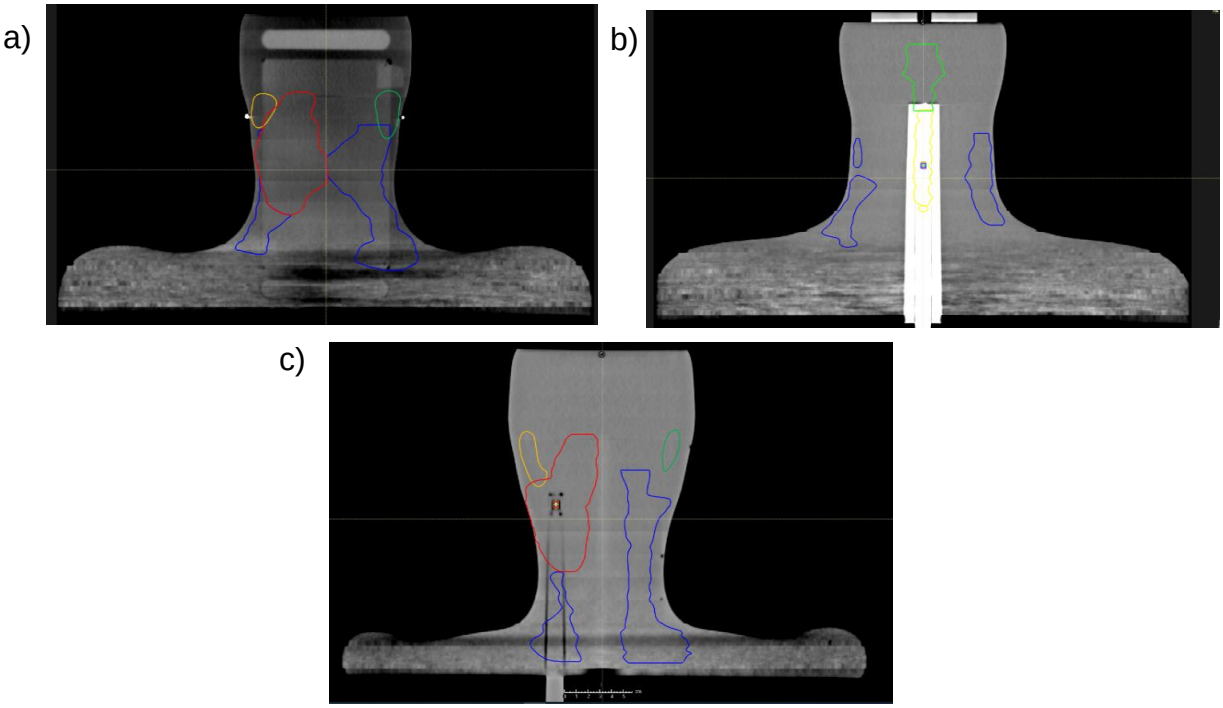

Figure 4.5 *Coronal plane sections showing detector positions with the phantom. a) Film position, b) Alanine or ionisation chamber in spinal cord OAR c) Alanine or ionisation chamber in the CTV. For measurements with detectors within the CTV and spinal cord OAR, either 3 alanine detectors or the sensitive volume of the ionisation chamber were at equivalent positions in the phantom.*

4.2.5.3. Ionisation chamber measurements

4.2.5.3.1. Daily output measurements

Firstly, reference measurements were performed with a secondary standard PTW-Roos Type 34001 ionisation chamber in a 220 MeV single layer of 10 cm x 10 cm with 0.25 cm spot spacing and delivering around 0.5 Gy (10 MU per spot) at a depth of 2 cm in solid water (RW3). The reference point of the detector was positioned at the isocentre. The absolute dose value was then compared to the TPS to provide a daily beam output correction for the machine. The Semiflex chamber used within the phantom was then cross-calibrated against the secondary standard Roos chamber at 2 cm depth with the 220 MeV reference field for scaled MU to deliver around 2 Gy to each chamber. The chamber was cross calibrated at 2 Gy as this was approximate dose level of a single fraction of the head and neck plan. An operating voltage of -400

V was applied to the Semiflex chamber while -200 V was applied to the Roos chamber. Ion recombination and polarity correction factors were assessed for both ionisation chambers.

4.2.5.3.2. Head and Neck Plan Irradiation

Ionisation chamber holders were designed to enable the insertion of PTW Semiflex Type 31010 ionisation chambers within the phantom. The ionisation chamber can be operated in relatively small field sizes (field size range 3 – 40 cm^2) which are required for accurate dose measurements within the tumour region of the phantom. For the head and neck phantom measurements, a single fraction was initially delivered to the phantom with the ionisation chamber within the CTV region. The chamber was then moved to the spinal OAR and the single fraction irradiation repeated. At Centre A, the experimental time allocated allowed for testing the impact of the weight variation shell on the dose within the CTV. The single fraction irradiation was repeated for the ionisation chamber in the CTV when the weight gain shell was added to the phantom. The absorbed dose to water was derived using the formalisation of the IAEA TRS-398 code of practice [21] and beam quality correction factors from either IAEA TRS-398 or from Palmans et al. (2022) [166]. The corrected ionisation chamber dose measurements were then compared to the TPS predicted dose. For point dose measurements (ionisation chamber and alanine) within the spinal cord, the relative difference was also normalised to the spinal cord tolerance for the number of fractions delivered. From the TORPEdO trial, a value of 43.6 Gy for 33 fractions was considered [157]. This was calculated due to the OAR region being in a steeper dose gradient region compared to the CTV region.

4.2.5.4. Alanine measurements

Unlike ionisation chambers, the dose response of alanine depends on the charge, the fluence and the energy of the particles within the radiation field. Correction factors are required for absolute dose measurements with alanine. The alanine pellets used for the phantom had a nominal diameter of 5.0 mm and a thickness of 2.4 mm. The alanine pellets were read out at NPL, and the pellet corrected with a cross-calibration and quenching factor (or relative effectiveness (RE) correction).

4.2.5.4.1. Cross-calibration of alanine

This work aimed to replicate the cross-calibration method proposed by Palmans et al. (2018) [71] with a Roos chamber instead of Farmer chamber, because the Roos chamber is the recommended chamber of the upcoming IPEM code of practice for proton dosimetry [167]. The cross-calibration of alanine was performed via the substitution method in RW3 solid water slabs. 9 alanine pellets were irradiated within a farmer type holder. Both detectors, positioned at the clinical reference depth of 2 cm water-equivalent depth, were alternately irradiated in a single-layer scanned field of size 10 cm × 10 cm, nominal energy 220 MeV delivering around 10 Gy. A high energy of 220 MeV was chosen to provide a minimal energy spread of the beam.

Dose to water was derived from the ionisation chamber measurement as [21]:

$$D_{w,Q_{\mathrm{cross}}}^{IC} = M_{Q_{\mathrm{cross}}}^{\mathrm{IC}} N_{D,w,Q_0}^{\mathrm{IC}} k_{Q_{\mathrm{cross}},Q_0}^{\mathrm{IC}} \quad (4.1)$$

where Q_{cross} is the beam quality at reference depth, $N_{\mathrm{D,w},Q_0}^{\mathrm{IC}}$ is the absorbed dose to water calibration coefficient of the ionisation chamber in the calibration beam quality Q_0, $M_{Q_{\mathrm{cross}}}^{\mathrm{IC}}$ is the ionisation chamber reading corrected for pressure, temperature,

polarity effects and ion recombination, and $k^{\mathrm{IC}}_{Q_{\mathrm{cross}},Q_0}$ is the beam quality correction factor for the ionisation in the cross calibration beam quality with respect to the calibration beam quality. The tabulated $k^{\mathrm{IC}}_{Q_{\mathrm{cross}},Q_0}$ values from the IAEA TRS-398 code of practice were used [21] as well as updated beam quality values recently published by Palmans et al. (2022) [166].

A similar equation can be defined for alanine [71]:

$$D^{\mathrm{Alanine}}_{\mathrm{w},Q_{\mathrm{cross}}} = M^{\mathrm{Alanine}}_{Q_{\mathrm{cross}}} N^{\mathrm{Alanine}}_{\mathrm{D,w},Q_0} k^{\mathrm{Alanine}}_{Q_{\mathrm{cross}},Q_0} \quad (4.2)$$

where the product $M^{\mathrm{Alanine}}_{Q_{\mathrm{cross}}} N^{\mathrm{Alanine}}_{\mathrm{D,w},Q_0}$ is the value that NPL provides as a ^{60}Co-reference value of absorbed dose to water by reading out the irradiated pellet. $k^{\mathrm{Alanine}}_{Q_{\mathrm{cross}},Q_0}$ is the beam quality factor which can be derived from the cross-calibration method, using the condition that $D^{\mathrm{IC}}_{\mathrm{w},Q_{\mathrm{cross}}} = D^{\mathrm{Alanine}}_{\mathrm{w},Q_{\mathrm{cross}}}$:

$$k^{\mathrm{Alanine}}_{Q_{\mathrm{cross}},Q_0} = \frac{M^{\mathrm{IC}}_{Q_{\mathrm{cross}}} N^{\mathrm{IC}}_{\mathrm{D,w},Q_0} k^{\mathrm{IC}}_{Q_{\mathrm{cross}},Q_0}}{M^{\mathrm{Alanine}}_{Q_{\mathrm{cross}}} N^{\mathrm{Alanine}}_{\mathrm{D,w},Q_0}} \quad (4.3)$$

4.2.5.4.2. Relative effectiveness calculation for alanine

The method for calculation of the RE of alanine's dose response descried by Carlino et al. (2018) was applied in this work [37]. Raystation (version 10B ion) was used to determine the energy spectra of primary and secondary protons in the radiation field as a dose weighted average of the relative effectiveness, $\eta_{\mathrm{aln}}(E_i, Z_i)$, for each ion type. For each beam, the alanine dose weighted average RE, $\bar{\eta}_{\mathrm{aln,Plan}}$, was scored in each voxel of the dose grid (1 × 1 × 1 mm^3) within 0.5% uncertainty using the Monte Carlo algorithm. The alanine pellets were contoured from the CT scan and an average RE determined for each pellet from the dose weighed RE values.

The RE was determined by Raystation for both the cross-calibration setup and head and neck plan. Given the mass electronic stopping power ratio water to alanine and perturbation correct factors is almost independent of proton beam quality. The RE correction factor was determined as:

$$k_{\mathrm{Plan},\,Q_{cross}}^{Alanine} \approx \frac{\bar{\eta}_{\mathrm{aln},Q_{\mathrm{cross}}}}{\bar{\eta}_{\mathrm{aln,Plan}}} \tag{4.4}$$

4.2.5.4.3. Head and neck irradiation

For the head and neck phantom irradiation, 5 fractions of the treatment were delivered to the phantom with 3 alanine pellets detectors within the CTV and spinal OAR. Five fractions were delivered to ensure the alanine in the CTV received a dose level close to 10 Gy for reduced measurement uncertainty.

The absorbed dose to water for alanine was calculated by Equation 4.5 [71]:

$$D_{\mathrm{w,Plan}}^{\mathrm{Alanine}} = M_{\mathrm{Plan}}^{\mathrm{Alanine}} N_{\mathrm{D,w},Q_0}^{\mathrm{Alanine}} k_{Q_{\mathrm{cross}},Q_0}^{\mathrm{Alanine}}\, k_{\mathrm{Plan},\,Q_{cross}}^{Alanine} \tag{4.5}$$

where $M_{\mathrm{Plan}}^{\mathrm{Alanine}} N_{\mathrm{D,w},Q_0}^{\mathrm{Alanine}}$ is what NPL provides as the ^{60}Co-reference value of absorbed dose for the pellet, $k_{Q_{\mathrm{cross}},Q_0}^{\mathrm{Alanine}}$ is the value derived from the cross-calibration process and $k_{\mathrm{Plan},\,Q_{cross}}^{Alanine}$ is derived from the ratio of dose weighted average RE for the cross-calibration delivery compared to the treatment plan delivery from Raystation. The corrected pellet doses were then compared to the predicted TPS dose.

4.2.5.5. Film measurements

All EBT3 films were handled following radiochromic film guidelines and best procedures [105,106]. EBT3 films were scanned after 48 hours on an EPSON Expression 10000XL and film analysis was carried out with an in-house NPL software

called Vigo (version 2.0.0) [168] with the green channel. The green channel has been shown to be more sensitive than the red channel for doses over 6 Gy [108].

4.2.5.5.1. Film reference check

At Centre A, four 3.5 cm x 4 cm reference pieces from the same EBT3 sheet as the piece used in the PRuDeNCE phantom, were irradiated in a 220 MeV, 10 cm x 10 cm single layer field with 0.25 cm spot spacing, positioned at 2 cm depth in local solid water (RW3). A PTW-Roos chamber was positioned directly underneath the film to record the dose delivered to each film. The MU of the delivery were scaled to provide the following dose levels, 0, 2, 6.5, 10 and 12 Gy. Due to time constraints, only a 10 Gy irradiation was performed at Centre B. An additional unirradiated 3.5 cm x 4 cm film piece was kept as background. During the analysis, a central 1.0 cm square region of interest was used for the determination of average optical density of the film piece. The dose from the calibration films were compared to the batch calibration (3^{rd} order polynominal fit) to ensure the batch calibration provided a good fit for the calibration of the film measurement sheet.

4.2.5.5.2. Head and neck irradiation

For the head and neck phantom irradiation, 5 fractions of the treatment were delivered to the phantom with EBT3 film positioned coronally alongside with the alanine pellets in the CTV and OAR regions. During analysis, auto alignment was used to adjust for possible minor disagreement in position between the film and TPS. The film measurements were used to evaluate the dose homogeneity and distribution throughout the phantom. The film dose distribution showed a general under response across the distribution owing to film quenching, therefore, to correct for this the film

dose was upscaled. The film was upscaled by the relative difference between the average dose of the film within the CTV region (90-100% dose threshold cut from film dose map) by either the average corrected alanine pellet dose or TPS dose value within the CTV region. The film was scaled by the TPS as a comparison to alanine results due to alanine measurements showing a small systematic under response compared to ionisation chamber measurements (as will be shown in the results section below). Raystation (version 11B ion) was also used to determine the dose-averaged linear energy transfer (LETd) maps for each clinical plan. This was calculated to provide further information on the of quenching occurring within the film region.

Gamma index analysis was performed to compare the dose distribution between the film (reference dose distribution) and the predicted TPS dose distribution (considered as the evaluation dose distribution) [169]. Gamma analysis is a mathematical technique to calculate a dimensionless metric, known as gamma index. The gamma index is determined by combining the dose difference and distance difference for each point of the evaluated dose distribution to a reference dose distribution [168,169]. The gamma analysis can determine either a global or local gamma index. For the local, the gamma index gives the absolute difference between local dose difference between the evaluation and reference dose distribution. For global, the local dose differences is divided by a normalised dose value. This normalisation value can be any dose value, typically the average dose within the high dose gradient region is used. The choice of the type of gamma analysis depends on what is being considered, for example, global analysis can provide an understanding of errors in higher dose regions while local analysis will highlight failure in either high

or low dose gradient regions. The gamma analysis is typically reported as the percentage of points that achieve the gamma index pass rate. The pass rate criteria is dependent on the clinical site and dose planning constraints. For this work a series of pass rates for both local and global gamma index were considered.

4.3. Results

4.3.1. Proton tissue-equivalent materials

Table 4.2 shows the average mass density, RSP and HU for the weight shell material sample slabs, as well as their relative differences to their target tissues. The material properties of VC#2 and MS#6 have been previously reported in Chapter 3. It should be noted the density of weight-variation shell was also measured directly; 1.014 g/cm^3 for the right-hand side of phantom neck and 1.002 g/cm^3 for the left-hand side of neck phantom. This is due to the variability in material production.

Table 4.2 Average mass density, RSP and HU for the phantom materials test slabs. Weigh-variation shell was compared against water as its target tissue. Location of CT scanning NPL (*) and UCLH (**).

Material	Weight shell (CB PA12)
Average mass density (SD)	1.00 (0.02)
Average relative difference to target tissue (SD) (%)	1.35 (0.84)
Average RSP (SD)	1.00 (0.04)
Average relative difference to target tissue (SD)	2.78 (1.22)
Average HU (120 kVp) (SD)*	13 (29)
Predicted RSP (SD)	1.02 (0.02)
Average relative difference to experimental RSP (SD) (%)	2.42 (1.52)
Average HU (dual energy 120 kVp) (SD)**	4 (28)
Predicted RSP (SD)	1.01 (0.02)
Average relative difference to experimental RSP (SD) (%)	1.35 (1.93)

4.3.2. Pilot audit study

4.3.2.1. Ionisation chamber measurements

4.3.2.1.1. Daily output measurements

Table 4.3 shows agreement between the PTW-Roos chamber and the TPS values. The chamber dose was calculated considering the IAEA TRS-398 tabulated beam quality values as well as current best estimates for beam quality values published in Palmans et al. (2022) [166].

Table 4.3 *Reference output measurements of Roos chamber at 220 MeV*

Centre	Roos chamber		Nominal Value (Gy)	% Difference	
	TRS-398 (Gy)	Palmans et al. (2022) (Gy)		TRS-398	Palmans et al. (2022)
A	0.563	0.560	0.558	0.9	0.4
B	0.553	0.551	0.552	0.2	-0.2

4.3.2.1.2. Head and neck phantom measurements

Table 4.4 shows the Semiflex chamber dose results positioned at the CTV and OAR considering IAEA TRS-398 and Palmans et al. (2022) beam quality values as well as their comparison to TPS predictions for dose. The ratio between the ionisation chamber measurement in the CTV without and with the weight-variation shell was 0.991 at Centre A.

Table 4.4 *Head and neck phantom measurements with Semiflex ionisation chamber. For the spinal OAR chamber reading, the absolute difference between chamber and TPS and relative % difference normalised to the normal tolerance dose for the spinal cord for the number of fractions delivered (48 Gy RBE) also calculated respectively.*

Centre	Location	k_{Q_{Plan},Q_0}^{IC} value	Measured (Gy)	Daily output Corrected (Gy)	TPS (Gy)	Relative difference (output corrected) to TPS (%)	Absolute difference to TPS (Gy)	Difference relative to 1.32 Gy (%)
A	CTV	TRS-398	1.976	1.959	1.927	1.66	N/A	N/A
		Palmans et al. (2022)	1.966	1.958	1.927	1.63	N/A	N/A
	OAR	TRS-398	0.858	0.851	0.863	-1.38	-0.01	-0.90
		Palmans et al. (2022)	0.855	0.851	0.863	-1.33	-0.01	-0.87
B	CTV	TRS-398	1.963	1.959	1.924	1.83	N/A	N/A
		Palmans et al. (2022)	1.952	1.957	1.924	1.74	N/A	N/A
	OAR	TRS-398	0.951	0.949	0.669	41.23	0.28	20.94
		Palmans et al. (2022)	0.946	0.948	0.669	41.08	0.28	20.87

4.3.2.2. Alanine measurements

4.3.2.2.1. Cross calibration measurements

Table 4.5 and Table 4.6 shows the cross-calibration factors for alanine in Centre A and B, respectively.

Table 4.5 *Cross-calibration factor for alanine in Centre A proton beam at 220 MeV.*

Alanine Dosimeter Number	$M_{Q_{cross}}^{\text{Alanine}} N_{\text{D,w},Q_0}^{\text{Alanine}}$	$k_{Q_{\text{cross}},Q_0}^{Alanine}$ TRS-398	$k_{Q_{\text{cross}},Q_0}^{Alanine}$ Palmans et al. (2022)
78/873.1	10.017	1.012	1.013
78/873.2	9.977	1.016	1.017
78/873.3	9.988	1.015	1.015
78/873.4	9.977	1.016	1.017
78/873.5	9.930	1.021	1.021
78/873.6	9.954	1.018	1.019
78/873.7	9.989	1.015	1.015
78/873.8	9.957	1.018	1.019
78/873.9	9.951	1.019	1.019
Average	9.971	1.017	1.012
SD	0.026	0.003	0.003

Table 4.6 *Cross-calibration factor for alanine in Centre B proton beam at 220 MeV.*

Alanine Dosimeter Number	$M_{Q_{cross}}^{\text{Alanine}} N_{\text{D,w},Q_0}^{\text{Alanine}}$	$k_{Q_{\text{cross}},Q_0}^{Alanine}$ TRS-398	$k_{Q_{\text{cross}},Q_0}^{Alanine}$ Palmans et al. (2022)
78/1345.1	9.849	1.020	1.016
78/1345.2	9.881	1.017	1.013
78/1345.3	9.895	1.016	1.011
78/1345.4	9.934	1.012	1.007
78/1345.5	9.874	1.018	1.014
78/1345.6	9.910	1.014	1.010
78/1345.7	9.839	1.022	1.017
78/1345.8	9.839	1.022	1.017
78/1345.9	9.948	1.010	1.006
Average	9.885	1.017	1.012
SD	0.040	0.003	0.004

4.3.2.2.2. Head and neck phantom measurements

Table 4.7 and Table 4.8 shows the alanine measurements at the CTV and OAR considering the tabulated beam quality values from IAEA TRS-398 for the measurements acquired Centre A and B, respectively, as well as their comparison against TPS predictions for dose. Note that in the tables, results using Palmans et al. (2022) values are not shown for simplicity as the results using IAEA TRS-398 and Palmans et al. (2022) data were within the standard deviation of the measurement.

Table 4.7 : *Alanine results for Centre A.*

Location	Alanine Dosimeter Number	$M_{\text{Plan}}^{\text{Alanine}} N_{\text{D,w},Q_0}^{\text{Alanine}}$ (Gy)	$k_{Q_{\text{cross}},Q_0}^{Alanine}$	$k_{\text{Plan},Q_{cross}}^{Alanine}$	Corrections Applied (Gy)	Daily output corrected (Gy)	TPS (Gy)	Relative difference (output corrected) (TPS) (%)		
CTV	**78/875.1**	9.371	1.017	1.005	9.575	9.492	9.617	-1.30		
	78/876.1	9.319	1.017	1.005	9.522	9.440	9.640	-2.08		
	78/877.1	9.344	1.017	1.005	9.548	9.465	9.641	-1.83		
Mean of all pellets (SD)		9.345 (0.03)	1.017 (<0.01)	1.005 (<0.01)	9.552 (0.03)	9.466 (0.03)	9.632 (0.02)	-1.74 (0.40)		
Location	**Alanine Dosimeter Number**	$M_{Q_{\text{cross}}}^{\text{Alanine}} N_{\text{D,w},Q_0}^{\text{Alanine}}$ (Gy)	$k_{Q_{\text{cross}},Q_0}^{Alanine}$	$k_{\text{Plan},Q_{cross}}^{Alanine}$	**Corrections Applied (Gy)**	**Daily output corrected (Gy)**	**TPS (Gy)**	**Relative difference (output corrected) (TPS) (%)**	**Absolute difference (Gy)**	**Difference relative to 6.61 Gy (%)**
OAR	**78/878.1**	4.096	1.017	1.003	4.177	4.141	4.291	-3.50	-0.15	-2.27
	78/879.1	4.078	1.017	1.003	4.158	4.122	4.311	-4.38	-0.19	-2.85
	78/880.1	4.122	1.017	1.002	4.199	4.163	4.332	-3.91	-0.17	-2.56
Mean of all pellets		4.099 (0.02)	1.017 (<0.01)	1.001 (<0.01)	4.178 (0.02)	4.142 (0.02)	4.311 (0.02)	-3.93 (0.44)	-0.17 (0.02)	-2.56 (0.29)

Table 4.8 *Alanine results for Centre B.*

Location	**Alanine Dosimeter Number**	$M_{\mathrm{Plan}}^{\mathrm{Alanine}} N_{\mathrm{D,w},Q_0}^{\mathrm{Alanin}}$ **(Gy)**	$k_{Q_{\mathrm{cross}},Q_0}^{Alanine}$	$k_{\mathrm{Plan},Q_{cross}}^{Alanine}$	**Corrections Applied (Gy)**	**Daily output corrected (Gy)**	**TPS (Gy)**	**Relative difference (output corrected) (TPS) (%)**		
CTV	**78/1347.1**	9.427	1.017	1.001	9.594	9.577	9.610	-0.35		
	78/1348.1	9.378	1.017	1.001	9.545	9.527	9.620	-0.97		
	78/1349.1	9.529	1.017	1.001	9.698	9.680	9.634	0.47		
Mean of all pellets (SD)		9.445 (0.08)	1.017 (<0.01)	1.002 (<0.01)	9.612 (0.08)	9.595 (0.08)	9.622 (0.01)	-0.28 (0.73)		
Location	**Alanine Dosimeter Number**	$M_{Q_{Plan}}^{\mathrm{Alanine}} N_{\mathrm{D,w},Q_0}^{\mathrm{Alanin}}$ **(Gy)**	$k_{Q_{\mathrm{cross}},Q_0}^{Alanine}$	$k_{\mathrm{Plan},Q_{cross}}^{Alanine}$	**Corrections Applied (Gy)**	**Daily output corrected (Gy)**	**TPS (Gy)**	**Relative difference (output corrected) (TPS) (%)**	**Absolute difference to TPS (Gy)**	**Difference relative to 6.61 Gy (%)**
OAR	**78/1350.1**	3.865	1.017	1.044	4.103	4.103	3.446	18.86	0.65	9.83
	78/1351.1	3.548	1.017	1.043	3.763	3.763	3.256	15.35	0.50	7.56
	78/1352.1	3.180	1.017	1.043	3.372	3.372	3.124	7.74	0.24	3.66
Mean of all pellets		3.531 (0.34)	1.017 (<0.01)	1.043 (<0.01)	3.742 (0.36)	3.734 (0.36)	3.275 (0.16)	13.98 (5.68)	0.46 (0.20)	7.02 (3.12)

4.3.2.3. Film measurements

The reference dose analysis showed the agreement between the 10 Gy calibration film and the film batch calibration was within 1.5% for the green channel at Centre A. The film dose distribution was upscaled by either relative difference to the corrected alanine or TPS values. Comparing alanine to film, a 5.4% upscaling of dose was applied to the film map. While when comparing film to TPS, an 6.9% upscaling of dose was applied to film map. Table 4.9 shows the gamma index results for the film irradiation at Centre A when comparing the upscaled dose film distribution against TPS values. Figure 4.6 shows the gamma maps for film at 3%/ 3 mm for alanine and TPS scaled film.

Table 4.9 *Film analysis for Centre A – Global and local analysis with a dose normalisation of 9.64 Gy with dose threshold set to 20-100%.*

Dose scaling method	**Gamma pass rate (Global)**					**Gamma pass rate (Local)**				
	3%/2 mm	**3%/3 mm**	**4%/3 mm**	**5%/3 mm**	**5%/2 mm**	**3%/2 mm**	**3% 3 mm**	**4%/3 mm**	**5%/3 mm**	**5 %/2 mm**
Alanine	90.67	92.90	98.21	99.73	99.27	87.45	90.86	96.59	99.17	98.11
TPS	90.99	93.84	98.61	99.82	99.59	85.66	90.74	96.31	98.87	97.75

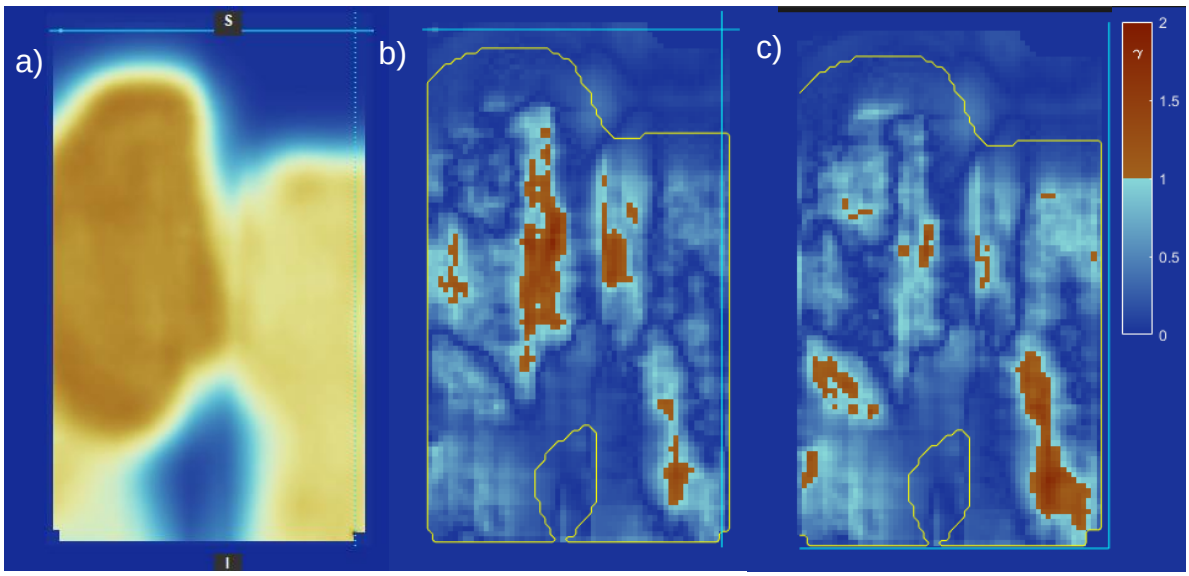

Figure 4.6 *a) Film dose map, Gamma maps (global) b) 3 % / 3 mm for alanine scaled film vs. TPS c) 3 % / 3 mm for TPS scaled film vs.TPS for Centre A*

The reference dose analysis showed the agreement between the 10 Gy calibration film and the film batch calibration was within 3.4% for the green channel at Centre B. The film dose distribution was upscaled by either relative difference to the corrected alanine or TPS values. Comparing alanine to film, a 7.3% upscaling of dose was applied to film map. While when comparing film to TPS, an 7.7% upscaling of dose was applied to film map. Table 4.10 shows the gamma index results for the film irradiation at Centre A when comparing the upscaled dose film distribution against TPS values Figure 4.7 shows the gamma maps for film at 3%/3 mm for alanine and TPS scaled film.

Table 4.10 *Film analysis for Centre B – Global and local analysis with a dose normalisation of 9.64 Gy with dose threshold set to 20-100%.*

Dose scaling method	Gamma pass rate (Global)					Gamma pass rate (Local)				
	3%/2 mm	3%/3 mm	4%/3 mm	5%/3 mm	5%/2 mm	3%/2 mm	3% 3 mm	4%/3 mm	5%/3 mm	5 %/2 mm
Alanine	94.80	95.96	98.68	99.82	99.72	91.01	93.63	98.71	99.92	99.75
TPS	90.10	93.10	97.90	99.45	99.38	85.74	89.53	97.69	99.58	99.32

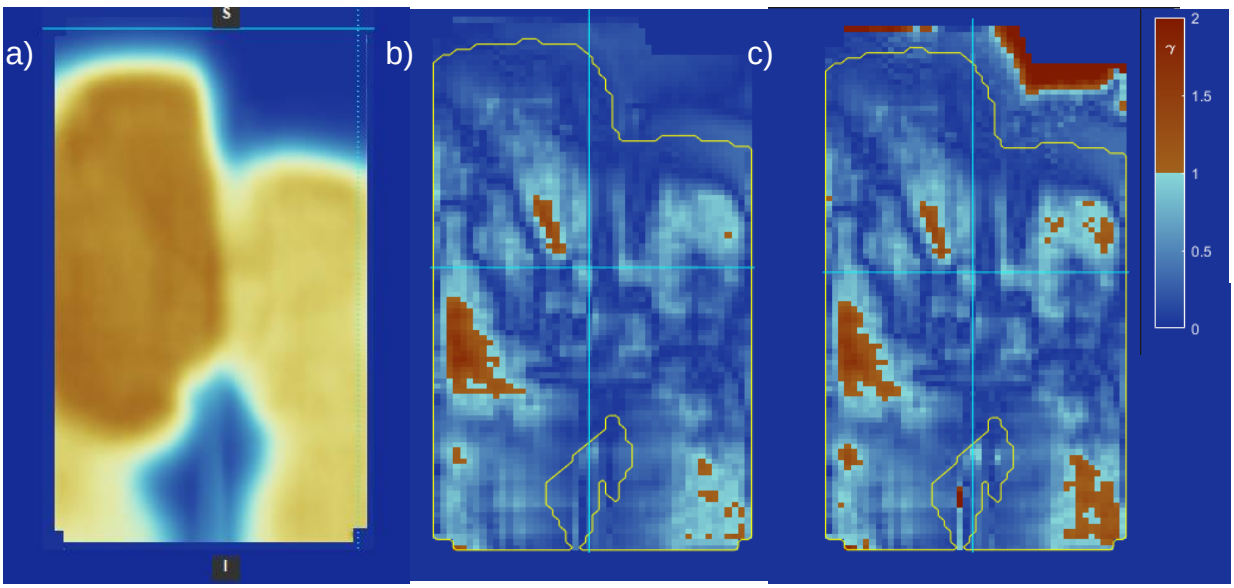

Figure 4.7 *a) Film dose map, Gamma maps (global) b) 3 %/ 3 mm for alanine scaled film vs. TPS c) 3%/ 3 mm for TPS vs. TPS scaled film for Centre B.*

4.3.1.1. Linear Energy Transfer maps

Figures 4.8 a) and b) show the dose-averaged linear energy transfer maps for the clinical plan calculated in Raystation (version 11B ion) in the coronal plane at the position of the film and axial plane at the position of the alanine or Semiflex detectors for Centre A and B plans, respectively.

a)

b)

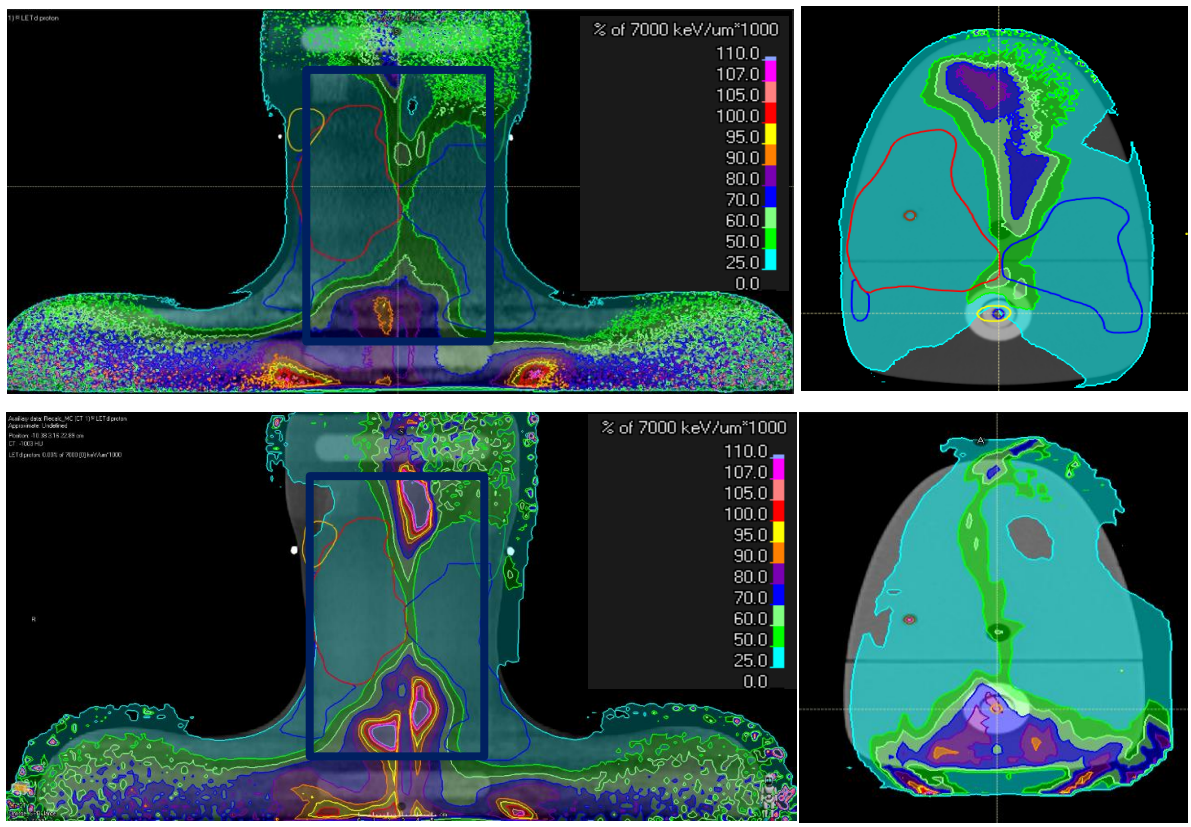

Figure 4.8 *Linear energy transfer maps in phantom a) Centre A (Coronal and Axial plane) b) Centre B (Coronal and Axial Plane). Blue box on coronal plane images shows the film position within the phantom.*

4.4. Discussion

During this work, an anthropomorphic head and neck phantom was successfully designed, built, and used in a pilot study for oropharyngeal cancer at two U.K. based proton centres.

The absolute dose measurements with the Semiflex chamber and alanine results showed good agreement within 2 % with TPS values at the CTV for both centres (Table 4.4). The dose measured in the phantom by the ionisation chamber were higher than TPS predictions in the CTV. For Centre A measurements, the absolute dose measurement with the Semiflex chamber and alanine showed good agreement with the 2 and 4 % with TPS in the OAR region respectively. However, for Centre B, the OAR measurements with the chamber and alanine were shown to be significantly larger than the TPS predictions.

From reviewing Centre B's treatment plan, the clinical plan was shown to conform the beam to significantly reduce the dose to the spinal region which resulted in a steep dose gradient in the detector region. Research has highlighted that for cylindrical chambers in proton beams the effective point of measurement can be shifted in the direction of the beam direction. IAEA TRS-398 suggest a $0.75 \cdot r_{cyl}$ shift to effective point of measurement for cylindrical chambers in steep dose gradients where r_{cyl} is the radius of the cylinder. Work by Barna et al. (2022) has highlighted for the PTW Semiflex 31010 chamber in water the shift is more significant ($0.92 \cdot r_{cyl}$). The impact of the effective point of measurement shift was investigated in Raystation and a 2.5 mm shift (equivalent to $0.92 \cdot r_{cyl}$ for the PTW-Semiflex in water) impacted the dose prediction by around 40% when compared to the central dose prediction. This effective point of measurement shift therefore can explain the overresponse of the chamber compared to TPS predictions seen at Centre B. It should be noted due to measurement being within a high-density bone-equivalent material the effective point of measurement could be greater than the shift calculated by Barna et al. (2022) in water. Further work could look to investigate the impact of the phantom materials on

the effective point of measurement of the PTW-Semiflex chamber within the phantom. These results highlight the challenge of measuring in OAR regions which can have steep dose drop off with absolute dose detectors, such as ionisation chambers and alanine. Future phantoms designs should look to use detector such as film for OAR regions where the dose drop off is likely to be steep.

In this study, the cross-calibration factors values using the IAEA TRS-398 taken at the centres were shown to agree to the NPL report IR 48 values within uncertainties. The alanine dose measurements underestimated the dose by 2-3% compared to the ionisation chamber within the CTV. The overall uncertainties of the two dosimetric detectors are 2% for the ionisation chamber and 3% for alanine. The difference in the dose determined by both detectors suggest more factors may be required or current factors need better quantification for the derivation of dose to water in the phantom. This includes determination of factors such as the RE correction, the water-to-alanine stopping power ratio and perturbation factors for alanine pellets in proton beams. The determination of dose from ionisation chambers is dominated by uncertainties on the beam quality correction factor as well as a large influence of local dose gradients. This work investigated the effect of using the recommended values in IAEA TRS-398 and those recently published in Palmans et al. (2022) and both had comparable results. Further experimental and Monte Carlo work in a proton beam is necessary to gain confidence on the correction factors used in this work, in particular derivation of the RE factor in Raystation and perturbation factors of alanine by Monte Carlo simulations.

The film was evaluated as a combination of the pass-rate and critical review of the film and TPS profile comparisons through failing gamma map regions. For the pass rate results from both facilities showed a >90 % and > 95 % pass rate for the gamma

criterions of 3 %/3 mm and 4 %/3 mm (global) respectively. These results are indicative with what is seen for gamma analysis in radiotherapy [72,80] . An average dose scaling was applied to the full film dose map to correct for quenching effects, nevertheless, the film was shown to have failed gamma regions (Figure 4.6 b) and c) and 4.7 b) and c)). Due to the variety of factors which impact film, such as inherent film analysis uncertainties, film dose rescaling uncertainties and impact of film quenching, it is difficult to interpret the failed gamma regions. Absolute dose output measurements with the ionisation chamber and alanine pellets in the CTV and OAR regions give indication there was no delivery error.

For this study, both an alanine and TPS rescaling value were considered to reduce the impact of film quenching. For Centre A, the gamma index results (Table 4.9) were comparable when rescaling against the TPS as opposed to the results obtained using alanine. For Centre B, the gamma index pass rates (Table 4.10) were lower for the TPS rescaled film when compared to alanine, particularly for the stricter pass rate criteria, even though the dose scaling values showed better agreement (within 0.5%) to each other in comparison to Centre A (1.5%). In addition, the LET maps (Figure 4.8) highlight the range of LET within each clinical plan. As a result, uncertainty should be attributed to film quenching being LET dependent [170]. This highlights that the use of an average scaling factor may not be a suitable method to provide an accurate dose comparison. Due to this limitation, the film analysis was performed as a relative dose comparison for this study. Further work could investigate RE corrections of the film by applying a dose-average LET correction map [170] instead of an average dose rescaling technique.

Due to experimental time constraints, the impact of the weight-variation shell was only briefly tested as part of this work. Ionisation chamber results showed a reduction of dose to the CTV of less than 1.0 % between the two setups (with or without weight-variation shell). This suggests the shell did not have a significant impact on the dose within the CTV. Further work could investigate the impact on the dose distribution by performing gamma analysis on the dose distribution between phantom setups (setup 1 – with shell and setup 2 - without shell) using film. The development of a range of shell thicknesses between 0.2 and 1 cm would allow further understanding on the effects of weight variation that lead to patient treatment replan, as well as support online adaptive planning development within clinical centres.

4.5. Conclusion

In conclusion, an anthropomorphic head and neck phantom was successfully designed, manufactured, and tested as an audit phantom. The study showed 2% agreement between ionisation chamber and alanine within the CTV region to TPS predictions. Results for the OAR region were mixed and highlighted the challenges of measuring dose in this region with dosimetry detectors. Film analysis showing a >95% pass rate for 4%/3 mm gamma analysis (global and local) for both centres. Overall, the phantom is a useful tool to evaluate proton therapy deliveries and provides a realistic challenge for clinical centres as part of an end-to-end audit service.

5. Final Remarks

With proton therapy becoming an adopted form of radiotherapy for the treatment of complex paediatric and adult cancers, there is a need to support and provide clinical centres with confidence that they are providing good quality and safe treatment to patients. Audits have been shown to uphold and improve standards as well as help highlight any potential issues with a treatment. This work has contributed to proton therapy audits, through the development of tools and techniques that increase the accuracy and consistency on the determination of absorbed dose in proton therapy centres.

Previous work had highlighted the uncertainties that current plastic phantom materials can cause to proton dosimetry measurements within anthropomorphic phantoms. Consequently, during my project a model was developed to formulate tissue-equivalent materials which were optimised for both photon imaging and therapeutic proton beams. A series of novel bone and muscle formulations were manufactured and characterised by Monte Carlo simulations and by experiments. Overall, the best new formulations were shown to meet the tissue-equivalent materials criteria specific. The best novel plastics, vertebra bone (VB#2) and muscle plastics (MS#6), were shown to be better optimised than current phantom materials, matching mass density, mass attenuation and RSP within 2% and for vertebra bone-equivalent plastics, it was possible to match nuclear and scattering properties within 5%. However, due to the challenges of manufacturing a homogenous muscle-equivalent plastic, compromise was required to ensure a match the selected photon and proton

interactions within 2%. This resulted in a formulation that did not match scattering and nuclear interactions within the 5% criteria when compared to real muscle. Therefore, the material's scattering and nuclear interactions properties do not accurately mimic muscle tissue.

During my project, I also developed two novel phantoms to help support clinical centres with key challenges of proton therapy deliveries. Due to the way protons interact with matter, tissue heterogeneity and patient variation can have a significant impact on proton treatment deliveries within certain clinical scenarios. Consequently, there was a need for phantoms which can be used as QA tools to assess these complex and challenging proton deliveries.

The RaLPh phantom was shown to be a compact and simple setup which passed the acceptable proton phantom criteria of providing repeatable and accurate dosimetry measurements. Range measurements had an average uncertainty of 0.5 % when considering the relative standard uncertainty in positioning of EBT3 film in the phantom and repeatability of measurement. These allowed for a variety of material configurations (water, bone, and lung-equivalent materials) to be experimentally tested and compared against TPS calculations. However, it should be noted the phantom did not pass the end-to-end audit tool criteria as a material override is currently required for the phantom materials. However, due to the development of the novel muscle and bone-equivalent materials during this work, the phantom materials could be replaced with these new materials to enable end-to-end audit capabilities.

The next step was to use the muscle and bone materials in the design and manufacture of the PRuDeNCE phantom which was then successfully trialled as an end-to-end audit device. The anthropomorphic head and neck phantom was tested in

a pilot audit study at the two NHS high energy scanning proton centres. Absolute dose and relative dose distribution measurements were taken in the CTV, spinal OAR, and coronal slice within the phantom with the use of ionisation chamber, alanine pellets and EBT3 film. Results showed ionisation chamber and alanine dose measurements to be within 2% of TPS predictions with the CTV and OAR (excluding the Centre B's OAR measurements). The gamma index of film dose distribution showing a >95% agreement for a 4% /3 mm gamma pass rate. The phantom was shown to be a useful tool to evaluate proton therapy deliveries to the oropharyngeal cancer site and provides a realistic challenge for clinical centres as part of an end-to-end audit service. Consequently, the phantom passed the acceptable proton phantom criteria specified for this project.

The research achievements described in this thesis can be summarised as i) the formulation, manufacture, and characterization of novel tissue-equivalent materials for proton therapy phantoms, ii) development of a proton range audit device (RaLPh) and iii) development of a head and neck phantom (PRuDeNCE) as an end-to-end audit device for adaptive radiotherapy applications.

To bring this work forward to full auditing capabilities, further work needs to characterise the phantom detectors in more detail and realise full metrological uncertainty budgets for their use for this purpose. Specifically, it may be valuable to perform further work to provide more confidence in the determination of relative effectiveness correction of these detectors when using them as absolute dosimeters within end-to-end audit devices. Alternative detectors to the ones used in this work should be considered for phantom purposes, such silicon diodes, gels, TLD and OSLD detectors.

FINAL REMARKS

For the expansion of auditing capabilities for different sites and patient ages, such as Liver, Breast, Paediatric Head and Neck and Paediatric Spine, other tissue-equivalent materials such as lung, adipose, brain, breast, liver, brain stem, should be developed. Further work could consider other technologies for producing anthropomorphic phantoms as 3D printing due to its efficient and cost-effective method of manufacture. The formulation of tissue-equivalent materials through the cost-function model has also highlighted the need for better cross-sectional data for the characterisation of nuclear interactions of materials in proton beams.

In summary, my work has supported and progressed the methodologies and tools for the development of proton therapy audits within the UK. I have developed novel phantom materials and phantoms for independent audit to provide confidence in the delivery of complex proton therapy treatments.

References

[1] Crellin A.M., Burnet N.G. Proton Beam Therapy: The Context, Future Direction and Challenges Become Clearer Department of Health Strategy for Proton Developing Strategies for Selecting. Clinical Oncology, **26,**736–8, (2014)

[2] NHS England. Clinical Commissioning Policy: Proton Beam Therapy for Children, Teenagers and Young Adult in the treatment of malignant and non-malignant tumours. NHS Report, 200808P, (2020)

[3] Newhauser W.D., Zhang R. The physics of proton therapy. Physics in Medicine and Biology, **60**,155–209. (2015)

[4] Bhatia S., Sklar C. Second cancers in survivors of childhood cancer. Nature Reviews Cancer, **2**, 124–32, (2002)

[5] Hooning M.J., Botma A., Aleman B.M.P., Baaijens M.H.A., Bartelink H., Klijn J.G.M, et al. Long-term risk of cardiovascular disease in 10-year survivors of breast cancer. Journal of the National Cancer Institute, **99,** 365–**7**5, (2007)

[6] Biedka M., Kuźba-Kryszak T., Nowikiewicz T., Zyromska A. Fertility impairment in radiotherapy. Contemporary Oncology (Pozn) **20,** 199–204, (2016)**.**

[7] van de Schoot A.J.A.J., de Boer P., Crama K.F., Visser J., Stalpers L.J.A., Rasch C.R.N., et al. Dosimetric advantages of proton therapy compared with photon therapy using an adaptive strategy in cervical cancer. Acta Oncologica 55, 892–9, (2016)

[8] Steneker M., Lomax A., Schneider U. Intensity modulated photon and proton therapy for the treatment of head and neck tumors. Radiotherapy and Oncology **80**, 263–7, (2016)

[9] Harrabi S.B., Bougatf N., Mohr A., Haberer T., Herfarth K., Combs S.E., et al. Dosimetric advantages of proton therapy over conventional radiotherapy with photons in young patients and adults with low-grade glioma. Strahlentherapie Onkologie **192,** 759–69, (2016)

[10] Paganetti H. *Proton Therapy Physics*. Taylor & Francis Inc, (2012)

[11] Leuven U.Z. Proton Therapy (2019) https://www.uzleuven.be/en/proton-therapy (accessed January 31, 2020).

[12] Andreo P., Burns D.T., Nahum A.E., Seuntjens J., Attix F.H. Fundamentals of Ionizing Radiation Dosimetry. WILEY (2017)

[13] Andreo P., Evans M.D.C., Hendry J.H., Horton J.L., Izewska J., Mijnheer B.J., et al. *External Photon Beams: Physical Aspects. Radiation Oncology Physics: A handbook for Teachers and Students*, IAEA Technical report ST1/PUB/196, 161–217, (2005)

[14] Leeman J., Romesser P., Zhou Y., Sean M., Riaz N, Sherman E. Proton therapy for head and neck cancer: expanding the therapeutic window. The Lancet Oncology **18**, 254-265 (2017).

[15] Rana S., Zeidan O., Ramirez E., Rains M., Gao J., Zheng Y. Measurements of lateral penumbra for uniform scanning proton beams under various beam delivery conditions and comparisons to the XiO treatment planning system. Medical Physics, **40,** 091708, (2013)

[16] Safai S., Bortfeld T., Engelsman M. Comparison between the lateral penumbra of a collimated double-scattered beam and uncollimated scanning beam in proton radiotherapy. Physics in Medicine & Biology, **53**, 1729, (2008)

[17] ICRU. *Fundamental quantities and units for ionizing radiation (revised)*, ICRU Report 85, Oxford University Press **11**, 1-30 (2011)

[18] Palmans H., Seuntjens J., Verhaegen F., Denis J.M., Vynckier S., Thierens H. Water calorimetry and ionization chamber dosimetry in an 85-MeV clinical proton beam. Medical Physics **23,** 643–50, (1996)

[19] Lourenço A., Lee N., Shipley D., Romano F., Kacperek A., Duane S., et al. Application of a portable primary standard level graphite calorimeter for absolute dosimetry in a clinical low-energy passively scattered proton beam. Physics in Medicine and Biology **67,** 1-19, (2022)**.**

[20] Thomas R.A.S., Bolt M.A., Bass G., Nutbrown R., Chen T., Nisbet A., et al. Radiotherapy reference dose audit in the United Kingdom by the National Physical Laboratory: 20 years of consistency and improvements. Physics and Imaging in Radiation Oncology **3**, 21–7, (2017)

[21] Andreo P., Burns D.T., Hohlfeld, K., Huq, M.S., Kanai T., Laitano F., et al. *Absorbed Dose Determination in External Beam Radiotherapy: An International Code of Practice for Dosimetry based on Standards of Absorbed Dose to Water.* IAEA Technical Report Series TRS-398 113-24, (2000).

[22] Seco, J., Verhaegen, F. *Monte Carlo Techniques in Radiation Therapy*. 1st ed. CRC Press (2013)

[23] Seltzer S.M. *An Overview of ETRAN Monte Carlo Methods*. In Monte Carlo Transport of Electrons and Photons, Springer US; **38** 153–81, (1988)

[24] Battistoni G., Boehlen T., Cerutti F., Chin P.W., Esposito L.S., Fassò A., et al. Overview of the FLUKA code. Annals of Nuclear Energy **82**, 10–8, (2015)

[25] Rogers D.W.O. Fifty years of Monte Carlo simulations for medical physics*. Physics in Medicine & Biology **51**, 287-301, (2006)

[26] Agostinelli S., Allison J., Amako K., Apostolakis J., Araujo H., Arce P., et al. Geant4—a simulation toolkit. Nuclear Instruments and Methods in Physics Research Section A: Accelerators, Spectrometers, Detectors and Associated Equipment **506**, 250–303, (2003)

[27] Nuclear Energy Agency. *PENELOPE 2018: A code system for Monte Carlo simulation of electron and photon transport.* Workshop Proceedings, Spain 1-420, (2019)

[28] Andreo P. Monte Carlo simulations in radiotherapy dosimetry. Radiation Oncology **13** 1-15 (2018)

[29] Royal College of Radiologists, Society and College of Radiographers, Institute of Physics and Engineering in Medicine, National Patient safety Agency, British Institute of Radiology. *Towards Safer Radiotherapy*. London: Royal College of Radiologists, Report BFCO(08)1 (2008)

[30] Merwe D van der., Dyk J.V., Healy B., Zubizarreta E., Izewska J., Mijnheer B., et al. Accuracy requirements and uncertainties in radiotherapy: a report of the International Atomic Energy Agency. Acta Oncologica **56,** 1-6 (2017)

[31] ICRU. *Determination of absorbed dose in a patient irradiated by beams of X or Gamma rays in radiotherapy procedures (Report 24)*, *Bethesda, MD,* **15**, 3, (1976)

[32] Thwaites D. Accuracy required and achievable in radiotherapy dosimetry: have modern technology and techniques changed our views ? Journal of Physics: Conference Series, IOP Publishing, **444**, 012006, (2013)

[33] Chang D.S., Foster D.L., Das .IJ., Mendonca MS, Dynlacht JR. *Therapeutic Ratio*. In: Basic Radiotherapy Physics and Biology, Springer 277–82, (2014)

[34] Lomax A. *SFUD, IMPT, and Plan Robustness*. In: Particle Radiotherapy, Springer 169–94 (2016)

[35] Paganetti H. Range uncertainties in proton therapy and the role of Monte Carlo simulations. Physics in Medicine and Biology **57**, 99-117, (2012)

[36] Clark C.H., Aird E.G., Bolton S., Miles E.A., Nisbet A., Snaith J.A.D., et al. Radiotherapy dosimetry audit: three decades of improving standards and accuracy in UK clinical practice and trials. The British Journal of Radiology **88**, 20150251, (2015)

[37] Carlino A., Gouldstone C., Kragl G., Traneus E., Marrale M., Vatnitsky S., et al. End-to-end tests using alanine dosimetry in scanned proton beams. Physics in Medicine and Biology **63**, 055001, (2018)

[38] ICRU. *Tissue Substitutes in Radiation Dosimetry and Measurement.* ICRU Report 44. Oxford University Press (1993)

[39] DeWerd L.A., Kissick M. *The Phantoms of Medical and Health Physics*. Springer, (2014)

[40] McGarry C.K., Grattan L.J., Ivory A.M., Leek F., Liney G.P., Liu Y., et al. Tissue mimicking materials for imaging and therapy phantoms: A review. Physics in Medicine and Biology **65**,1-43, (2020)

[41] Tillery H., Moore M., Gallagher K.J., Taddei P.J., Leuro E., Argento D., et al. Personalized 3D-printed anthropomorphic whole-body phantom irradiated by protons, photons, and neutrons. Biomedical Physics and Engineering Express **8**, 027004, (2022)

[42] Sun Nuclear. *ATOM Dosimetry Phantoms (Model 701-706)*. CIRS Inc Product Data Sheet ATOMPhantomFamily_110822, (2022)

[43] IBA, *Integrated Beam Scanning and Annual QA* IBA Data Sheet Beam_Scanning-Br-E_Rev.2_0620, (2022)

[44] Sun Nuclear. *Xsight Lung Tracking Phantom Kit (Model 18023-A)*. CIRS Inc Product Data Sheet 18023-A-PB 060222 (2016)

[45] Radiology Support Devices Inc. *Nuclear Medicine Phantoms.* RSD Product Data Sheet RSD-Tech-Data-012721 (2021)

[46] Sun Nuclear. *Plastic Water® (Model PW).* CIRS Inc Product Data Sheet PW DS 120418 (2013)

[47] Woodard H.Q., White D.R. The composition of body tissues. The British Journal of Radiology 59,149–59, (2014)

[48] Snyder, W.S., Cook, M.J., Nasset, E.S., Karhausen, L.R., Howells, G.P., Tipton, I.H. *Report on the Task Group on Reference Man* (ICRP publication 23). Pergamon Press 1975.

[49] Shrimpton P.C., Wall B.F., Fisher E.S. The tissue-equivalence of the Alderson Rando anthropomorphic phantom for X-rays of diagnostic qualities. Physics in Medicine and Biology, **26**, 133–9, (1981)

[50] Bondesson D., Meijers A., Janssens G., Rit S., Rabe M., Kamp F., et al. Anthropomorphic lung phantom based validation of in-room proton therapy 4D-CBCT image correction for dose calculation. Zeitschrift Fur Medizinische Physik 1-11, (2020)

[51] Bär E., Lalonde A., Zhang R., Jee K.W., Yang K., Sharp G., et al. Experimental validation of two dual-energy CT methods for proton therapy using heterogeneous tissue samples. Medical Physics **45,** 48–59, (2018)

[52] White D.R. *The formulation of substitute materials with predetermined characteristics of radiation absorption and scattering.* Queen Mary University of London (1974)

[53] Akhlaghi P., Hakimabad H.M., Motavalli L.R. Determination of tissue equivalent materials of a physical 8-year-old phantom for use in computed tomography. Radiation Physics and Chemistry **112**, 169–76, (2015)

[54] Stacey A.J., Bevan A.R., Dickens C.W. A new phantom material employing depoymerised natural rubber. British Journal of Radiology 34, 510–5, (2014)

[55] Frigerio N.A., Coley R.F., Sampson M.J. Depth dose determinations I. Tissue-equivalent liquids for Standard Man and muscle. Physics in Medicine and Biology **17**,792–802, (1972)

[56] Constantinou C. Tissue substitutes for particulate radiations and their use in radiation dosimetry and radiotherapy Queen Mary University of London (1978)

[57] Winslow J.F., Hyer D.E., Fisher R.F., Tien C.J., Hintenlang D.E. Construction of anthropomorphic phantoms for use in dosimetry studies. Journal of Applied Clinical Medical Physics **10,** 195–204, (2009)

[58] Tino R., Yeo A., Leary M., Brandt M., Kron T. A Systematic Review on 3D-Printed Imaging and Dosimetry Phantoms in Radiation Therapy. Technology in Cancer Research and Treatment **18,** 1–14, (2019)

[59] Yea J.W., Park J.W., Kim S.K., Kim D.Y., Kim J.G., Seo C.Y., et al. Feasibility of a 3D-printed anthropomorphic patient-specific head phantom for patient-specific quality assurance of intensity-modulated radiotherapy. PLoS ONE **12**, 1–11, (2017)

[60] Zhang F., Zhang H., Zhao H., He Z., Shi L., He Y., et al. Design and fabrication of a personalized anthropomorphic phantom using 3D printing and tissue equivalent materials. Quantitative Imaging in Medicine and Surgery **9**, 94–100, (2019)

[61] Soultanidis G., Subiel A., Renard I., Reinhart A.M., Green V.L., Oelfke U., et al. Development of an anatomically correct mouse phantom for dosimetry measurement in small animal radiotherapy research. Physics in Medicine and Biology **64**, 12NT02 (2019)

[62] Ehler E., Craft D., Rong Y. 3D printing technology will eventually eliminate the need of purchasing commercial phantoms for clinical medical physics QA procedures. Journal of Applied Medical Physics **19**, 8–12, (2018)

[63] Taylor P., Craft D., Followill D., Howell R. SU-F-T-181: Proton Therapy Tissue-Equivalence of 3D Printed Materials. Medical Physics **43**, 3503, (2016)

[64] Filippou V., Tsoumpas C. Recent advances on the development of phantoms using 3D printing for imaging with CT, MRI, PET, SPECT, and ultrasound. Medical Physics **45**, e740–60, (2018)

[65] CIRS Inc. *Proton Therapy Dosimetry Head (Model 731-HN)*. CIRS Inc Product Data Sheet 731HN DS 120418 (2013)

[66] Gordeev E.G., Galushko A.S., Ananikov V.P. Improvement of quality of 3D printed objects by elimination of microscopic structural defects in fused deposition modeling. PLoS ONE **13**, 1-19 (2018)

[67] Botnariuc D., Ghica C., Cook H., Bento M., Nisbet A., Royle G., et al. A Monte Carlo framework to evaluate the radiological properties of 3D-printable materials for proton therapy phantom development. International Conference on Monte Carlo Techniques for Medical Applications, (2022)

[68] Taylor P.A., Kry S.F., Alvarez P., Tyler K., Lujano C., Hernandez N., et al. Results From the Imaging and Radiation Oncology Core Houston's Anthropomorphic Phantoms Used for Proton Therapy Clinical Trial Credentialing. International Journal of Radiation Oncology - Biology - Physics **95**, 242-248 (2016)

[69] Kirby T.H., Hanson W.F., Johnston D.A. Uncertainty analysis of absorbed dose calculations from thermoluminescence dosimeters. Medical Physics **19,** 1427–33, (1992)

[70] Alvarez P., Kry S.F., Stingo F., Followill D. TLD and OSLD dosimetry systems for remote audits of radiotherapy external beam calibration. Radiation Measurements **106**, 412–5, (2017)

[71] Palmans H., Carlino, A., Gouldstone, C., Sharpe P. Cross Calibration of Alanine for scanned proton beams. NPL Report IR 48 (2018).

[72] Branco D., Taylor P., Zhang X., Li H., Guindani M., Followill D. An Anthropomorphic Head and Neck Quality Assurance Phantom for Credentialing of Intensity-Modulated Proton Therapy. International Journal of Particle Therapy **4**, 40–7, (2017)

[73] Lewis D.J., Taylor P.A., Followill D.S., Sahoo N., Mahajan A., Stingo F.C., et al. A New Anthropomorphic Pediatric Spine Phantom for Proton Therapy Clinical Trial Credentialing. International Journal of Particle Therapy **4**, 40-7, (2018)

[74] Sądel M, Bilski P, Swakoń J, Rydygier M, Horwacik T, Weber A. Comparative investigations of the relative thermoluminescent efficiency of LiF detectors to protons at different proton therapy facilities. Radiation Measurements **82,** 8–13, (2015)

[75] Kerns JR, Kry SF, Sahoo N. Characteristics of optically stimulated luminescence dosimeters in the spread-out Bragg peak region of clinical proton beams. Med Phys **39**, 854–63, (2012)

[76] Fiorini F., Kirby D., Thompson J., Green S., Parker D.J., Jones B., et al. Under-response correction for EBT3 films in the presence of proton spread out Bragg peaks. Physica Medica **30**, 454–61, (2014)

[77] Kirby D., Green S., Palmans H., Hugtenburg R., Wojnecki C., Parker D. LET dependence of GafChromic films and an ion chamber in low-energy proton dosimetry. Physics in Medicine and Biology **55,** 417–33, (2010)

[78] Grant R.L., Summers P.A., Neihart J.L., Blatnica A.P., Sahoo N., Gillin M.T., et al. Relative stopping power measurements to aid in the design of

anthropomorphic phantoms for proton radiotherapy. Journal of Applied Clinical Medical Physics **15**, 121–6, (2014)

[79] Constantinou C., Attix F.H., Bhudatt M.S., Paliwal R. A solid water phantom material for radiotherapy x-ray and γ-ray beam calibrations. Medical Physics **9,** 311–449, (1982)

[80] Nenoff L., Matter M., Charmillot M., Krier S., Uher K., Weber D.C., et al. Experimental validation of daily adaptive proton therapy. Physics in Medicine and Biology **66**, 2505010, (2021)

[81] Grevillot L., Stock M., Palmans H., Moreno J.O., Letellier V., Dreindl R., et al. Implementation of dosimetry equipment and phantoms at the MedAustron light ion beam therapy facility. Medical Physics **45**, 352–69, (2018)

[82] Dietlicher I., Casiraghi M., Ares C., Bolsi A., Weber D.C., Lomax A.J., et al. The effect of surgical titanium rods on proton therapy delivered for cervical bone tumors: Experimental validation using an anthropomorphic phantom. Physics in Medicine and Biology **59**, 7181–94, (2014)

[83] Ableitinger A., Vatnitsky S., Herrmann R., Bassler N., Palmans H., Sharpe P., et al. Dosimetry auditing procedure with alanine dosimeters for light ion beam therapy. Radiotherapy and Oncology **108**, 99–106 (2013)

[84] Nishio T., Tachibana H., Kase Y., Hotta K., Nakamura M., Tamura M., et al. Liver phantom design and dosimetric verification in participating institutions for a proton beam therapy in patients with resectable hepatocellular carcinoma: Japan Clinical Oncology Group trial (JCOG1315C). Radiotherapy and Oncology **140,** 98–104, (2019)

[85] Kostiukhina N., Georg D., Rollet S., Kuess P., Sipaj A., Andrzejewski P., et al. Advanced Radiation DOSimetry phantom (ARDOS): A versatile breathing phantom for 4D radiation therapy and medical imaging. Physics in Medicine and Biology **62**, 8136–53 (2017)

[86] Kostiukhina N., Palmans H., Stock M., Georg D., Knäusl B. Dynamic lung phantom commissioning for 4D dose assessment in proton therapy. Physics in Medicine and Biology 64, 235001 (2019)

[87] Poel R., Belosi F., Albertini F., Walser M., Gisep A., Lomax A.J., et al. Assessing the advantages of CFR-PEEK over titanium spinal stabilization implants in proton therapy - A phantom study. Physics in Medicine and Biology **65,** 245031, (2020)

[88] Palmans H., Symons J.E., Denis J.M., De Kock E.A., Jones D.T.L., Vynckier S. Fluence correction factors in plastic phantoms for clinical proton beams. Physics in Medicine and Biology **47,** 3055–71,(2002)

[89] Al-Sulaiti L, Shipley D, Thomas R, Owen P, Kacperek A, Regan PH, et al. Water equivalence of some plastic-water phantom materials for clinical proton beam dosimetry. Applied Radiation and Isotopes 70, 1052-7 (2012)

[90] Lourenço A., Shipley D., Wellock N., Thomas R., Bouchard H., Kacperek A., et al. Evaluation of the water-equivalence of plastic materials in low- and high-energy clinical proton beams. Physical in Medicine and Biology **62**,3883–901, (2017)

[91] Leeds Test Objects. *Tissue Equivalent Materials: The Original Tissue Equivalents.* Leeds Test Object Product Data Sheet (2014)

[92] Khachonkham S., Dreindl R., Heilemann G., Lechner W., Fuchs H., Palmans H., et al. Characteristic of EBT-XD and EBT3 radiochromic film dosimetry for photon and proton beams. Physics in Medicine and Biology **63**,065007, (2018)

[93] Reinhardt S., Hillbrand M., Wilkens J.J., Assmann W. Comparison of Gafchromic EBT2 and EBT3 films for clinical photon and proton beams. Medical Physics **39**, 5257–62, (2012)

[94] McGowan S.E., Burnet N.G., Lomax A.J. Treatment planning optimisation in proton therapy. British Journal of Radiology **86**, 20120288, (2013)

[95] Unkelbach J. Paganetti H. Robust Proton Treatment Planning: Physical and Biological Optimization. Seminars in Radiation Oncology **28**, 88–96, (2018)

[96] Knopf A.C., Lomax A. In vivo proton range verification: A review. Physics in Medicine and Biology **58**, 131–6, (2013)

[97] Hillbrand M., Landry G., Ebert S., Dedes G., Pappas E., Kalaitzakis G., et al. Gel dosimetry for three-dimensional proton range measurements in anthropomorphic geometries. Zeitschrift für Medizinishe Physik **29**,162–72, (2019)

[98] Kim D.H., Cho S., Jo K., Shin E.H., Hong C.S., Han Y., et al. Proton range verification in inhomogeneous tissue: Treatment planning system vs. measurement vs. Monte Carlo simulation. PLoS ONE **13**,1–14 (2018)

[99] Farr J.B., Moyers M.F., Allgower C.E., Bues M., Hsi W.C., Jin H., et al. Clinical commissioning of intensity-modulated proton therapy systems: Report of AAPM Task Group 185. Medical Physics **48**, e1–30, (2021)

[100] Zhao L., Das .IJ. Gafchromic EBT film dosimetry in proton beams. Physics in Medicine and Biology **55**, N291, (2010)

[101] Piermattei A., Miceli R., Azario L., Fidanzio A., Delle Canne S., De Angelis C., et al. Radiochromic film dosimetry of a low energy proton beam. Medical Physics **27**, 1655–60, (2000)

[102] Vatnitsky S.M. Radiochromic film dosimetry for clinical proton beams. Applied Radiation and Isotopes **48**, 643–51, (1997)

[103] Devic S, Tomic N, Lewis D. Reference radiochromic film dosimetry: Review of technical aspects. Physica Medica **32,** 541–56, (2016)

[104] 3D Systems Inc. *Accura® Bluestone™* 3D Systems Product Data Sheet 09-20 (2020)

[105] Niroomand-Rad A., Blackwell C.R., Coursey B.M., Gall K.P., Galvin J.M., McLaughlin W.L., et al. *Radiochromic film dosimetry: recommendations of AAPM Radiation Therapy Committee Task Group 55*. Medical Physics **25**, 2093–115, (1998)

[106] Bouchard H., Lacroix F., Beaudoin G., Carrier J.F., Kawrakow I. On the characterization and uncertainty analysis of radiochromic film dosimetry. Medical Physics **36,** 1931–46, (2009)

[107] Miura H., Ozawa S., Hosono F., Sumida N., Okazue T., Yamada K., et al. Gafchromic EBT-XD film: Dosimetry characterization in high-dose, volumetric-modulated arc therapy. Journal of Applied Clinical Medical Physics **17,** 312–22, (2016)

[108] Marroquin E.Y., González J.A.H., López M.A.C, Barajas V., García-Garduño O.A. Evaluation of the uncertainty in an EBT3 film dosimetry system utilizing net optical density. Journal of Applied Clinical Medical Physics **17**, 466–81, (2016)

[109] Lewis D., Micke A., Yu X., Chan MF. An efficient protocol for radiochromic film dosimetry combining calibration and measurement in a single scan. Medical Physics, **39,** 6339-50, (2012)

[110] Lewis D., Chan MF. Correcting lateral response artifacts from flatbed scanners for radiochromic film dosimetry. Medical Physics, **42,** 416–29, (2015)

[111] Schoenfeld A.A., Wieker S., Harder D., Poppe B. The origin of the flatbed scanner artifacts in radiochromic film dosimetry-key experiments and theoretical descriptions. Physics in Medicine and Biology **61**, 7704–24, (2016)

[112] Palmer A.L., Bradley D., Nisbet A. Evaluation and implementation of triple-channel radiochromic film dosimetry in brachytherapy. Journal of Applied Clinical Medical Physics **15**, 280–96, (2014)

[113] Micke A., Lewis D.F., Yu X. Multichannel film dosimetry with nonuniformity correction. Medical Physics **38**, 2523–34, (2011)

[114] Zhang R., Newhauser W.D. Calculation of water equivalent thickness of materials of arbitrary density, elemental composition and thickness in proton beam irradiation. Physics in Medicine and Biology **54,** 1–19, (2009)

[115] Gottschalk B. Comments on “Calculation of water equivalent thickness of materials of arbitrary density, elemental composition and thickness in proton beam irradiation.” Physics in Medicine and Biology **55**, 29-30, (2010)

[116] Newhauser W., Zhang R. Reply to ’Comments on “calculation of water equivalent thickness of materials of arbitrary density, elemental composition and thickness in proton beam irradiation.” Physics in Medicine and Biology **55**, 31–3, (2010)

[117] Böhlen T.T., Cerutti F., Chin M.P.W., Fassò A., Ferrari A., Ortega P.G., et al. The FLUKA Code: Developments and challenges for high energy and medical applications. Nuclear Data Sheets **120**, 211–4, (2014)

[118] Vlachoudis V. Flair: A powerful but user friendly graphical interface for FLUKA. International Conference on Mathematics, Computational Methods & Reactor Physics, Saratoga Springs, New York, (2009)

[119] ICRU. *Key Data For Ionizing-Radiation Dosimetry: Measurement Standards And Applications*. ICRU Report 90. Oxford University Press **14** (2014)

[120] Schneider U., Pedroni E., Lomax A. The calibration of CT Hounsfield units for radiotherapy treatment planning. Physics in Medicine and Biology 41, 111, (1996)

[121] Cook H., Royle G., Palmans H., Lourenço A. *Simulations for the improvement of bone-equivalent materials for proton beam dosimetry,* International Conference on Monte Carlo Techniques for Medical Applications. (2019)

[122] Paganetti H. Proton beam therapy. IOP Publishing, 1–23 (2017)

[123] Taylor P.A., Lowenstein J., Followill D., Kry S.F. The Value of On-Site Proton Audits. International Journal of Radiation Oncology - Biology - Physics **112**, 1004–11, (2022)

[124] Rossi H, Failla G. Tissue-equivalent ionisation chambers. Nucleonics 14, (1965)

[125] Shonka R.F. Conducting plastic equivalent to tissue, air, and polystyrene. Second United Nations International Conference on Peaceful Use of Atomic Energy, 160, (1958)

[126] Spiers F.W. Effective Atomic Number and Energy Absorption in Tissues. The British Journal of Radiology **19**, 52–63, (1946)

[127] Weber J., van den Berge D.J. The effective atomic number and the calculation of the composition of phantom materials. The British Journal of Radiology **42**,378–83, (1969)

[128] White D.R. The formulation of tissue substitute materials using basic interaction data. Physics in Medicine and Biology **22**, 889–99, (1977)

[129] White D.R., Martin R.J., Darlison R. Epoxy resin based tissue substitutes. The British Journal of Radiology **50**, 814–21, (1977)

[130] White D.R. Tissue substitutes in experimental radiation physics. Physics in Medicine and Biology **5**, 467–79 (1978)

[131] Cook H., Lambert J., Thomas R., Palmans H., Hussein M., Clark C.H., et al. Development of a heterogeneous phantom to measure range in clinical proton therapy beams. Physica Medica **93**, 59-68, (2022)

[132] Xu X.G., Eckerman K. *Handbook of anatomical models for radiation dosimetry*. WILEY (2009)

[133] Gottschalk B. On the scattering power of radiotherapy protons. Medical Physics, **37**, 352–67, (2010)

[134] ICRU. *Stopping Power of Electrons and Positrons.* ICRU Report 37 Oxford University Press **2** (1984)

[135] Palmans H., Al-Sulaiti L., Andreo P., Shipley D., Lühr A., Bassler N., et al. Fluence correction factors for graphite calorimetry in a low-energy clinical proton beam: I. Analytical and Monte Carlo simulations. Physics in Medicine and Biology **58**, 3481–99, (2013)

[136] Lourenço A., Thomas R., Bouchard H., Kacperek A., Vondracek V., Royle G., et al. Experimental and Monte Carlo studies of fluence corrections for graphite calorimetry in low- and high-energy clinical proton beams. Medical Physics **43**, 4122–32, (2016)

[137] ICRU. *Nuclear Data for Neutron and Proton Radiotherapy and for Radiation Protection* ICRU Report 63. Oxford University Press (2000)

[138] Rossi B. *High-energy Particles.* Prentice-Hall, (1952)

[139] Goma C., Almeida I.P., Verhaegen F. Revisiting the single-energy CT calibration for proton therapy treatment planning: a critical look at the stoichiometric method. Physics in Medicine & Biology **63**, 235011, (2018)

[140] CIRS Inc. *CIRS Tissue Equivalent Materials (Model XXX)* CIRS Product Data Sheet TE DE Draft 062920 (2020)

[141] Sun Nuclear. Advanced Electron Density Phantom. CIRS Inc Product Data Sheet AEDP_052422 (2022)

[142] Barca P., Paolicchi F., Aringhieri G., Palmas F., Marfisi D., Fantacci M.E., et al. A comprehensive assessment of physical image quality of five different scanners for head CT imaging as clinically used at a single hospital centre—A phantom study. PLoS ONE **16**, 1–17, (2021)

[143] National Physical Laboratory. Improving confidence in intra-operative cancer detection technologies Webpage accessed June 29 (2022)

[144] Byrd R.H., Gilbert J.C., Nocedal J. A trust region method based on interior point techniques for nonlinear programming. Mathematical Programming **89**, 149–85, 2000

[145] Viviani G.L. Practical Optimization. IEEE Power Engineering Review 5, 33, (1985)

[146] Bortfeld T. An analytical approximation of the Bragg curve for therapeutic proton beams. Medical Physics **24**, 2024–33, (1997)

[147] Bourque A.E., Carrier J.F., Bouchard H. A stoichiometric calibration method for dual energy computed tomography. Physics in Medicine and Biology **59**, 2059–88, (2014)

[148] Rasouli F.S., Masoudi S.F., Jette D. Technical Note: On the analytical proton dose evaluation in compounds and mixtures. Medical Physics **43**, 303–7, (2016)

[149] Sio T.T., Lin H.K., Shi Q., Gunn G.B., Cleeland C.S., Lee J.J., et al. Intensity modulated proton therapy versus intensity modulated photon radiation therapy for oropharyngeal cancer: First comparative results of patient-reported outcomes. International Journal of Radiation Oncology Biology Physics **95**,1107–14, (2016)

[150] Dagan R., Bryant C.M., Bradley J.A., Indelicato D.J., Rutenberg M., Rotondo R., et al. A Prospective Evaluation of Acute Toxicity from Proton Therapy for Targets of the Parotid Region. International Journal of Particle Therapy **3**, 285–90, (2016)

[151] Gunn G.B., Blanchard P., Garden A.S., Zhu X.R., Fuller C.D., Mohamed A.S.R., et al. Clinical outcomes and patterns of disease recurrence following intensity modulated proton therapy for oropharyngeal squamous carcinoma International Journal of Radiation Oncology, Biology, Physics **95**, 360–7, (2016)

[152] Holliday E.B., Kocak-Uzel E., Feng L., Thaker N.G., Blanchard P., Rosenthal D.I., et al. Dosimetric advantages of intensity-modulated proton therapy for oropharyngeal cancer compared with intensity-modulated radiation: A case-matched control analysis. Medical Dosimetry **41**, 189–94, (2016)

[153] Slater J.D., Yonemoto L.T., Mantik D.W., Bush D.A., Preston W., Grove R.I., et al. Proton radiation for treatment of cancer of the oropharynx: Early experience at Loma Linda University Medical Center using a concomitant boost technique. International Journal of Radiation Oncology Biology Physics **62**, 494–500, (2005)

[154] Li X., Lee A., Cohen M.A., Sherman E.J., Lee N.Y. Past, present and future of proton therapy for head and neck cancer. Oral Oncology **110**, 104879, (2020)

[155] Nutting C.M., Morden J.P., Harrington K.J., Urbano T.G., Bhide S.A., Clark C., et al. Parotid-sparing intensity modulated versus conventional radiotherapy in head and neck cancer (PARSPORT): A phase 3 multicentre randomised controlled trial. The Lancet Oncology **12**, 127–36, (2011)

[156] Sharma S., Zhou O., Thompson R., Gabriel P., Chalian A., Rassekh C., et al. Quality of life of postoperative photon versus proton radiation therapy for oropharynx cancer. International Journal of Particle Therapy **5**, 11–7, (2019)

[157] Price J., Hall E., West C., Thomson D. TORPEdO - A Phase III Trial of Intensity-modulated Proton Beam Therapy Versus Intensity-modulated Radiotherapy for

Multi-toxicity Reduction in Oropharyngeal Cancer. Clinical Oncology **32**, 84–8, (2020)

[158] Figen M., Çolpan Öksüz D., Duman E., Prestwich R., Dyker K., Cardale K., et al. Radiotherapy for Head and Neck Cancer: Evaluation of Triggered Adaptive Replanning in Routine Practice. Frontiers in Oncology **10**, 579917, (2020)

[159] Ahn P.H., Lukens J.N., Teo B.K.K., Kirk M., Lin A. The use of proton therapy in the treatment of head and neck cancers. Cancer Journal **20**, 421–6, (2014)

[160] Weber D.C., Tomsej M., Melidis C., Hurkmans C.W. QA makes a clinical trial stronger: Evidence-based medicine in radiation therapy. Radiotherapy and Oncology **105,** 4–8, (2012)

[161] Pettersen M.N., Aird E., Olsen D.R. Quality assurance of dosimetry and the impact on sample size in randomized clinical trials. Radiotherapy and Oncology **6**, 195–9, (2008)

[162] Fedorov A., Beichel R., Kalpathy-Cramer J., Finet J., Fillion-Robin J-C., Pujol S., et al. 3D Slicer as an Image Computing Platform for the Quantitative Imaging Network. Magnetic Resonance Imaging **30**, 1323–41, (2012)

[163] Noble D.J., Yeap P-L., Seah S.Y.K., Harrison K., Shelley L.E.A., Romanchikova M, et al. Anatomical change during radiotherapy for head and neck cancer, and its effect on delivered dose to the spinal cord. Radiotherapy and Oncology, 130, 32–8, (2019)

[164] Senkus-Konefka E., Naczk E., Borowska I., Badzio A., Jassem J. Changes in lateral dimensions of irradiated volume and their impact on the accuracy of dose delivery during radiotherapy for head and neck cancer. Radiotherapy and Oncology, **79,** 304–9, (2006)

[165] Barker J.L.J., Garden A.S., Ang K.K., O'Daniel J.C., Wang H., Court L.E., et al. Quantification of volumetric and geometric changes occurring during fractionated radiotherapy for head-and-neck cancer using an integrated CT/linear accelerator system. International Journal of Radiation Oncology - Biology -Physics, **59,** 960–70, (2004)

[166] Palmans H., Lourenço A., Medin J., Vatnitsky S., Andreo P. Current best estimates of beam quality correction factors for reference dosimetry of clinical proton beams. Phys Med Biol **67**, 195012, (2022)

[167] Green S., Amos R., Van den Heuvel F., Kacperek A., MacKay R.I., Palmans H., et al. EP-1467: IPEM Code of Practice for proton and ion beam dosimetry: update on work in progress. Radiotherapy and Oncology, **123**, S783–4, (2017)

[168] Hussein M., Clark C.H., Nisbet A. Challenges in calculation of the gamma index in radiotherapy – Towards good practice. Physica Medica **36**, 1–11, (2017)

[169] Low D.A., Harms W.B., Mutic S., Purdy JA. A technique for the quantitative evaluation of dose distributions. Medical Physics, **25**, 656–61, (1998)

[170] Resch A.F., Heyes P.D., Fuchs H., Bassler N., Georg D., Palmans H. Dose- rather than fluence-averaged LET should be used as a single-parameter descriptor of proton beam quality for radiochromic film dosimetry. Medical Physics **47**, 2289–99, (2020)

[171] Thwaites D.I., DuSautoy A.R., Jordan T., McEwen M.R., Nisbet A., Nahum A.E., et al. The IPEM code of practice for electron dosimetry for radiotherapy beams

of initial energy from 4 to 25 MeV based on an absorbed dose to water calibration. Physics in Medicine and Biology **48**, 2929–70, (2003)

[172] Aerssens J., Boonen S., Lowet G., Dequeker J. Interspecies differences in bone composition, density, and quality: Potential implications for in vivo bone research. Endocrinology **139**, 663–70, (1996)

[173] Cone S.G., Warren P.B., Fisher M.B. Rise of the Pigs: Utilization of the Porcine Model to Study Musculoskeletal Biomechanics and Tissue Engineering During Skeletal Growth. Tissue Engineering Part C: Methods **23**, 763–80 (2017)

[174] Williams EJ. Concerning the scattering of fast electrons and of cosmic-ray particles. The Royal Society, 531–72, (1939)

[175] Moliere G. Theorie der Streuung schneller geladener Teilchen I. Einzelstreuung am abgeschirmten Coulomb-Feld. Zeitschrift Für Naturforschung A, **2**, 133–45, (1947)

[176] Moliere G. Theorie der Streuung schneller geladener Teilchen II Mehrfach-und Vielfachstreuung. Zeitschrift Für Naturforschung A **3**, 78–97, (1948)

[177] Goudsmit S, Saunderson JL. Multiple Scattering of Electrons. American Physical Society, **57**, 24–9, (1940)

[178] Egan P. fwhm. MATLAB Central File Exchange (2022)

[179] Liszka M., Stolarczyk L., Kłodowska M., Kozera A., Krzempek D., Mojżeszek N., et al. Ion recombination and polarity correction factors for a plane-parallel ionization chamber in a proton scanning beam. Medical Physics **45**, 391–401, (2018)

[180] Rossomme S., Horn J., Brons S., Jäkel O., Mairani A., Ciocca M., et al. Ion recombination correction factor in scanned light-ion beams for absolute dose measurement using plane-parallel ionisation chambers. Physics in Medicine and Biology **62**, 5365–82, (2017)

[181] Eaton DJ., Bass G., Booker P., Byrne J., Duane S., Frame J., et al. IPEM code of practice for high-energy photon therapy dosimetry based on the NPL absorbed dose calibration service. Physics in Medicine and Biology **65**, 195006, (2020)

[182] Butson M.J., Cheung T., Yu P.K.N. Scanning orientation effects on Gafchromic EBT film dosimetry. Australasian Physics and Engineering Sciences in Medicine 29, 281–4, (2006)

[183] Borca V.C., Pasquino M., Russo G., Grosso P., Cante D., Sciacero P., et al. Dosimetric characterization and use of GAFCHROMIC EBT3 film for IMRT dose verification. Journal of Applied Clinical Medical Physics **14**, 158–71 (2013)

Appendices

A.RaLPh in an electron beam

A.1. Introduction

Given the similarity between proton and electron stopping powers, preliminary experiments were performed with electrons at NPL with an Elekta Synergy Linac as a quantitively relevant test of the phantom. For electron measurements, the range was defined as R_{50}, the depth distal to the peak where the percentage depth dose drops to 50%. Preliminary testing also provided testing of the experimental protocol and analysis methods.

A.2. Methods

A.2.1. EBT3 film range measurements with RaLPh

A.2.1.1. Film handling, post-processing, and readout

All film handling, post-processing and readout performed was the same as the procedures explained in Chapter 2, section 2.2.2.1.

A.2.1.2. Film calibration

Firstly, doses were determined with a NACP-02 chamber (Scanditronix medical, Vislanda, SE) operated at -100 V (collecting negative charge) in an 18 MeV electron beam (Elekta Synergy Linac) of 6 x 6 cm^2 field size delivering 100 MU. The chamber was placed in a WTe solid water holder and 3.9 cm WTe electron solid water (BARTS Health NS Trust, UK) build up was placed above the ionisation to position the chamber at 4 cm water-equivalent depth. The ionisation measurements were corrected

following recommendations of the IPEM code of practice [171]. The following equation was applied for the determine of dose:

$$D_{W,Q} = M_1 \cdot N_{D,W} \cdot f_{TP} \cdot f_{ele} \cdot f_{pol} \cdot f_{ion} \quad (\mathrm{A.1})$$

where M_1 is the ionisation chamber reading, $N_{D,W}$ is the calibration coefficient in terms of absorbed dose to water in an electron beam, f_{TP} is the temperature and pressure correction, f_{ele} is the electrometer correction, f_{ion} is the ion recombination correction, and k_{pol} is the polarity correction.

For the EBT3 film calibration, an equivalent 4.0 cm water-equivalent build-up plate of WTe solid water was used and each piece of film was placed in the centre of the 6 x 6 cm^2 field. A 12-point calibration of EBT3 film was determined for the doses delivered as shown in Table A.1.

Table A.1 *Film calibration doses*

Film number	Dose from ionisation chamber (Gy)
1	0.000
2	0.100
3	0.299
4	0.498
5	0.747
6	0.996
7	1.494
8	1.992
9	2.987
10	4.979
11	7.468
12	9.949

A central square region of interest (1.5 x 1.5 cm^2) was taken for each calibration EBT3 film piece and the average scanner signal determined over this region. The following function was fitted to the data:

$$X(D) = \frac{(a + bD)}{(D + c)} \quad (A.2)$$

where $X(D)$ is the average pixel value at dose D, and a, b, and c are the fitted function parameters [112].

A.2.1.3. EBT3 film irradiations for variable phantom configurations

The phantom was positioned on the treatment bed and position markers were drawn around the phantom to make sure the phantom position was identical between phantom configuration changes throughout the experiment. The front face was perpendicular to the beam and the isocentre was aligned with the of front of the phantom; a 1-degree tilt of the gantry (91 degrees) was applied to avoid the tunnelling of the electrons between the gap containing the film. An applicator generating a 6 x 6 cm^2 collimated field was used to simulate a broad beam. An 18 MeV electron beam with 500 MU was delivered to each film. Seven setups using solid water 1472 (Chapter 2, Table 2.1) were performed and each setup was repeated three times. After irradiation, the same film analysis approach described in Chapter 2, section 2.2.2.4. was used for these measurements. The R_{50} for the depth-OD profiles ($R_{50,\mathrm{OD}}^{\mathrm{Film}}$) and the depth-dose profiles ($R_{50,\mathrm{D}}^{\mathrm{Film}}$) were determined for each film irradiation.

A.2.2. Ionisation chamber measurements

A similar experimental approach described in Chapter 2, section 2.2.3.1. was used for these measurements. Terminology used in this section is defined in Chapter 2. A water phantom was set up with a small area PTW Classic Markus chamber 23343

operated at -100 V and positioned 0.1 mm from the front face of the water phantom. An 18 MeV electron beam was used with a 6 x 6 cm^2 field size. The ionisation chamber was moved in 1 mm steps sizes until reaching the range of the distal fall off region of the beam so that a $\mathrm{PDI_w}$ curve could be measured with the ionisation chamber. The PDI of water was measured and then the slabs of solid water (1 cm), lung (0.5 cm) and bone substitutes (0.5 cm) were placed individually in front of the water phantom and the $\mathrm{PDI_{w,m}}$ was remeasured to determine their water-equivalent thickness. The determination of ranges $R_{50,\mathrm{w}}^{\mathrm{IC}}$ and $R_{50,\mathrm{w,m}}^{\mathrm{IC}}$ by the interpolation of the PDD followed the same approach as range determination method described in Chapter 2, section 2.2.2.4. $R_{50,\mathrm{w}}^{\mathrm{IC}}$ and $R_{50,\mathrm{w,m}}^{\mathrm{IC}}$ can be defined as the depth in water at which the ionisation reading is 50% of the maximum value. The $R_{50,\mathrm{I}}$ was converted to $R_{50,D}^{\mathrm{IC}}$ via the following equation [171].

$$R_{50,D}^{\mathrm{IC}} = 1.029 * R_{50,I}^{\mathrm{IC}} - 0.063 \qquad (\mathrm{A}.3)$$

where $R_{50,D}^{\mathrm{IC}}$ is the depth which the dose is 50 % of that at the maximum for the depth-dose curve in water and $R_{50,I}^{\mathrm{IC}}$ is the depth which the ionisation is 50 % of that at the maximum for the depth-ionisation curve in water. The $R_{50,D}^{\mathrm{IC}}$ measurements were performed to determine the water-equivalent thickness of the materials used with the phantom.

A.3. Results

A.3.1. EBT3 film irradiations for variable phantom configurations

Figure A.1 shows the average depth-dose profiles for the seven SW 1472 configurations. The uncertainty for each measurement was determined considering the propagation of the 0.5% relative standard uncertainty in positioning EBT3 film in

the phantom as well as the repeatability of measurement. All uncertainties are expressed as standard uncertainties ($k = 1$) and are presented in the error bars shown in Figure A.1. The average range standard uncertainty for all configurations was between 0.51-0.64%.

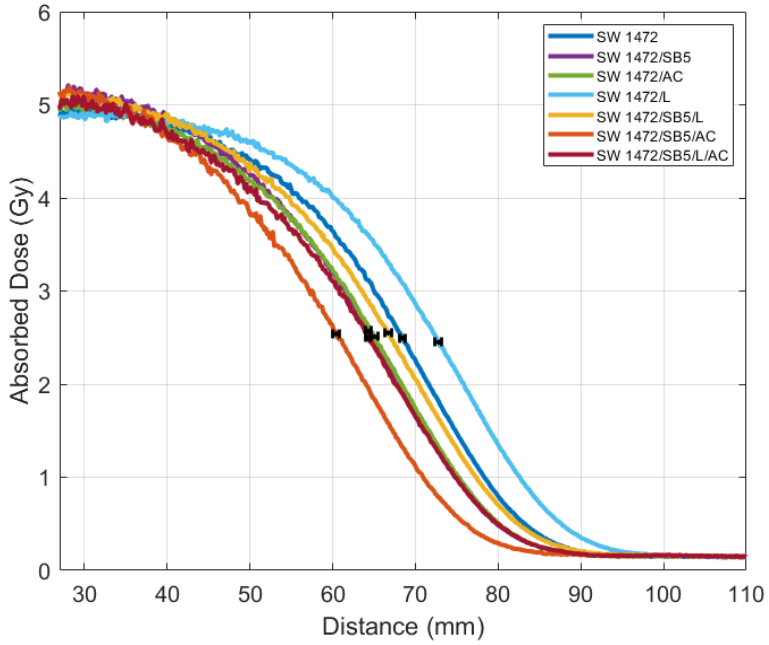

Figure A.1 *Average depth-dose profile for SW 1472 configurations in an electron beam*

Table A.2 shows the R_{50} values calculated from the depth-OD and depth-dose profiles for the 7 different RaLPh configurations. $\mathrm{R}_{50,\mathrm{D}}^{\mathrm{Film}}$ data points have been extracted from depth-dose profiles as illustrated in Figure A.1. The ratio between the range determined from the OD and dose profiles was determined. The results indicated that a constant range calibration factor value of 1.019 ± 0.001 could be applied to $R_{50,\mathrm{OD}}^{\mathrm{Film}}$ to obtain $R_{50,\mathrm{D}}^{\mathrm{Film}}$.

Table A.2 $R_{50,OD}^{Film}$ *and* $R_{50,D}^{Film}$ *for the seven SW 1472 setups for electron beam measurements*

Configuration (n)	$R_{50,\mathrm{OD}}^{\mathrm{Film}}$ (mm)	$R_{50,\mathrm{D}}^{\mathrm{Film}}$ (mm)	Ratio
SW 1472	80.88	68.66	1.18
SW 1472/SB5	77.07	64.37	1.20
SW 1472/AC	77.46	65.18	1.19
SW 1472/Lung	85.35	72.87	1.17
SW 1472/SB5/Lung	80.74	66.67	1.20
SW 1472/SB5/AC	73.07	60.19	1.21
SW 1472/SB5/Lung/AC	77.24	64.17	1.20

A.3.2. Ionisation chamber measurements

Table A.3 shows the calculated $R_{50,\mathrm{D}}^{\mathrm{IC}}$ for the ionisation chamber measurements as well as the experimental determined WET and $r\mathrm{WET}$.

Table A.3 $R_{50,D}^{IC}$ *water-equivalent thickness and relative water-equivalent thickness measurements derived from the ionisation chamber measurements*

Material	$R_{50,\mathrm{D}}^{\mathrm{IC}}$ (mm)	WET (mm)	$r\mathrm{WET}$
Water	66.64		
SW 1472	62.54	5.40	1.08
SB5	57.94	10.00	1.99
Accura Bluestone	57.94	9.18	1.84
Lung (LN 330)	65.49	1.18	0.23

A.4. Discussion

Preliminary electron beam experiment demonstrated that the RaLPh phantom had the possibility of being used to determine the range shift of different solid water, bone, and lung configurations with EBT3 film. The preliminary experiment allowed practice of experimental procedure and analysis of results before testing at a proton beam centre. Water-equivalent and relative water-equivalent values were different from those determined via proton experiments (Chapter 2, Table 2.6), particularly for

the bone substitute materials. The ionisation peak measurement (required for the determination of the range) may have been slightly less well characterised for the bone materials due to the peak being close to the start of ionisation measurements, resulting in a slightly less accurate determination of the $R_{50,I}^{\mathrm{IC}}$. Also WET measurements may be less reliable due to the greater scattering of electrons compared to that of proton beams, so there is more variability in the R_{50} range value. Results also showed a constant calibration factor of 1.019 ± 0.001 between OD and dose R_{50} values. Hence facilitating the streamlining of experimental measurements as the acquisition of the calibration curve would not be required.

B.Elemental composition of tissue and commercial tissue-equivalent materials

B.1. Cortical bone and cortical bone-equivalent materials

The material formulations were collected from published data and private communications [47,48,61,91,139]. Some formulations cannot be stated due to intellectual property restrictions.

Table B.1 *Elemental composition and density of cortical bone and bone-equivalent plastics*

Material	ICRP Cortical Bone	Accura Bluestone	CIRS Cortical Bone	CIRS Dense Bone (1250 mg/cc)	Delrin	Gammex Cortical Bone (SB3)	Hard Cortical Bone (SB5)	NPL Bone
Density	1.8500	1.7800	1.9100	1.8200	1.4250	1.8250	1.8400	1.3200
H	0.0472	0.0311		0.0360	0.0670	0.0341	0.0260	0.0602
C	0.1443	0.2280		0.2880	0.4000	0.3141	0.3058	0.6326
N	0.0420			0.0110		0.0184	0.0098	0.0492
O	0.4461	0.4520		0.3200	0.5330	0.3650	0.3893	0.0911
F		0.0216						
Na		0.0004						
Mg	0.0022							
Al		0.0049						
Si		0.2530						
P	0.1050			0.1080				
S	0.0032	0.0004		0.0008				
Cl		0.0036		0.0004		0.0004	0.0006	
K		0.0001						
Ca	0.2099	0.0009		0.2330		0.2681	0.2685	0.0761
Ti		0.0001						0.0909
Fe		0.0002						
Ni		0.0004						
Zn	0.0001	0.0001						
Sb		0.0023						
Ba				0.0032				
Total	1.000	0.997	1.000	0.997	1.000	1.000	1.000	1.000

B.2.Vertebra bone and vertebra bone-equivalent materials

Table B.2 *Elemental composition and density of vertebra bone and bone-equivalent plastics*

Material	ICRP Vertebra Bone (excluding C4)	CIRS Bone 800 mg/cc HA	Gammex Bone #480	Gammex Bone #484	Leeds Test Object (Average Bone)
Density	1.4200	1.5300	1.3350	1.5600	1.4000
H	0.0629	0.0570	0.0668	0.0477	0.0571
C	0.2607	0.4080	0.5348	0.4163	0.5058
N	0.0390	0.0100	0.0212	0.0152	0.0167
O	0.4356	0.2590	0.2561	0.3200	0.2820
Na	0.0010				
Mg	0.0010				
P	0.0609	0.0830			
S	0.0030	0.0007			
Cl	0.0010	0.0003	0.0011	0.0008	0.0010
K	0.0010				
Ca	0.1329	0.1790	0.1201	0.2002	0.1374
Fe	0.0010				
Ba		0.0028			
Total	1.000	0.997	1.000	1.000	1.000

B.3. Muscle and muscle-equivalent materials

Table B.3 *Elemental composition and density of muscle and muscle-equivalent plastics*

Material	Muscle	CIRS Muscle	Gammex Muscle
Density	1.0500	1.0620	1.0500
H	0.1020	0.0910	0.0810
C	0.1430	0.6970	0.6717
N	0.0340	0.0210	0.0242
O	0.7100	0.1680	0.1985
Na	0.0010		
P	0.0020		
S	0.0030		
Cl	0.0010	0.0010	0.0014
K	0.0040		
Ca		0.0220	0.0232
Total	1.000	1.000	1.000

C. Bone-equivalent materials study

C.1. Introduction

Ideally, a tissue-equivalent material should be validated against the human tissue that it is designed to mimic the energy range required for the modality. However, due to limited accessibility of human tissues, animal tissues provide a good alternative for experimental testing. A preliminary study was carried out to test bone-equivalent materials against real pig bone samples for a range of imaging photon beam and clinical proton beam and material properties; density, HU, RSP, partial fluence correction and relative scattering properties. At that time, a new proton optimised bone-equivalent material had not been manufactured, and so only commercial bone-equivalent materials were tested against real bone.

C.2. Methods

C.2.1. Real bone material samples

Pig cortical bone was used as human bone substitute [172,173] due to its elemental properties being similar to human bone and ease of availability from local butchers (Hepburn, Essex, UK, L. Buckle, Essex, UK and Teddington Butcher Ltd, Middlesex UK). The pigs aged from approximately 6 months to 1 year before butchering. The bones were cleaned of any biological tissue via manual cleaning with knives and scissors (Figure C.1 a)), light boiling, and cleaning in acetone. The bones were sawn and only the dense bone within the main leg shaft processed into a powder at Verder Scientific UK Ltd (Hope Valley, UK). The grinding of the pig bone into a powder was completed in two stages: i) the bone pieces were passed through the cutting mill SM 300 with a six-disc rotor at a speed of 1000 RPM three times reducing

the sieve hole diameter from 10 mm, 4mm and 1 mm each time, ii) The finer power was then placed in a ZM200 ultra-Centrifugal mill with 12 teeth rotor and a ring sieve with 0.5 mm aperture. The mill was operated at 12,00 RPM. This turned the bone into the consistency of flour (Figure C.1 b)) for compacting into 3D printed containers.

a)  b) 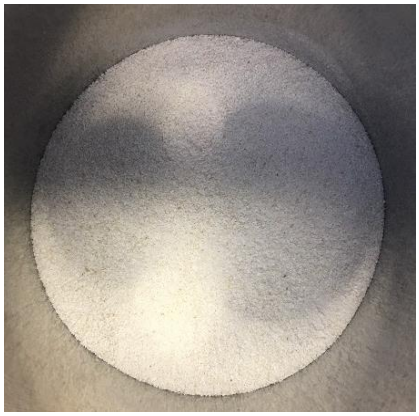

Figure C.1 *Bone to powder form*

The bone material was tested with mass spectrometry at NPL to provide an understanding of the elemental composition of the sample. This work was to assess the impact of using mechanical grinding compared to manual crushing on the bone samples, due to concerns of the mechanical grinding causing an increase in higher Z elements in the sample (Figure C.2). The number and amount of each element between the crushed and ground samples were similar apart from Iron (Fe) and Bromine (Br). Iron was more prominent in the crushed sample possibly due to older cutting equipment being used for these bones' samples. Interestingly, Bromine was found in a larger amount in the ground sample which might suggest contamination in the grinding process at the centre. It was concluded that the grinding process did not significantly increase the presence of higher Z element to the samples and was considered suitable for experimental measurements.

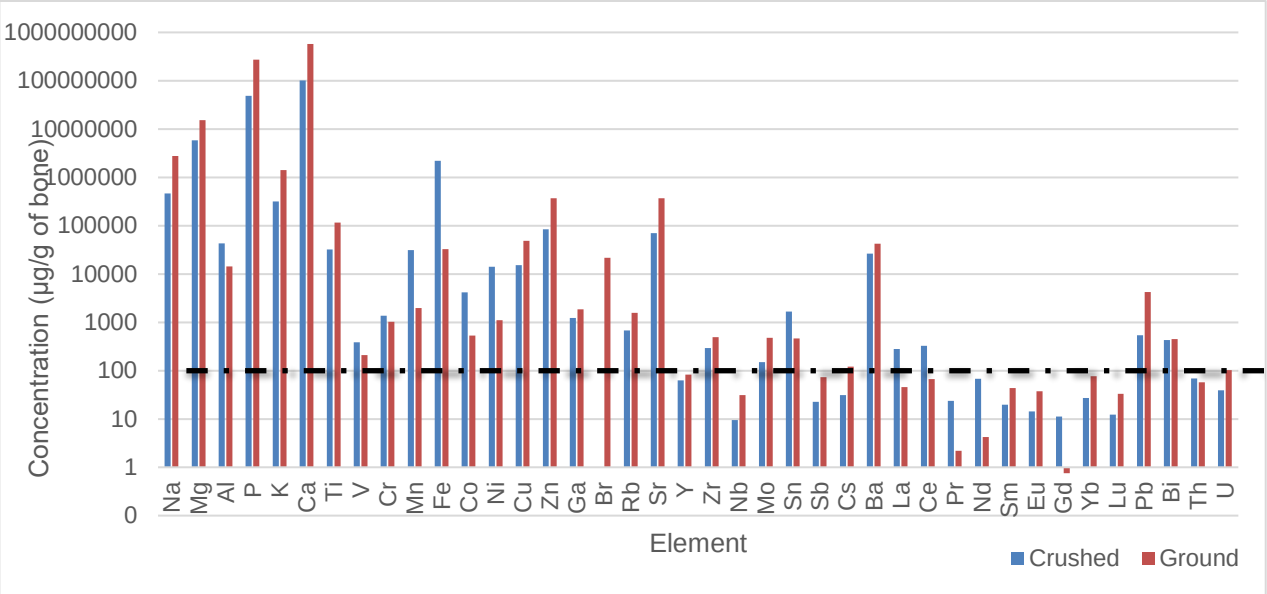

Figure C.2 *Mass spectrometry of bone samples. Crushed refers to manual grinding of the sample whilst ground to automated grinding. The black dashed line highlights the amount which is considered a trace element (100 µg/g) in a sample.*

3D printable containers for the bone powder were designed (Figure C.3 a) and b)) and printed with an Anet A8 printer. The containers were designed to have the same internal volume as the commercial material samples. The holders were printed in PLA and all containers and PLA discs were printed from the same reel of filament to reduce filament variability. PLA discs were printed so the PLA face thickness (0.81 ± 0.06 mm) of the containers could be replicated with the other samples for the experimental measurements (Figure C.3 c)). The bone powder was tapered and compacted into the containers (Figure C.3 b), and CT scans with the Mediso AnyScan SCP at NPL performed to ensure that the holder was filled and did not include airgaps via visual inspection of the scans before measurements at the proton centre.

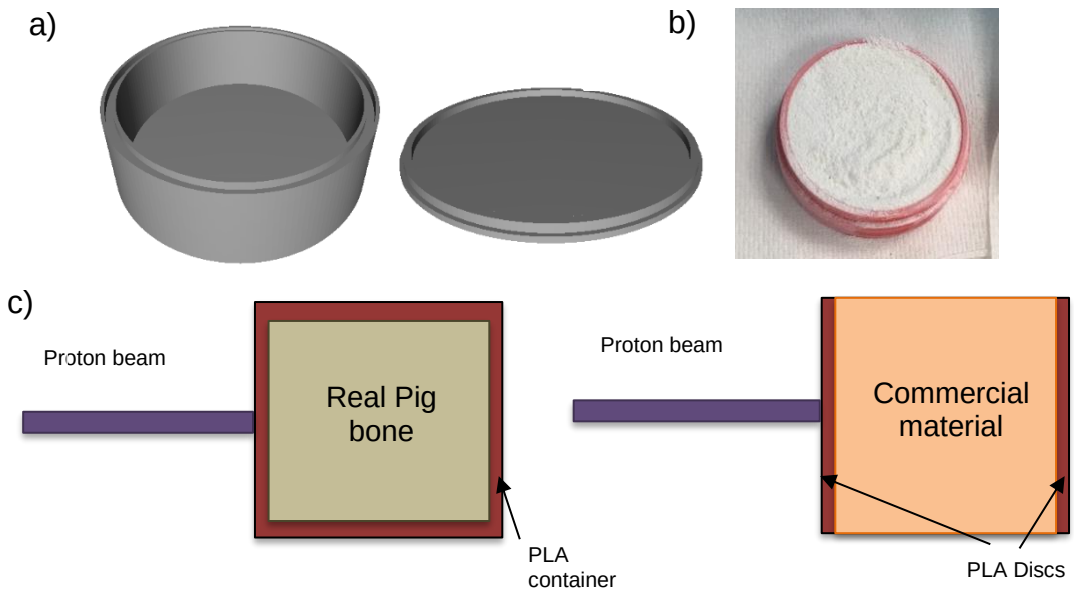

Figure C.3 *a) 3D design of holder and filed holder, b) 3D printed holder with pig bone powder. c) Comparison of setup for bone and commercial materials*

The following commercial materials were tested against pig bone: SB5 Hard bone, Delrin, and NPL bone [91,143]. Cylindrical samples (5 cm diameter and thickness of 0.5 cm, 1.0 cm (x2) and 1.5 cm) were manufactured to reduce the amount of bone material required per sample. The samples were tested at NPL and the Rutherford Cancer Centre North East. A range of measurements were carried out to characterise the pig bone samples as well as bone-equivalent substitutes.

C.2.2. Experimental measurements

C.2.2.1. Density

The measured material density of the samples was measured using the same method described in Chapter 2, section 2.2.1.

C.2.2.2. CT scans of samples

Each cylinder was scanned in a Mediso AnyScan SCP scanner and a Phillips Big Bore CT scanner at NPL and the Rutherford Cancer Centre North East, respectively. The samples were placed centrally within custom made inset within bolus sheets and solid water was placed above and below the setup on the carbon fibre CT couch. This custom made inset for the samples was developed to reduce scattering and artefacts in the scan due to air. The following scanner settings were used at the Rutherford Cancer Centre; helical scan, tube voltage of 120 kV, voxel size of 0.117 x 0.117 x 0.1 cm^3, average tube current of 286 mA, and scan reconstruction option of Brain. The following scanner settings were used at NPL; axial scan, 120 kV tube voltage, voxel size of 0.098 x 0.098 x 0.25 cm^3, tube current of 400 mA and scan reconstruction of abdomen.

C.2.2.3. Ionisation chamber measurements in a water phantom

A similar approach to the measurements described in Chapter 2 section 2.3.2.1 was applied to determine the WET of the different materials in consideration. A 150 MeV continuous pristine spot beam was delivered, and the PTW Bragg Peak chamber 34070 was moved a depth of 0.5 cm until the total range was determined and an external PTW beam monitor chamber 7862 was positioned in front of the beam right in front of the water phantom, and its signal used for normalisation. The chamber was then moved in finer steps of 0.02 cm over the Bragg peak and $R_{80,w}^{\mathrm{IC}}$ region. The PDI was corrected for temperature and pressure. The PDI measurements were assumed to be the same as the percentage depth dose (PDD) profile. For the pig bone samples, the PDI profiles of the sample thicknesses of 0.5 cm, 1.0 cm, 1.5 cm, 2 cm, 3 cm, 4 cm (excluding container thickness) were measured by using individual containers as

well as taping containers together. For the substitute materials, the PDI profiles of SB5 sample thicknesses of 0.5 cm, 1 cm, 2 cm, 3 cm, 4 cm were measured while for the Delrin and NPL bone thicknesses of 1 cm, 2 cm and 4 cm were measured.

The $R_{80,w}^{\mathrm{IC}}$ and $R_{80,w,m}^{\mathrm{IC}}$ values was determined via the same approach detailed in Chapter 2, section 2.3.2.1. Ionisation chamber measurements were performed to determine the WET and RSP of the tissue-equivalent materials.

The WET of the PLA container faces was determined analytically. The WET of the PLA container faces were calculated by the thin targets approach [3].

$$t_w = t_m \frac{\rho_m}{\rho_w} \frac{\overline{S_m}}{\overline{S_w}} \qquad (\mathrm{C}.1)$$

where t_w and t_m are the thickness of the water and the material, respectively, ρ_w and ρ_m are the mass densities of water and the material, respectively, and $\overline{S_w}$ and $\overline{S_m}$ are the mean proton stopping mass stopping power values for water and the material, respectively. The WET of the PLA containers was removed from the WET of each material setup.

C.2.2.4. Partial fluence correction factors

The partial fluence correction factors $k_{\mathrm{fl,partial}}^{\mathrm{Exp}}$ of each material were also calculated using PDI data. It should be noted that $k_{\mathrm{fl,partial}}^{\mathrm{Exp}}$ represents a partial fluence correction factor because it accounts for primary and some secondary particles and gives an indication of the equivalence between materials in terms of fluence.

As discussed in Lourenço et al. (2016) [136], the partial fluence correction factor can be determined from the ionisation chamber readings acquired for the WET measurements for the different samples , by the following equation:

$$k_{\mathrm{fl,partial}}^{\mathrm{Exp}} \approx \frac{M^{1}_{(\mathrm{z_w})}}{M^{2}_{(\mathrm{d,t_{m,w-eq}})}} \qquad (\mathrm{C.2})$$

where $M^{1}_{(\mathrm{z_w})}$ is the ionisation chamber reading in water, $M^{2}_{(\mathrm{d,t_{m,w-eq}})}$ is the ionisation chamber reading in water after passing through the bone substitute samples. The corresponding depth in water z_w is given by $z_w = d + t_{\mathrm{m,w-eq}}$, where d is an arbitrary depth in the M^2 setup and $t_{\mathrm{m,w-eq}}$ is the water-equivalent thickness of the material.

A mean value for $k_{\mathrm{fl,partial}}^{\mathrm{Exp}}$ can be calculated for N depths via the following equation.

$$k_{\mathrm{fl,partial}}^{\mathrm{Exp}}(\mathrm{t_{m,w-eq}}) \approx \frac{1}{N}\frac{M^{1}_{(\mathrm{z_w})}}{M^{2}_{(\mathrm{d,t_{m,w-eq}})}} \qquad (\mathrm{C.3})$$

The partial fluence correction factor was determined from the most proximal depth to a distal depth of 8.5 cm, to ensure only the plateau region was considered in the calculation as positioning in depth becomes very critical at the Bragg peak due to the steep gradient.

C.2.2.5. Relative scattering measurements

A proton will undergo multiple small Coulombic scattering interactions with the nuclei of the material as it travels through the material [10]. These small scattering interactions results in a change in the particles trajectory in the medium. Several multiple scattering theories, in particular Williams (1930), Moliere (1947, 1948) and Goudsmit and Sauderson (1940), have been proposed to describe multiple scattering interactions [12,174–177]. The statistical outcome is a multiple scattering angle of the proton beam and is in general approximated to a Gaussian distribution.

For this work, measurements were performed to investigate the proton beam lateral spot profiles of substitute materials against bone samples. The samples were placed in a sample holder whilst the holder was taped to solid water blocks in front of the water phantom (Figure C.4). The isocentre was set to the surface of the sample. The beam was set the following settings: a centrally positioned 150 MeV spot beam delivering 188 MU. The spot profiles of each material were measured at two thicknesses: 1.5 cm and 4 cm. Film was placed in front and behind the samples and fiducials were draw on the film to show the vertical and horizontal alignments. The films were handled by the same procedure described in Chapter 2 section 2.2.2.1.

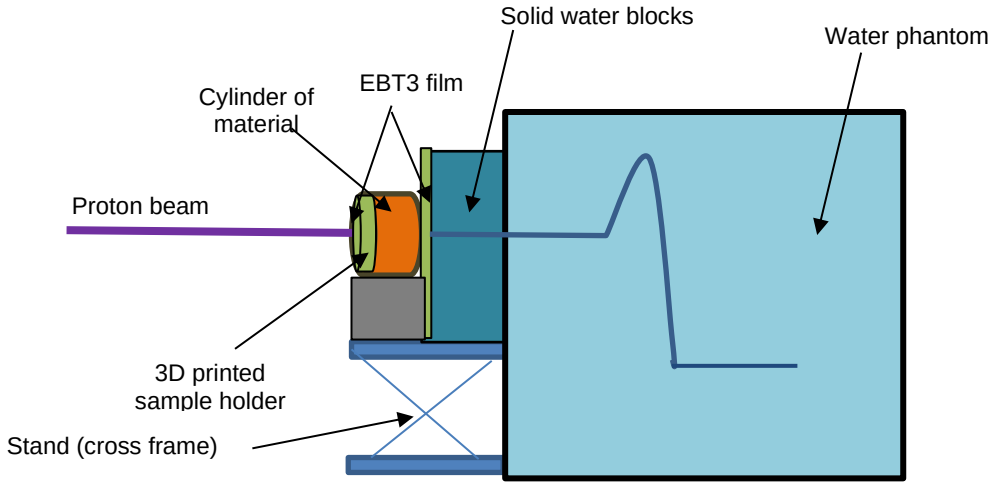

Figure C.4 *Scattering measurement setup*

EBT3 films were analysed with FilmQA Pro 2016 software (Ashland Inc. Wayne, NJ, USA). For all film analysis, the film was cropped and aligned using FilmQA Pro software settings. The horizontal and vertical line profile options were used between fiducials marks. No calibration curve was implemented into FilmQA Pro; the vertical and horizontal optical density profiles from the red channel were exported from Film QA Pro to MATLAB 2019a. The profile data was then fitted with a gaussian fit (3rd

order polynomial) via the curve fitting toolbox. The fitting data was used to calculate the full width half maximum (FWHM) (Figure C.5) [178].

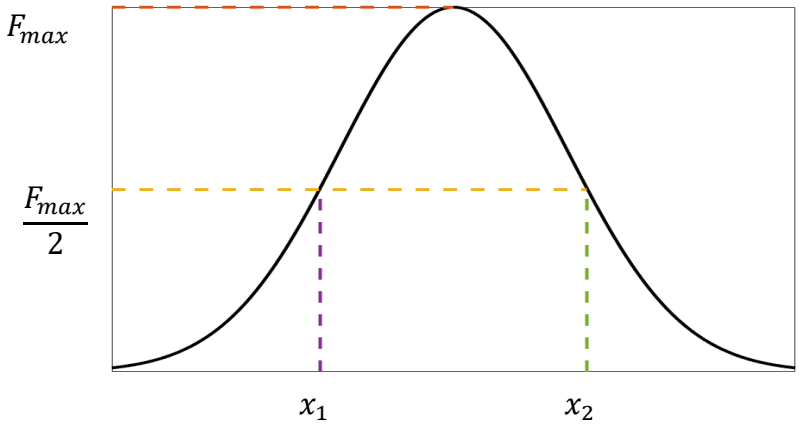

Figure C.5 *Gaussian distribution and FWHM*

$$\mathrm{FWHM} = \ x_2 - x_1 \tag{C.4}$$

where x_1 and x_2 are values when the gaussain falls to half of its maximum value

$$\Delta x^2_{scattering} \ = \mathrm{FWHM}^2_{\mathrm{AS}} - \ \mathrm{FWHM}^2_{\mathrm{BS}} \tag{C.5}$$

where FWHM_{AS} and FWHM_{BS} is full width half maximum after (AS) and before (BS) the sample, respectively.

C.3. Results

C.3.1. Density and RSP measurements

Table C.1 shows the experimentally determined density and RSP values for the pig bone and substitute bone-equivalent materials. The table also shows the relative difference between experimental mass density and values against that of pig bone as well as target tissue, human cortical bone. For cortical bone, RSP was calculated theoretically with the cost-function model.

Table C.1 *Mass density and RSP measurements of samples (pig bone and substitute bone-equivalent materials)*

Physical and Radiation properties	Cortical Bone (ICRP)	Pig Bone	SB5	NPL Bone	Delrin
Average mass density (g/cm^3) (SD)	1.85	1.13 (0.03)	1.87 (0.01)	1.32 (0.02)	1.43 (0.00)
Average relative % difference to pig bone	NA	NA	65.5	16.8	26.5
Average relative % difference to human cortical bone	NA	39.0	1.1	28.6	22.7
RSP (SD)	1.66	1.00 (0.03)	1.65 (0.02)	1.37 (0.002)	1.23 (0.006)
Average relative % difference to pig bone	NA	NA	65.7	24.5	37.9
Average relative % difference to cortical bone	NA	-40.2	-0.8	-25.5	-17.5

C.3.2. Hounsfield Units

Table C.2 shows the experimentally determined average HU for the pig bone and substitute bone-equivalent materials. The table also shows the relative difference between experimental HU values against pig bone as well as target tissue, human cortical bone. For cortical bone, HU was estimated by the semi-analytical approach described in Chapter 2, section 2.3.3.2. It should be noted this approach is a HU estimate for cortical bone as method is only truly applicable to the NPL CT scanner.

Table C.2 *Hounsfield unit values for samples (pig bone and commercial bone-equivalent materials).* $\Delta HU = HU_{plastic} - HU_{tissue}$

Centre	Radiation properties	ICRP Cortical bone	Pig Bone	SB5	NPL Bone	Delrin
Rutherford Cancer Centre North East	Average HU (SD)	1120	486 (28)	1283 (55)	313 (1)	666 (14)
	ΔHU to pig bone	N/A	N/A	797	-173	180
	ΔHU to cortical bone	N/A	-634	163	-72.1	-40.6
NPL	Average HU (SD)	1120	480 (21)	1220 (26)	364 (2)	634 (18)
	ΔHU to pig bone	N/A	N/A	740	-116	154
	ΔHU to cortical bone	N/A	-640	100	-756	-486

C.3.3. Partial Fluence Correction

Figure C.6 shows the partial fluence correction for pig bone and commercial bone-equivalent materials over a range of thicknesses.

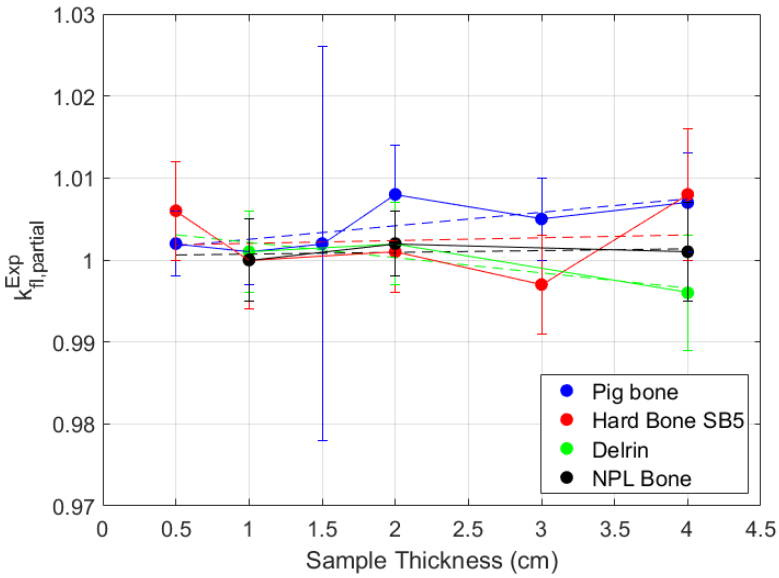

Figure C.6 *Partial fluence correction of pig bone and bone-equivalent materials at 150 MeV. Error bars shown standard deviation of each mean partial fluence at each thickness*

C.3.4. Scattering properties

Table C.3 shows the relative scattering properties for pig bone and commercial bone-equivalent materials for two sample thicknesses, 1.5 cm and 4.0 cm thickness, for both the vertical and horizontal proton beam profiles. The table also compares the relative scattering property of the commercial bone-equivalent materials to pig bone. A ratio value of unity would suggest the same scattering of pig bone and the commercial bone-equivalent material.

Table C.3 *Relative scattering properties for pig bone and commercial bone-equivalent materials (1.5 cm and 4.0 cm thickness samples.* $\Delta x^2_{scattering}$ *diff =* $\Delta x^2_{scattering,plastic} - \Delta x^2_{scattering,tissue}$

Radiation Property	Profile direction	Sample thickness (mm)	Pig Bone	Hard Bone SB5	NPL Bone	Delrin
$\Delta x^2_{scattering}$ (mm)	Vertical	15	10.21	10.61	15.91	9.53
$\Delta x^2_{scattering}$ diff (mm)	Vertical	15	N/A	0.40	5.70	-0.68
$\Delta x^2_{scattering}$ (mm)	Horizontal	15	8.40	6.01	12.52	7.21
$\Delta x^2_{scattering}$ diff (mm)	Horizontal	15	N/A	-2.39	4.12	-1.19
$\Delta x^2_{scattering}$ (mm)	Vertical	40	35.20	44.63	28.70	36.86
$\Delta x^2_{scattering}$ diff (mm)	Vertical	40	N/A	9.43	-6.50	1.66
$\Delta x^2_{scattering}$ (mm)	Horizontal	40	41.70	49.85	37.62	40.78
$\Delta x^2_{scattering}$ diff (mm)	Horizontal	40	N/A	8.15	-4.08	0.92

C.4. Discussion

This study successfully compared physical and radiation parameters of real bone sample against substitute bone-equivalent materials. However, the study was not able to replicate a real bone sample which mimicked the dense nature of human cortical bone. Table C.6 shows the pig bone material was around 40% lighter than human cortical bone. Therefore, due to the lower density of the pig bone samples, the study provided an insight into the bone-equivalence of substitute materials against spongiosa bone (1.18 gcm^{-3}) or cartilage (1.1 gcm^{-3}) [47,48] .

The study showed that NPL bone was the most bone-equivalent material compared to the pig bone material in terms of density, RSP and HU. However, when considering theoretical cortical bone results for density, RSP and HU, SB5 was shown to be superior. SB5 matched cortical bone for mass density and RSP on average within 1.0 %. HU measurements were within 100 HU to that of cortical bone which suggested SB5 could be correctly assigned mass density and RSP within 1.0% as dense bone during the stoichiometric calibration process.

Figure C.8 shows the partial fluence correction factor was small over the measured thicknesses and suggests the samples tested are equivalent in terms of nuclear interactions. Relative measurements of scattering (Table C.9) were also performed. The ratio between pig bone and bone-equivalent material appear to show no clear repeatable scattering comparison. The scattering property appears to differ depending on horizontal or vertical profiles. Repeat measurements with more thicknesses or a different approach may be required to improve relative scatter measurements.

Overall, the study provided an understanding of the challenges of developing real bone samples as well as helped to identify successful experimental methods for the characterisation of bone-equivalent materials against real bone samples.

D.Dosimetry measurements for phantom detectors

D.1. Introduction

Radiochromic film and alanine has been shown to quench in the Bragg peak region of a proton beam due their response being dependent on the type, fluence, and energy of the particles in the mixed radiation field [71]. This results in the detectors not providing an accurate absorbed dose measurement in the Bragg peak region.

Presently for proton therapy end-to-end audits film is typically used as a relative dose comparison to the TPS as well as to assess the homogeneity of the dose distribution [37,72]. As previously mentioned in Chapter 2, film dosimetry has been

well documented and film quenching is a key topic of discussion for proton therapy research [76,93,100,101,170]. Film quenching has been shown to result in up to a 20% under response of dose in the Bragg Peak region [93] as well as under response within spread out Bragg peak (SOBP) plans [76,170]. Previously work has focused on the investigation of film quenching around clinical doses levels [93,170]. However, in this phantom work, 5 x 2 Gy plans are delivered to the phantom to provide reduced uncertainty in alanine measurements. This study proposed testing a single energy beam and complex multifield cases at clinical dose of 2 Gy, as well as higher dose values (10 Gy) to investigate quenching effects in film.

Regarding alanine corrections, work by Palmans et al. (2018) and Carlino et al. (2018) have provided methods for the cross calibration and RE correction [37,71]. This work proposed to use the same approach of Palmans et al. (2018) and Carlino et al. (2018) for a Roos-and Semiflex-type chambers. The Roos-type chamber was proposed instead of a Farmer-type, because the Roos chamber is the recommended in the upcoming IPEM code of practice for proton dosimetry [167]. The PTW Semiflex Type 31010 chamber was chosen for phantom measurements due to its ability to operate in relatively small field sizes (field size range 3 – 40 cm^2) which are required for accurate dose measurements within the tumour region of the phantom.

Here, the determination of an alanine beam quality correction factor and the quenching of EBT3 and alanine within protons beams at dose levels and fields relevant for the head neck phantom measurements (Chapter 4) were investigated.

D.2. Methods

All proton measurements were taken at the Rutherford Cancer Centre Thames Valley. Measurements were performed over three visits to the centre.

D.2.1. Ionisation chamber measurements

D.2.1.1. Cross-calibration of Semiflex chamber

Beam output measurements were performed with a secondary standard PTW-Roos 34001 chamber in a 220 MeV single layer of 10 cm x 10 cm with 0.25 cm spot spacing and delivering around 2 Gy (10 MU per spot) at a depth of 2 cm in WT1 solid water. Isocentre was positioned at the solid water phantom surface. The PTW-Semiflex 31010 chamber used within the complex plan irradiation was then cross calibrated against the secondary standard Roos ionisation chamber at 2 cm depth within the 220 MeV reference field delivering the same dose (10 MU per spot). The Roos chamber and Semiflex chamber were operated at -400 V. Ion recombination and polarity correction factors were assessed for both ionisation chambers. Due to the uncertainties on the tabulated k_Q factors from IAEA TRS-398, this work looked to consider the calculation of dose by using either IAEA TRS-398 k_Q factors as well as the current best estimates for beam quality values published in Palmans et al. (2022) [166].

D.2.1.2. Ion recombination

Previous work has highlighted that ion recombination corrections can be significant in proton beams [179,180]. Ion recombination corrections vary depending on chamber type, beam energy, dose rate, and beam delivery (continuous or pulsed beams). Therefore, during this study ion recombination was calculated by different methods:

i. derived from a series of experiments by taking ionisation chamber readings at different polarizing voltages to obtain a Jaffé plot (extrapolation method)

ii. the best fit values derived from experiments by taking ionisation chamber readings at different polarizing voltages to obtain a Jaffé plot (extrapolation method)

iii. Two-Voltage Method (linear expression) for the ionisation chamber chambers, using the following equation [21]:

$$k_s = a_0 + a_1\left(\frac{M_1}{M_2}\right) + a_2\left(\frac{M_1}{M_2}\right)^2 \quad (\mathrm{D}.1)$$

where the a_i are constants for pulsed scanned radiation. M_1 and M_2 are the collected charges for the polarizing voltage ratio.

iv. for k_s< 1.03, Two-Voltage Method approximation (linear expression) for the ionisation chamber chambers [21]:

$$k_s - 1 = \frac{\frac{M_1}{M_2} - 1}{\frac{V_1}{V_2} - 1} \quad (\mathrm{D}.2)$$

Due to the possibility of charge multiplication effects at -400 V for the extrapolation method, the Jaffé plot were calculated considering with and without -400V measurements. Measurements were carried out using the cross-calibration conditions described in Appendices, section D.2.1.1.

D.2.1.3. Complex proton deliveries

The study included the delivery of a scanning target volume at 15 cm depth (STV-15) and a four-field proton plan to investigate quenching within the Bragg peak region. Firstly, the STV-15 plan delivered a homogenous box field irradiation (10 cm^3) centred at 15 cm deep in water. The Roos and Semiflex chambers were positioned at 15 cm (in the middle of the SOBP of the STV-15 field) and were irradiated separately. The effective point of measurement of the ionisation chambers was positioned at isocentre. The MUs of the plan were scaled to deliver approximately 10 Gy (8694.18 MU) for comparison with alanine measurements (section D.2.2.2.). For the ease of

setup, WT1 solid water was used for these measurements. Secondly, a four-field proton cylindrical (diameter = 5 cm, height = 5 cm) plan was designed to give similar measurement conditions to head and neck primary planning target volume (PTV) region. The plan (Figure D.1) was designed in Raystation 11B (version v12.0.100.0) by an experienced clinical medical physicist. Gantry angles at 0, 45, 85, 120 degrees were used. The plan was optimised to deliver 10 Gy and was calculated using the clinical Monte Carlo version 5.3 treatment planning code with an uncertainty of 0.5% and a dose grid resolution of 0.2 cm^3. The Semiflex chamber was positioned at 5 cm water-equivalent depth in WT1 solid water, positioned the chambers effective point measurement at the isocentre. The four-field 10 Gy plan was delivered to the chamber and absorbed dose to water was determined using the IAEA TRS-398 formalisation and values from Palmans et al. (2022) [166]. The corrected ionisation chamber measurements were then compared to the corrected alanine measurements.

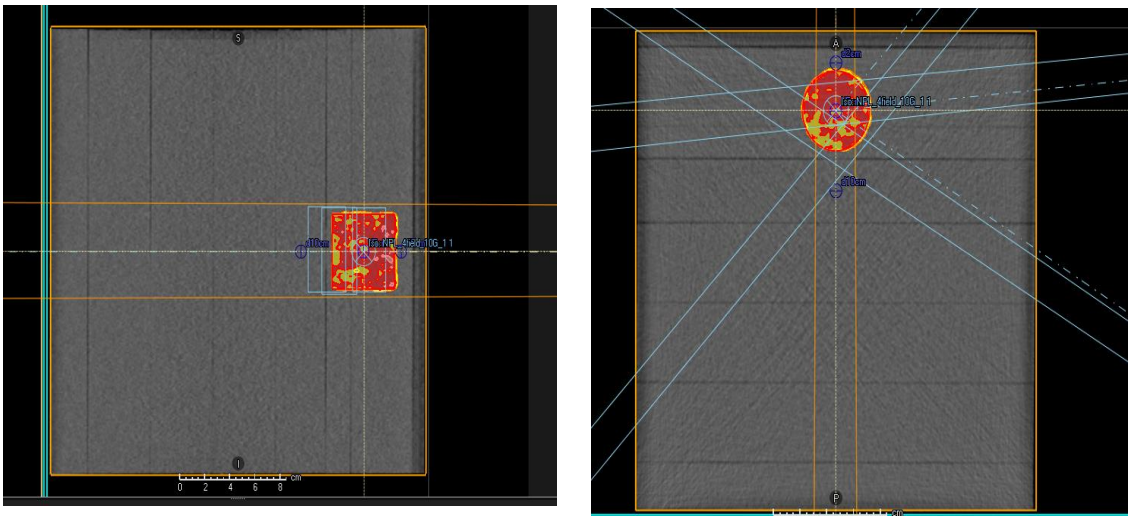

Figure D.1 *Four field plan a) Transverse plane b) Axial plane*

D.2.2. Alanine measurements

D.2.2.1. Cross-calibration method

The cross-calibration of alanine was performed in WT1 solid water slabs against the Roos chamber via the substitution method. Both detectors were alternately irradiated in a single-layer scanned field of size 10 cm × 10 cm, nominal energy 220 MeV delivering around 10 Gy (9391.05 MU), positioned at a reference depth of 2 cm water equivalent depth. Nine single pellets were irradiated over the 3 visits to the centre. The solid water phantom surface was positioned at isocentre. A high-energy of 220 MeV was chosen to provide a minimal energy spectrum spread of the beam. Due to constraints of the solid water-equivalent slabs available, there was a difference (estimated to be < 0.5 mm in water-equivalent thickness) between the ionisation chamber and alanine setups. A gradient correction factor within the plateau was determined and less than 1.000. Consequently, no gradient correction was applied as the difference was assumed negligible to the dose reading.

For ionisation chambers, dose to water can be calculated by equation:

$$D_{w,Q_{\mathrm{cross}}}^{IC} = M_{Q_{\mathrm{cross}}}^{\mathrm{IC}} N_{D,w,Q_0}^{\mathrm{IC}} k_{Q_{\mathrm{cross}},Q_0}^{\mathrm{IC}} \quad (\mathrm{D}.3)$$

where Q_{cross} is the beam quality at reference depth, $M_{Q_{\mathrm{cross}}}^{\mathrm{IC}}$ is the ionisation chamber reading corrected for pressure, temperature, polarity effects and ion recombination, $N_{\mathrm{D,w},Q_0}^{\mathrm{IC}}$ is the absorbed dose to water calibration coefficient of the ionisation chamber in the calibration beam quality Q_0, , and $k_{Q_{\mathrm{cross}},Q_0}^{\mathrm{IC}}$ is the beam quality correction factor for the ionisation chamber in the cross calibration beam quality. The absorbed dose to water was derived using the formalisation and beam quality correction factors either

from the IAEA TRS-398 code of practice [21] or from Palmans et al. (2022) [166]. A similar equation can be defined for alanine:

$$D_{\mathrm{w},Q_{\mathrm{cross}}}^{\mathrm{Alanine}} = M_{Q_{\mathrm{cross}}}^{\mathrm{Alanine}} N_{\mathrm{D,w},Q_0}^{\mathrm{Alanine}} k_{Q_{\mathrm{cross}},Q_0}^{\mathrm{Alanine}} \quad (\mathrm{D.4})$$

where the product $M_{Q_{\mathrm{cross}}}^{\mathrm{Alanine}} N_{\mathrm{D,w},Q_0}^{\mathrm{Alanine}}$ is the value that NPL provides as a ^{60}Co-reference value of absorbed dose to water. The notation of this quantity is $D_{\mathrm{w}}^{\mathrm{Co-ref}}$ in this work. $k_{Q_{\mathrm{cross}},Q_0}^{\mathrm{Alanine}}$ is the beam quality correction factor which can be derived from the cross-calibration method, using the condition that $D_{\mathrm{w},Q_{\mathrm{cross}}}^{\mathrm{IC}} = D_{\mathrm{w},Q_{\mathrm{cross}}}^{\mathrm{Alanine}}$ as follows:

$$k_{Q_{\mathrm{cross}},Q_0}^{\mathrm{Alanine}} = \frac{M_{Q_{\mathrm{cross}}}^{\mathrm{IC}} N_{\mathrm{D,w},Q_0}^{\mathrm{IC}} k_{Q_{\mathrm{cross}},Q_0}^{\mathrm{IC}}}{M_{Q_{\mathrm{cross}}}^{\mathrm{Alanine}} N_{\mathrm{D,w},Q_0}^{\mathrm{Alanine}}} \quad (\mathrm{D.5})$$

D.2.2.2. Complex proton deliveries

Alanine measurements were taken with both the STV-15 and 4-field plans for 10 Gy irradiations. For the STV-15 irradiations, 2 Farmer-type holders with 9 pellets and a single pellet were irradiated over the 3 visits. For the 4-field plan, 1 Famer-type with 9 pellets and a single pellet over the 3 visits. For the 4-field plan, the central 5 pellets from the Farmer-type holder were analysed to ensure they were in the homogenous region of the plan.

For alanine in a beam quality different to the cross-calibration beam, an additional correction should be applied, $k_{Q,Q_{\mathrm{cross}}}^{\mathrm{Alanine}}$, to account for the RE between the different fields:

$$D_{\mathrm{w},Q_{\mathrm{Plan}}}^{\mathrm{Alanine}} = M_{Q}^{\mathrm{Alanine}} N_{\mathrm{D,w},Q_0}^{\mathrm{Alanine}} k_{Q_{\mathrm{cross}},Q_0}^{\mathrm{Alanine}} k_{Q_{\mathrm{Plan}},Q_{\mathrm{cross}}}^{\mathrm{Alanine}} \quad (\mathrm{D.6})$$

The RE was calculated by the same approach described in Carlino et al. (2018) and Palmans et al. (2018). The correction for the alanine pellet was determined using

Raystation (version 10B ion). The RE is then determined from the ratio of the RE at the cross-calibration and the RE of the plan.

$$k^{\text{Alanine}}_{Q_{\text{Plan}},Q_{\text{cross}}} = \frac{\bar{\eta}_{\text{alanine},\,Q_{\text{cross}}}}{\bar{\eta}_{\text{alanine},\;Q_{\text{Plan}}}} \qquad (\text{D.7})$$

where $\bar{\eta}_{\text{alanine},\,Q_{\text{cross}}}$ is the RE of alanine in the cross-calibration field and $\bar{\eta}_{\text{alanine},Q_{\text{Plan}}}$ is the RE of alanine in the plan field. The RE and cross-calibration factor are then applied to ^{60}Co-reference value of absorbed dose to water to determine absorbed dose to water in the proton plan:

$$D^{\text{Alanine}}_{\text{w},Q_{\text{Plan}}} = \quad D^{\text{Co-ref}}_{\text{w}}\, k^{\text{Alanine}}_{Q_{\text{cross}},Q_0} \quad k^{\text{Alanine}}_{Q_{Plan}Q_{\text{cross}}} \qquad (\text{D.8})$$

D.2.3. Film measurements

D.2.3.1. Plateau region and complex proton deliveries

Film measurements were taken at the same measurement point and beam settings as described in sections D.2.2.1-2. to provide measurements in the plateau region as well as the Bragg peak region of the proton beam. An approximately 2 Gy and 10 Gy irradiations were delivered to the film and ionisation chamber via the substitution method. The films were handled and post processed using the methodology described in Chapter 2, section 2.2.2.1. Film analysis was performed with Vigo (version 2.0) using the green channel. A 12-point calibration curve (3rd order polynomial fit) was applied to films from a batch sheet irradiated with photon doses at NPL on Elekta Synergy Linac. For the comparison of film dose to ionisation chamber measurements, the average dose of the film was derived over an area comparable to the sensitive area of the Roos chamber area from the central region of the film.

For the 4-field plan, the film irradiation were also compared to the TPS dose distribution. Due to the film quenching, the film dose was scaled by the relative difference between the average dose of the film within the CTV region (90-100% dose threshold cut from film dose map) by either the average corrected alanine pellet dose or TPS dose value within the CTV region. Gamma index analysis (global and local) was performed to compare the dose distribution between the film and the predicted TPS dose distribution.

D.2.4. Summary of measurements

Table D.1 shows the summary table for measurements taken over the 3 visits to the centres.

Table D.1 *Summary of measurements taken during the 3 visits*

Detector	Measurement	Visit 1	Visit 2	Visit 3
Ionisation chamber	220 MeV, 10 x 10 $cm^{3,}$ Single layer, approx. 2 Gy	X		X
Alanine pellets		X		X
Film sheet				X
Ionisation chamber	220 MeV, 10 x 10 $cm^{3,}$ Single layer, approx. 10 Gy	X	X	X
Alanine pellets		X	X	X
Film piece				X
Ionisation chamber	STV-15, approx. 2 Gy			X
Alanine pellets				X
Film sheet				X
Ionisation chamber	STV-15, approx. 10 Gy			X
Alanine pellets		X	X	X
Film sheet				X
Ionisation chamber	4-field plan, approx. 2 Gy			
Alanine pellets				X
Film piece				X
Ionisation chamber	4-field plan, approx. 10 Gy			X
Alanine pellets				X
Film piece				X

D.3. Results

D.3.1. Ionisation chamber measurements

D.3.1.2. Ion recombination

Figure D.2 shows a linear relation between the inverse of the applied polarising voltage and the inverse of the ionisation chamber readings for a) Roos chamber and b) Semiflex chamber (Jaffé plots).

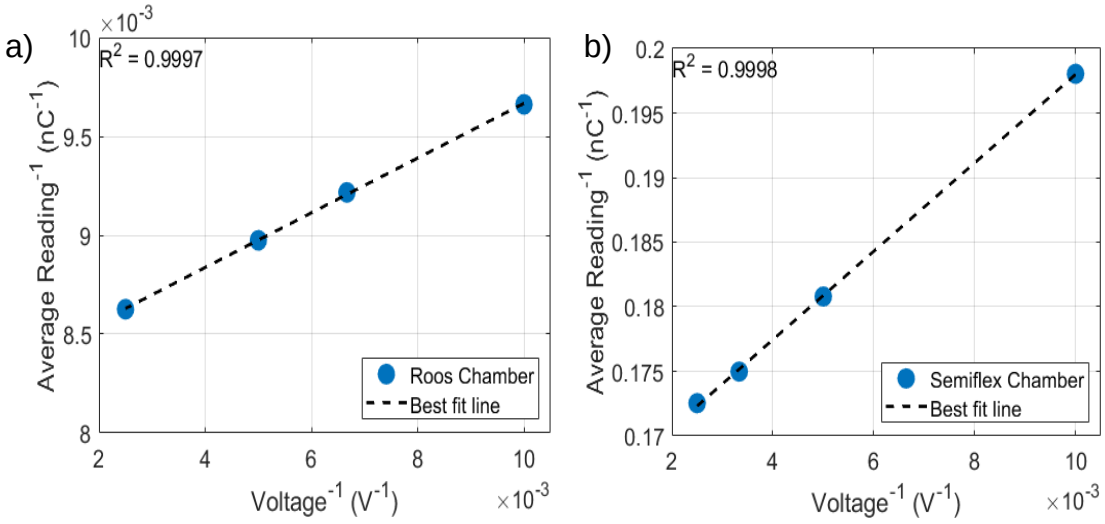

Figure D.2 *Inverse of the charge plotted against the inverse of the polarizing voltage for a) Roos ionisation chamber and b) Semiflex ionisation chamber. (Jaffé plots).*

Table D.2 shows the ion recombination corrections calculated for the Roos and Semiflex chamber.

Table D.2 *Ion recombination correction factors. The numbers in brackets represent ion recombination corrections calculated without the use of the - 400 V measurement, to reduce the effects of possible charge multiplication effects on the calculation*

Method	Ion recombination correction factor	
	Roos chamber	Semiflex chamber
Jaffé plots (measured value)	1.039 (1.039)	1.053 (1.055)
Jaffé plots (fitted value)	1.042 (1.042)	1.052 (1.053)
TRS-398 (Two-voltage method, equation D.1)	1.041	1.053
TRS-389 (Two-voltage method, equation D.2)	1.041	1.047

D.3.2. Alanine measurements

D.3.2.1. Cross calibration of alanine

Figure D.3 shows the $k^{\text{Alanine}}_{Q_{\text{cross}},Q_0}$ for all pellets irradiated during the three visits. When the IAEA TRS-398 $k^{\text{IC}}_{Q_{\text{cross}},Q_0}$ factors were applied, the mean $k^{\text{Alanine}}_{Q_{\text{cross}},Q_0}$ for the 9 pellets was 1.044 ± 0.01. While the mean $k^{\text{Alanine}}_{Q_{\text{cross}},Q_0}$ for the 9 pellets was 1.040 ± 0.01 when values published by Palmans *et al.* (2022) were applied.

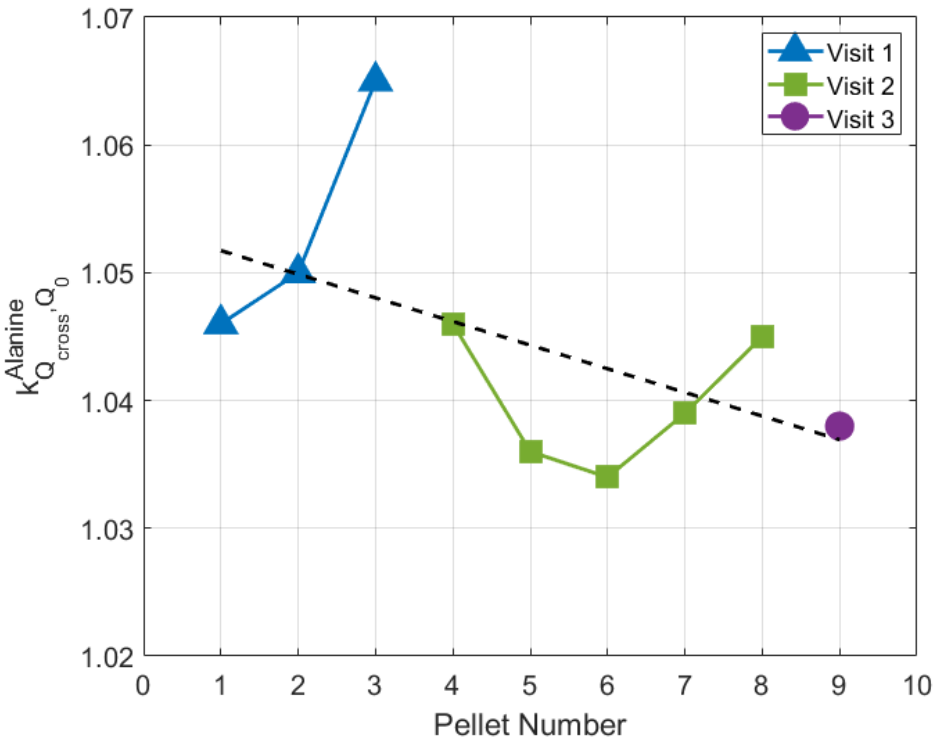

Figure D.3 *$k^{Alanine}_{Q_{cross},Q_0}$ for all pellets (using TRS-398 $k^{IC}_{Q_{cross},Q_0}$ factors). The dashed line show the linear fit thought all $k^{Alanine}_{Q_{cross},Q_0}$ values*

D.3.2.2. Complex proton deliveries

Figure D.4 shows the product of $M_Q^{Alanine} N_{D,w,Q_0}^{Alanine}$ for the STV-15 irradiations.

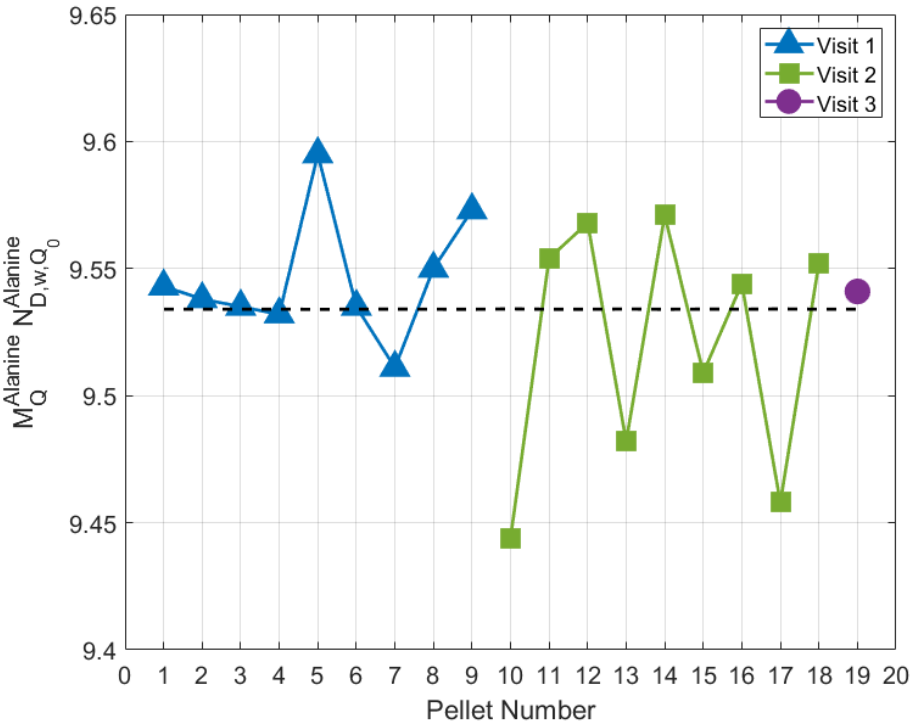

Figure D.4 *$M_Q^{Alanine} N_{D,w,Q_0}^{Alanine}$ for all pellets irradiated with 10 Gy in the STV-15*

Table D.3. presents the averaged pellets dose value per visit and the derived corrections factors ($k_{Q_{cross},Q}^{Alanine}$ and $k_{,Q,Q_{cross}}^{Alanine}$) to determine the absorbed dose to water in the proton beam ($D_{w,Q}^{Alanine}$) for the STV-15 irradiations. The alanine measurements were compared to Roos and Semiflex measurements in the STV-15 during visit 3.

Table D.3 *D_w^{Co-ref}, $k_{Q_{cross},Q_0}^{Alanine}$, $k_{Q_{Plan},Q_{cross}}^{Alanine}$, $D_{w,Q_{Plan}}^{Alanine}$ and difference to ionisation chamber measurements for STV-15 irradiations. *TRS-398 k_{Q_{cross},Q_0}^{IC} and **Palmans et al. (2022) k_{Q_{cross},Q_0}^{IC} values used for cross-calibration of alanine.*

Alanine pellets	D_w^{Co-ref} (Gy) (SD)	$k_{Q_{cross},Q_0}^{Alanine}$	$k_{Q_{Plan},Q_{cross}}^{Alanine}$	$D_{w,Q_{Plan}}^{Alanine}$	% difference to $D_{w,Q_{Plan}}^{IC}$	
					Roos	Semiflex
Visit 1	9.546 (0.03)	1.044*	1.000	9.966	0.1	0.8
		1.040**	1.000	9.928	<0.1	0.1
Visit 2	9.520 (0.05)	1.044*	1.000	9.939	0.4	1.02
		1.040**	1.000	9.901	0.3	0.3
Visit 3	9.541	1.044*	1.000	9.961	0.2	-0.8
		1.040**	1.000	9.923	0.1	-0.1
Average	9.533 (0.04)	1.044*	1.000	9.953	0.2	0.9
		1.040**	1.000	9.915	0.2	0.2

Similarly, to Table D.3, table D.4 presents the averaged pellet dose values as well as the corrections factors for the 4-field irradiation. The alanine measurements were compared to Semiflex measurements in the plan during visit 3.

Table D.4 *D_w^{Co-ref}, $k_{Q_{cross},Q_0}^{Alanine}$, $k_{Q_{Plan},Q_{cross}}^{Alanine}$, $D_{w,Q_{Plan}}^{Alanine}$ and difference to ionisation chamber measurements for 4-field irradiations. *TRS-398 k_{Q_{cross},Q_0}^{IC} and **Palmans et al. (2022) k_{Q_{cross},Q_0}^{IC} values used for cross-calibration of alanine. No ionisation chamber was irradiated in the 2 Gy plan, so the 10 Gy measurement was divided by a factor of 5.*

Alanine pellets	D_w^{Co-ref} (Gy) (SD)	$k_{Q_{cross},Q_0}^{Alanine}$	$k_{Q_{Plan},Q_{cross}}^{Alanine}$	$D_{w,Q_{Plan}}^{Alanine}$	% difference to $D_{w,Q_{Plan}}^{IC}$
Visit 3	1.914	1.044*	1.012	2.023	0.9
		1.040**	1.012	2.015	0.1
Visit 3	9.598 (0.06)	1.044*	1.012	10.143	0.6
		1.040**	1.012	10.104	0.2

D.3.3. Film measurements

D.3.3.1. Plateau region and complex proton deliveries

Table D.5 shows the average dose values from the film irradiation, as well as the difference to ionisation chamber measurements when considering the IAEA TRS-398 beam quality correction factors.

Table D.5 *Film irradiation dose values*

Film Irradiation	Film piece number	Irradiation description	Dose (Gy)	% difference to $D_{w,Q}^{IC}$
Visit 3	1	220 MeV, 10 x 10 $cm^{3,}$ Single layer, approx. 2 Gy	1.833	0.4
Visit 3	2	220 MeV, 10 x 10 $cm^{3,}$ Single layer, approx. 2 Gy	1.896	3.5
Visit 3	3	220 MeV, 10 x 10 $cm^{3,}$ Single layer, approx. 10 Gy	9.844	4.1
Visit 3	4	STV-15, approx. 2 Gy	9.417	0.6
Visit 3	5	STV-15, approx. 10 Gy	1.999	5.6
Visit 3	6	4-field plan, approx. 2 Gy	1.885	7.6
Visit 3	7	4-field plan, 10 Gy	9.264	9.2

D.3.3.2. Film compared to TPS predictions

Table D.6 shows the gamma analysis results for the 2 Gy and 10 Gy film irradiations compared to TPS dose distribution. For film at 2 Gy a mean value of 1.87 Gy was determined for the CTV region. Comparing alanine to film, a 7.7 % rescaling of dose was applied to the film map. While when comparing alanine to TPS, an 6.1 % rescaling of dose was applied to film map. For film at 10 Gy a mean value of 9.28 Gy was determined for the CTV region. Comparing alanine to film, an 8.5 % rescaling of dose was applied to the film map. While when comparing alanine to TPS, an 6.6 % rescaling of dose was applied to film map.

Table D.6 *Gamma pass rate for 4-field plans (2 Gy and 10 Gy deliveries). Global and local analysis with a dose normalisation of 2 or 10 Gy with dose threshold set to 20-100%.*

Dose level	Dose scaling method	Gamma pass rate (Global)					Gamma pass rate (Local)				
		3 % 2 mm	3 % 3 mm	4 % 3 mm	5 % 3 mm	5 % 2 mm	3 % 2 mm	3 % 3 mm	4 % 3 mm	5 % 3 mm	5 % 2 mm
2 Gy	Alanine	99.13	99.63	100.00	100.00	100.00	94.91	97.82	98.76	99.08	98.40
	TPS	97.53	98.30	99.45	99.91	99.77	95.69	97.20	98.72	99.50	89.90
10 Gy	Alanine	94.70	95.56	98.40	99.77	99.77	89.03	93.23	96.66	98.63	96.43
	TPS	94.10	95.25	98.86	99.95	99.95	91.13	94.29	97.99	99.82	98.99

Figure D.5 shows the film dose distributions, TPS predicted dose distributions and gamma index maps of the films for the 3 %/3 mm global criteria at 2 Gy and 10 Gy for the alanine and TPS scaled film and TPS comparison.

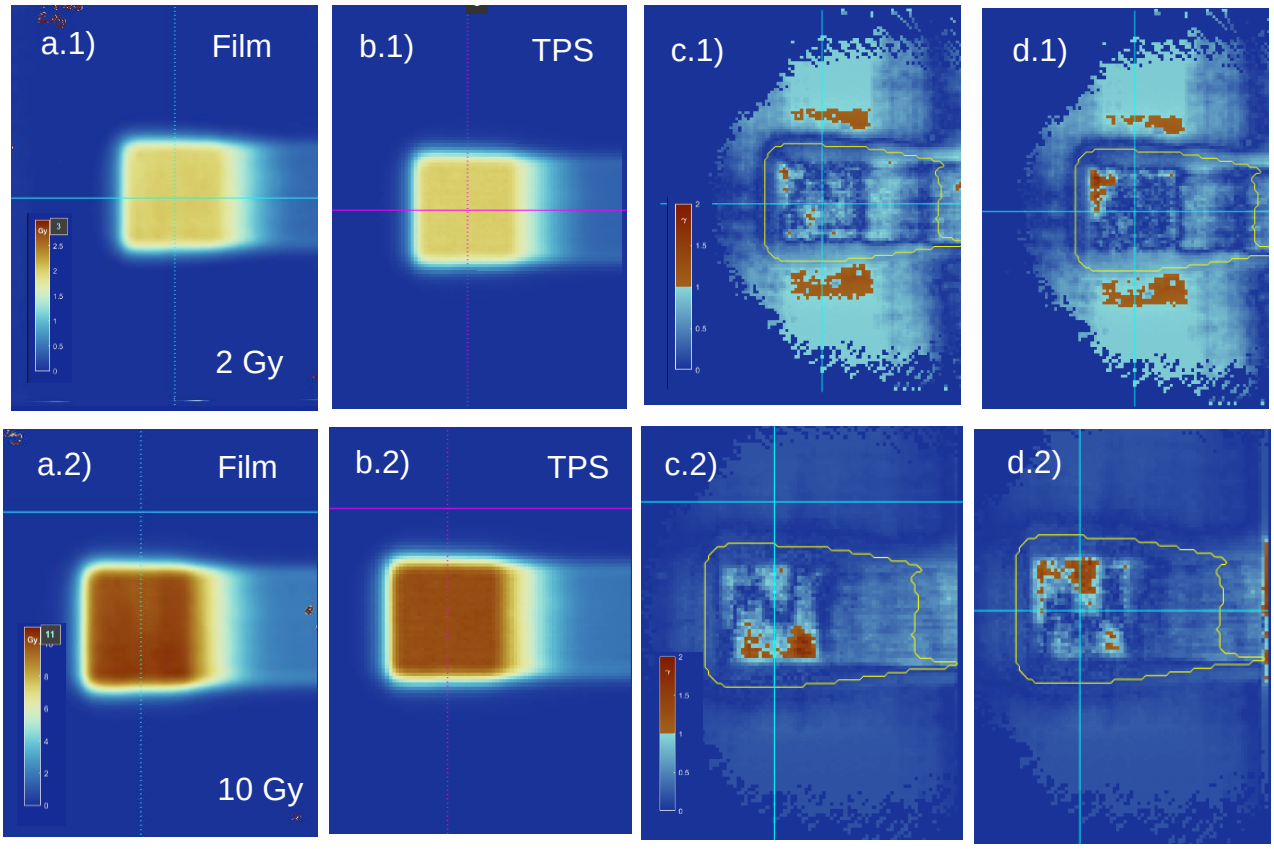

Figure D.5 *Film dose distributions at 2 and 10 Gy respectively (a.1 and a.2), TPS dose distribution for 2 and 10 Gy respectively (b.1 and b.2), Gamma analysis between alanine scaled film and TPS dose predictions for 3% /3 mm global criteria for 2 Gy nd 10 Gy respectively (c.1 and c.2), Gamma analysis between TPS scaled film and TPS dose predictions for 3% /3 mm global criteria for 2 Gy and 10 Gy respectively (d.1 and d.2).*

D.4. Discussion

Ion recombination results shows that for the Rutherford Cancer Centre Thames Valley, equipped with an IBA Proteus 230 MeV proton synchrocyclotron proton beam, ion recombination corrections can be as large as 4%-5% for plane-parallel plate or cylindrical ionisation chambers. Table D.2 shows there is good agreement between the different methods employed to determine ion recombination corrections, with possible charge multiplication effects at 400 V having minor impact of the final correction value. This work highlights the importance of characterising the ion recombination factor for ionisation chambers, in particular in pulsed scanning proton beams, as corrections can be significant.

The beam quality correction factor derived from the cross-calibration of alanine against the PTW Roos chamber, $k_{Q_{cross},Q_0}^{\mathrm{Alanine}}$, performed in a 220 MeV mono-energetic layer at 2 cm, was of the level of 1.04. The variation of pellets was found to (0.0096) be consistent with other studies into cross-calibration measurements (0.007) and suggested to be within the uncertainty of alanine relative measurement uncertainties (3% uncertainty for 68% confidence level). The beam quality correction factor is larger than values derived by Palmans et al. (2018) (1.022) derived at the MedAustron facility (Austria). The differences in calibration conditions can be also attributed to the differences, such as differences in proton energy, beam fluence, uncertainty in solid-water equivalence to water, detector difference and uncertainty in k_Q factors.

The beam quality correction factor derived from the cross-calibration and relative effectiveness correction factors were employed to derive dose from alanine measurements in complex beam deliveries: STV-15 (Table D.3) and 4-field plans (Table D.4). The good agreement within 0.2 % and 0.9% between the dose derived

from alanine and the dose derived from a Roos-type and Semiflex chambers provides confidence on the methodology adopted. On average the use of updated $k_{Q_{\mathrm{cross}},Q_0}^{\mathrm{IC}}$ by Palmans et al. (2022) was shown to provide better agreement between ionisation chamber and alanine than when using IAEA TRS-398 $k_{Q_{\mathrm{cross}},Q_0}^{\mathrm{IC}}$ values. Results showed for the 4-field plans, alanine and Semiflex chamber were shown to be on average within 0.6 % uncertainty, providing further confidence on the derived beam-quality and RE corrections.

The results from film measurements presented in Table D.5 were inconclusive. For measurements carried out at a 2 cm depth in the 220 MeV mono-energetic layer, where quenching is expected to be minimal, Films 2 and 3 showed a 4%-5% underestimate of dose for 2 Gy and 10 Gy dose deliveries. However, a repeat measurement at 2 Gy (Film 1) showed agreement within 0.5 % to ionisation chamber measurements. Ionisation chamber measurements carried out just below the film (film piece 1, 2, 3, 4 and 5) indicated irradiations agreement within 1.0 % to previous ionisation chamber measurements positioned at the same reference depth. Consequently, the reasoning for significant under-response is unclear, and may be due to possible issues with the film pieces, uncertainties on the batch calibration, as well as beam delivery uncertainties. Results in the Bragg peak region generally showed film quenching as STV-15 and 4-field film dose maps showed an under response of 6%-8% compared to alanine and ionisation chamber measurements. It should be noted that the 2 Gy STV-15 plan did show good agreement (within 0.6 %) between film and ionisation chamber measurements. Although previous work indicated film quenching to be less significant at high doses [170], this work shows quenching is still an issue and there is a need for a RE factor for absolute dose

measurements. Future work will investigate methods of applying RE corrections to film for complex proton deliveries.

For dose determination with film, a dose scaling factor via the use of alanine or TPS will be required for audit purposes. Table D.6 shows that when film is corrected for its under-response by using corrected alanine measurements, all gamma indexes pass rates considered were within good agreement to TPS predicted dose (95-100%) for global analysis. Results suggest the beam deliveries would pass an audit scenario, such as the IROC proton head and neck which considers 7%/4mm gamma analysis criteria with 85% of pixels pass rate [72].

This study has characterised the use of alanine and film quenching effects in proton irradiations to test the use of these detectors in an anthropomorphic phantom scenario. Overall, alanine results suggest that alanine can provide accurate dose measurements (within 0.6 %) when correction factors are applied. While for the determination of dose using film, a quenching correction factor is required. For phantom audit purposes, dose scaling of film by alanine would be required to enable relative dose distribution comparisons to TPS calculations.

E. Proton head and neck phantom in photon beams

E.1. Introduction

Preliminary experiments were performed with a megavoltage photon beam at NPL with an Elekta Synergy Linac to test photon-equivalence of the phantom as well as practice the experimental and analysis protocol with the phantom.

E.2. Methods

E.2.1. CT scanning of phantom

Laser alignment marks were drawn onto the phantom prior to scanning and were positioned on a reproducible alignment region near the CTV with a known isocentre distance from the coronal film location. Ball bearings were placed on the alignment markers to provide the isocentre position of the phantom. The phantom was scanned on the NPL Mediso AnyScan SCP scanner. A typical phantom scanning protocol was used to image the head and neck phantom, axial scan, 1.25 mm slice thickness, 300 mA tube current, 120 kVp and abdomen reconstruction to provide high resolution of the phantom. The phantom was scanned with dummy alanine and film within the phantom for treatment planning purposes.

E.2.2. Treatment planning of phantom

Using the CT image, a primary and secondary CTV contours and organs at risk regions (mandible, parotid glands, spinal cord, and brain stem) were registered onto the image for planning of the treatment. The contours were taken from an anonymous proton oropharyngeal patient’s plan and adapted to fit the phantom shape and detector position. A volumetric modulated arc therapy (VMAT) plan was devised with Raystation (version 11B). Typical clinical head and neck procedures were used when

developing the plan for the phantom. The plan was designed by an experienced clinical medical physicist. The plan was designed to deliver 65 Gy over 30 fractions. The plan resulted in the CTV receiving 61.77 Gy to 98% of the CTV volume. As well as the PTV receiving 58.45 Gy to 95% of the PTV region. The OARs were kept under acceptable dose constraints. The mean doses delivered to the left and right parotid glands were 32.72 Gy and 43.57 Gy, respectively. The spinal cord received a mean dose of 26.33 Gy and a dose of 66.14 Gy to 1% of the spinal region.

E.2.3. Dosimeter measurements

E.2.3.1. Beam output measurement

Beam output measurements with an ionisation chamber were performed in solid water at 5 cm depth. The reference point of a PTW-Semiflex 31010 chamber was positioned at the isocentre. A 6 MV, 10 cm x 10 cm with 100 MU was delivered to the ionisation chamber. Dose to water, $D_{w,Q}$, was derived from the ionisation chamber measurements following the recommendations of IPEM code of practice for high energy photons [181].

$$D_{w,Q} = \mathrm{M}_Q N_{D,w,Q}(QI) \qquad (E.1)$$

where M_Q is the chamber readings corrected for all influence quantities (temperature and pressure, ion recombination, polarity, and electrometer corrections) and $N_{D,w,Q}(QI)$ is the calibration coeffect for ionisation chamber for the specific beam quantity index.

E.2.3.2. Film reference calibration

All EBT3 films were handled following radiochromic film guidelines and best procedures [105,106]. Four film reference pieces were irradiated (3.5 cm x 4 cm) in

WT1 solid water with the film positioned at 5 cm depth with its reference point positioned at isocentre. A 6 MV beam of 10 cm x 10 cm was delivered, and the MU scaled to provide 2.5, 6.5, 10 and 12 Gy to each film piece. One piece was kept as background.

E.2.3.3. Phantom measurements

The laser markers were aligned to surface alignment markers on the phantom. The phantom was positioned on TPS planned isocentre. PTW Semiflex chamber measurements were performed during two separate 2 Gy plan irradiations to the CTV and OAR region to provide point dose measurements. An ionisation chamber measurement was also repeated in the CTV region for 2 Gy when the phantom had the weight shell added to the neck region on the phantom to assess the effect of patient variation on the VMAT plan.

The 2 Gy plan delivery was also delivered five times to the phantom with 3 alanine pellets positioned within the CTV and OAR regions (at the same reference point as the ionisation chamber) as well as film within the coronal plane to provide both point dose and distribution measurements. Point dose measurements were compared to TPS predicted values.

EBT3 films were scanned after 48 hours on an EPSON Expression 10000XL and film analysis was carried out with an in-house NPL software called Vigo (version 2.0.0) [168]. A previous determined 12-point batch film calibration was used, and the green channel applied for the phantom piece analysis. The green channel has been shown to be more sensitive than the red channel for doses over 6 Gy [108]. The film were scanned in the same method of as described in Chapter 2 section 2.2.2.1. The film was scanned via the standard procedure of horizontally (short edge of EBT3 film

perpendicular to scanning direction). However, due to film analysis suggesting possible scanner or film artefacts (Figure E.3), the film was rescanned vertically to investigate scanning orientation effects. The phantom piece dose map was scaled by the average % difference between the 10 and 12 Gy reference dose check values compared to the batch calibration predicted values. This was to ensure the film calibration was fitted for irradiated piece at the prescribed treatment dose. The film dose distribution was then compared to TPS predicted dose profile by global gamma index analysis.

E.3. Results

E.3.1. Beam output measurements

The beam output measurements were with 0.6% of nominal output measurements in the same setup and conditions. Phantom chamber measurements were corrected for the daily output difference.

E.3.2. *Phantom measurements*

E.3.2.1. Ionisation chamber measurements

Table E.1 shows ionisation chamber measurements in the CTV and OAR regions within the head and neck phantom as well as the comparison of those measurements to TPS predicted values.

Table E.1 Ionisation chamber measurements within phantom. *The TPS plan was not recalculated for the phantom neck shell.

Ionisation chamber location	Output corrected dose from Semiflex (Gy)	TPS predicted dose (Gy)	% Difference
CTV region	2.159	2.161	0.40
OAR region	1.249	1.255	0.48
CTV region (including weight gain shell)	2.133	2.161*	1.30

E.3.2.2. Alanine measurements

Table E.2 sows alanine measurements in the CTV and OAR regions within the head and neck phantom as well as the comparison of those measurements to TPS predicted values. Alanine results also showed agreement within 2 % with ionisation chamber measurements within the CTV and OAR, respectively.

Table E.2 *Average alanine measurements (3 pellets) within phantom*

Alanine pellet location	Output corrected dose from alanine (Gy) (SD)	TPS predicted dose (Gy) (SD)	% Difference
CTV region	10.879 (0.06)	10.810 (0.02)	0.64 (0.44)
OAR region	6.370 (0.19)	6.241 (0.16)	2.07 (0.27)

E.3.2.3. Film measurements

The film maps were corrected by reference dose check (average 2.26 % and 3.81 % difference at the 10 and 12 Gy) from the batch film calibration for the phantom film piece scanned in horizontal and vertical orientation, respectively. Table E.3 shows the gamma index results for the comparison between film and TPS dose distribution. Due to the horizontal orientation scan showing some possible film or scanner artefacts (seen as black box region on Figure 7.10), the film analysis was repeated in the vertical orientation.

Table E.3 *Film gamma analysis. Global and local analysis with a dose normalisation of 2 or 10 Gy with dose threshold set to 20-100%.*

	Global analysis					**Local analysis**				
Film scanning orientation	3%/2 mm	3%/3 mm	4%/3 mm	5%/3 mm	5%/2 mm	3%/2 mm	3%/3 mm	4%/3 mm	5%/3 mm	5%/2 mm
Horizontal	85.01	87.57	93.12	97.82	97.52	82.85	86.88	91.60	95.99	95.07
Vertical	94.57	96.08	99.54	100.0	99.94	90.28	94.61	98.34	99.56	98.62

Figure E.1 shows the gamma index of the film at 3%/3mm gamma index criteria (global) for the film scanned both horizontally and vertically.

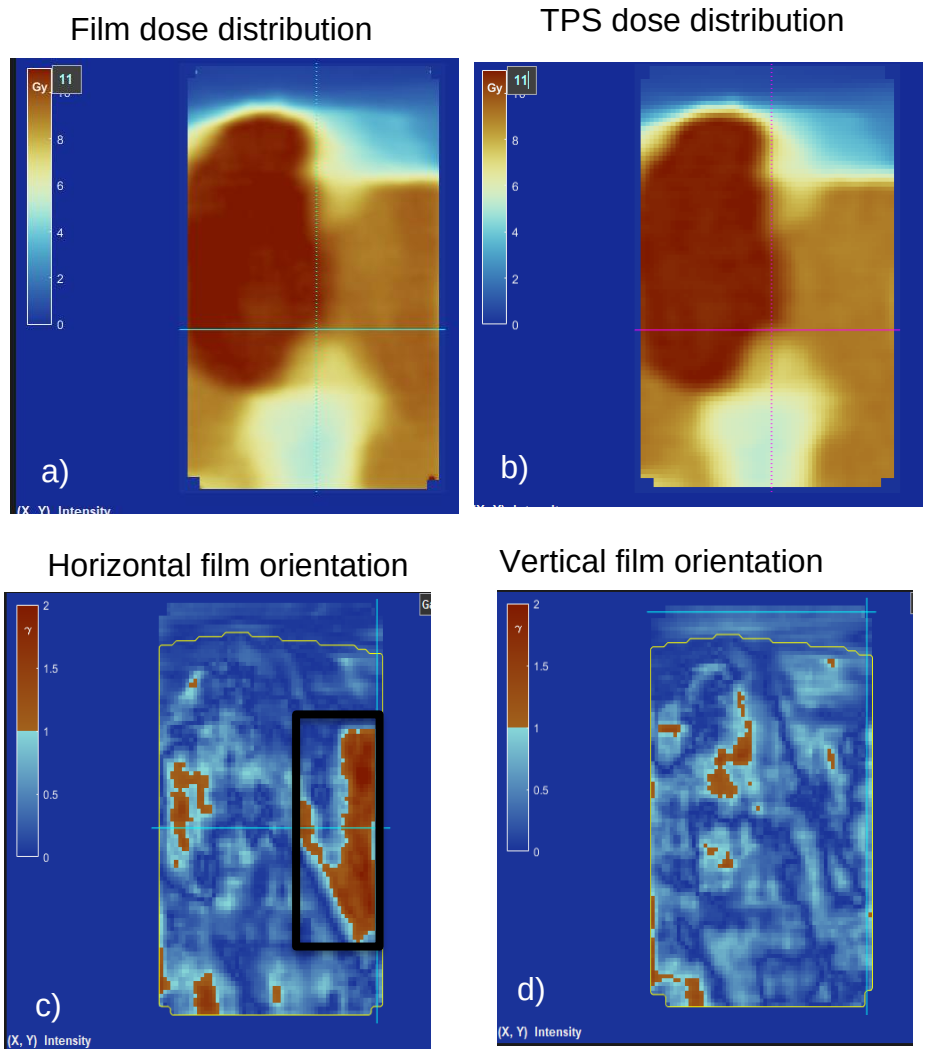

Figure E.1 *a) Film dose distribution, b) TPS dose distribution, Gamma map of film for 3%/3mm (global) c) horizontally d) vertically. Black box shows significant gamma index failure region, film showing an overresponse compared to the TPS.*

E.4. Discussion

The preliminary test showed the phantom allowed easy and repeatable setup. Table E.1 shows that the point dose measurements with the Semiflex chamber were within 0.5% to the TPS predicted doses for the CTV and OAR locations. The weight gain feature resulted in a 1.3% difference between chamber and TPS predicted doses.

The difference between CTV region ionisation chamber measurements with and without weight gain are within the uncertainty of ionisation chamber measurements, and so the impact of the weight gain cannot be determined from these measurements. Alanine measurements also show good agreement with TPS dose predictions (Table E.2), as alanine results were within 2% to TPS predicted values.

The film measurements were compared to the TPS predicted dose distribution. Results show that the film passed > 85% at 3%/3 mm and > 95% at 5%/2 mm criteria. These results would be considered a relatively poor pass rate compared to other NPL audits. Typically, a 95% for the 3%/3 mm criteria is considered a good standard of pass rate for VMAT delivery. The primary CTV shows good agreement to TPS; however, some variability can be seen in the secondary nodal CTV, where film measurement were higher than TPS predicted dose values (Figure E.3 c)). Due to the gamma index failure being situated mainly in a specific region along the film (seen in Figure E.3 c)), there was concern of possible scanner artefacts or film sheet failures. Therefore, the film was rescanned in the vertical orientation and gamma analysis repeated. The orientation of film showed a non-negligible impact on the results which showed the vertical orientation to provide better agreement with the TPS and passed a > 95% at 3 %/3 mm criteria. Scanner and film orientation is a known factor which can lead to film measurement uncertainty [182,183]. Butson et al. (2006) showed a change in scanned orientation can lead to a 4% variation for a 3 Gy irradiated EBT film. Due to the low gamma pass region not being replicated in the vertical orientation this may suggest any possible artefacts is extenuate by the combination of scanner light direction and film orientation. Due to the lack of conformity in the film analysis,

future work should look to repeat film measurements to ensure a 95% at 3%3 mm can be achieved in the standard orientation (horizontally).

Overall, results showed the photon equivalence of the phantom for audit purposes. The ionisation chamber and alanine measurements were within 0.5 and 2% with the TPS predicted values respectively. Film measurements was shown to provide a good method to compare the dose distribution measurands to TPS prediction (> 95% at 3 %/3 mm criteria). However, further work is required to characterise the differences found between film scanning orientation. This work has provided confidence in the protocol and analysis method for the use of the head and neck phantom as an end-to-end audit phantom.